Studying Charge Transfer Phenomena in the Interface of $SrCoO_3$ / $SrIrO_3$ Superlattices and Sr_2CoIrO_6 Double Perovskites Grown by Molecular Beam Epitaxy

by

Jibril Ahammad

A dissertation submitted to the Graduate Faculty of
Auburn University
in partial fulfillment of the
requirements for the Degree of
Doctor of Philosophy

Auburn, Alabama
August 9, 2025

Keywords: Molecular Beam Epitaxy, Band alignment, Interfacial charge transfer, Novel physics, Oxide heterostructures, X-ray Spectroscopy

Approved by

Dr. Ryan B. Comes, Chair, Associate Professor, Department of Materials Science and Engineering, University of Delaware
Dr. Minseo Park, Professor, Department of Physics, Auburn University
Dr. Jianjun Dong, Professor, Department of Physics, Auburn University
Dr. Yu Lin, Professor, Department of Physics, Auburn University
Dr. Byron H. Farnum, Associate Professor, Department of Chemistry and Biochemistry, Auburn University

Abstract

When two different transition-metal oxide thin films are stacked together, charge transfer can occur across the interface in certain cases. Interfacial charge transfer has been experimentally established as a promising mechanism to induce emergent electronic and magnetic phenomena. However, there is no established theoretical framework to predict or explain charge transfer in Transition metal oxides and experimental verification of existing theories is critical towards bridging this gap.

Motivated by the prediction of interfacial charge transfer in 3d-5d oxide heterostructures by *Phys. Rev. X 7, 011023 (2017)*, high quality epitaxial $(SrIrO_3)_n/SrCoO_3)_m$ (SIO/SCO) superlattices were grown using Molecular Beam Epitaxy (MBE). Scanning transmission electron microscopy and X-ray diffraction data confirmed excellent structural and crystalline quality of the films. X-ray absorption study (XAS) of Co L and O K edges confirms the perovskite nature of the SCO films. While $SrCoO_3$ underwent significant degradation when exposed to air for over 24 hours, it remained intact even after 6 months, when incorporated into a superlattice with $SrIrO_3$. This is likely because that Ir donates electron to Co and makes the structure stable.

Charge transfer was confirmed using synchrotron-based polarization-dependent hard X-ray absorption spectroscopy on Co K and Ir $L_{2,3}$ edges. The findings were complemented by In-vacuo X-ray photoelectron spectroscopy (XPS) and ex-situ Hard X-ray photoelectron spectroscopy (HAXPES) of Co 2p spectrum. An anisotropy between in-plane and out-of-plane charge transfers was observed indicating a corresponding anisotropy in the electronic structure. This suggests that the interface added another degree of symmetry-breaking, in consistent with previous studies. Polarization-dependent Ir L_2 edge data indicated a strain-induced orbital polarization in $SrIrO_3$ layers arising due to charge transfer or polar distortions due to interfacial effects. Angle-dependent pre-edge data on Co K edges indicated minimal Co 3d-4p mixing suggesting that $SrCoO_3$ layers in the superlattice remained just as distorted Octahedral coordination. A stronger hybridization effect was observed towards out-of-plane with the decreasing SIO : SCO layers ratio. Charge transfer was observed in Sr_2CoIrO_6 double perovskite films with a higher ratio of Co^{2+} than the superlattices.

These findings provide new insights into charge transfer mechanisms in metallic transition metal oxides, offering pathways to improve existing theoretical frameworks and explore novel interfacial physics.

Acknowledgements

I am deeply grateful to many people who supported me throughout my Ph.D. journey. First, I would like to express my sincere gratitude to my advisor Dr. Ryan Comes for his continuous support both in and out of the lab: from research, lab maintenance to visits to the national lab visits, data analysis, conference presentation, writing. He allowed me to work independently most of the time that helped me grow as an independent researcher. However, when needed, he provided valuable feedback efficiently that helped refine my ideas. I am grateful to my committee members- Dr. Minseo Park, Dr. Jianjun Dong, Dr. Yu Lin, and Dr. Byron Farnum- for their support in my doctoral study.

When I joined Auburn FINO lab, I was fortunate to be welcomed by four experienced graduate students, who helped me thoroughly in becoming independent to operate the MBE and XPS systems. Miles Blanchet provided me with comprehensive training on how the MBE system worked. He also trained me on operating Vibrating Sample Magnetometer (VSM) to measure magnetic properties of a thin film. Suresh Thapa and Rajendra Paudel taught me more intricate details on thin films growth and relevant analysis. Their mentorship in my initial film growths was incredibly helpful. Patrick Gemperline extensively trained me on the maintenance of the MBE and XPS system, particularly vacuum and cooling systems. All of them helped me in transferring samples from one location to another, which was challenging in the beginning. They were very patient and supportive. I am sincerely thankful to all of them.

I also appreciate the support of Brian Opatosky and Tanzila Tasnim, who joined the group after me. I had the pleasure of collaborating with Brian on cobalt and tantalum-based systems, and with Tanzila on iridates. Their contributions were invaluable to my research. I am especially thankful to Dr. Gaurab Rimal, a former postdoctoral researcher in the FINO Lab, from whom I gained deep insights into the MBE techniques and strategies for optimizing growth conditions. He also trained me in detail on electrical transport measurements.

I am thankful to Dr. Wencan Jin for his in-depth teaching on two-dimensional materials, and for training me on X-ray spectroscopy and electron diffraction. I thank Sunil Uprety for training me on Raman spectroscopy in Dr. Park's lab. I also thank Dr. Ayayi Ahyi for training me on

photolithography in the cleanroom of Auburn Physics and helping me on preliminary transport property measurements.

The research works of this dissertation would be impossible without the cooperation from the collaborators. I am thankful to Dr. Jerzy Sadowski (Brookhaven) and Dr, George Sterbinsky (Argonne) for acquiring XAS data of pure $SrCoO_3$ films. Dr. Bruce Ravel provided (Brookhaven) tremendous assistance by training and helping in acquiring Co K and Ir L edge data of the superlattice samples. Lidia Lapinski, Uditha Jayathilake and Dr. Alexander Gray (Temple University) measured the HAXPES data both at Temple University and in Diamond light source. I thank Dr. Gabriel Ortiz and Dr. Jinwoo Hwang (Ohio State) for performing scanning transmission electron microscopy in our superlattice films. Finally, I am thankful to Dr. Boris Kiefer (New Mexico State University) for his hard work on the theoretical study of our superlattice system.

This research work was supported financially by the U.S. Department of Energy, Office of Science under contract no. DE-SC0023478.The XRD instrument was supported through Major Research Instrumentation program from the National Science Foundation under contract no. DMR-2018794.

This research used resources from the Beamline for Materials Measurement (6-BM) and Beamline for Electron Spectro-Microscopy (21-ID) at the National Synchrotron Light Source II, a U.S. Department of Energy (DOE) Office of Science User Facility operated for the DOE Office of Science by Brookhaven National Laboratory under Contract No. DE-SC0012704. This research also used resources from the Beamline 9-BM-B,C in the Advanced Photon Source, an Office of Science User Facility operated for the U.S. Department of Energy (DOE) Office of Science by Argonne National Laboratory and was supported by the U.S. DOE under Contract No. DE-AC02-06CH11357.

The theoretical work used Stampede3 at Texas Advanced Computing Center through allocation DMR-110093 from the Advanced Cyberinfrastructure Coordination Ecosystem: Services & Support (ACCESS) program, which is supported by U.S. National Science Foundation grants 2138259, 2138286, 2138307, 2137603, and 2138296.

My sincere thanks go to the administrative staff in the physics department, especially Mary Prater and Glenda Stroud, whose help with bureaucratic processes saved me considerable time and effort. I am also thankful to Dave Patrick and the physics department for supporting me as a teaching assistant during the first three years of my Ph.D. I am grateful to my fellow cohort members- with whom I completed coursework for the degree. Together, we attended classes, exchanged ideas, and collaborated on solving challenging problems. I acknowledge that Microsoft Co-pilot was used in proofreading parts of the writing of this dissertation.

Beyond the lab and academic environment, I am grateful to the Bangladeshi student association at Auburn University. Their events and social gatherings provided much-needed mental support. Finally, I owe immense gratitude to my family and friends. Their unwavering support, encouragement, and love mean a lot to me.

Table of Contents

Abstract 2

Acknowledgements 4

List of Tables 11

List of Figures 12

List of Abbreviations 18

Chapter 1 : Backgrounds and Motivation 19

1.1 Introduction 19

1.2 Complex oxides 19

1.2.1 Perovskite oxide thin films and heterostructures 20

1.3 Interfacial charge transfer and its significance 22

1.4 Theory of charge transfer in complex oxides 24

1.5 About $SrCoO_3$ and $SrIrO_3$ thin film systems 25

1.6 Significance of 3d-5d interface study and $SrCoO_3$ / $SrIrO_3$ heterostructures 27

1.7 Physics corresponding to cobaltite and iridate systems 30

1.7.1 Crystal field theory 30

1.7.2 Pairing energy (vs crystal field) and spin-state 32

1.7.3 Spin-orbit coupling (SOC) 33

1.7.4 The Kondo effect 35

Chapter 2 : Thin Film Growth Method 38

2.1 Introduction 38

2.2 Thin films and epitaxial growth 38

2.3 Molecular Beam Epitaxy (MBE) 40

2.4 Auburn FINO Lab MBE system 41

2.4.1 Instruments 41

2.4.2 Growth steps: 44

2.5 Primary physical processes in an MBE growth 45

2.6 Instruments in the Auburn FINO Lab 46
Chapter 3 : Experimental Backgrounds 48
3.1 Introduction 48
3.2 Rutherford Backscattering Spectrometry (RBS) 48
3.2.1 Principle of RBS 49
3.2.2 Rutherford scattering cross-section 51
3.2.3 RBS experiments for our samples: 52
3.3 Reflection high-energy electron diffraction (RHEED) 53
3.3.1 RHEED instruments: 53
3.3.2 Principles of RHEED operation 54
3.3.3 RHEED Theory 55
3.4 X-ray diffraction (XRD) 61
3.4.1 How X-rays are generated 61
3.4.2 Principles of XRD 62
3.4.3 Instruments for XRD experiment 63
3.4.4 XRD measurement modes 65
3.4.5 Crystal structure determination and phase identification 68
3.4.6 X-ray diffraction from single crystal thin films and multilayers 68
3.4.7 Diffraction in real films 69
3.5 X-ray photoelectron spectroscopy (XPS) 70
3.5.1 XPS principles 70
3.5.2 Measurements and quantifications 71
3.5.3 Film thickness determination using XPS 73
3.5.4 Auburn FINO Lab XPS System 73
3.5.5 Hard X-ray photoelectron spectroscopy (HAXPES) 74
3.6 X-ray absorption near-edge structure (XANES) 75
3.6.1 X-ray absorption 75
3.6.2 XANES Theory 76
3.6.3 XANES Analysis 80
3.6.4 Experimental aspects 80

3.6.5 XANES detection modes 81
3.6.6 X-ray linear dichroism (XLD) 82
3.7 Electron Microscopy 83
Chapter 4 : Thin Film Growth and Characterizations 86
4.1 Introduction 86
4.2 Characterization backgrounds 86
4.3 $SrCoO_3$ (SCO) growth and characterizations 88
4.3.1 Backgrounds 88
4.3.2 Results and discussions 90
4.4 $SrIrO_3$ (SIO) growth and characterizations 94
4.5 $SrIrO_3$/$SrCoO_3$ (SIO/SCO) superlattice growth and characterizations: 96
4.5.1 Backgrounds 96
4.5.2 Results and discussions 97
4.6 Sr_2CoIrO_6 (SCIO) growth and characterizations 99
4.7 $LaCoO_3$ (LCO) growth and characterizations 100
4.8 Challenges and outlook 101
4.9 Conclusions 102
Chapter 5 : Charge Transfer Study using X-ray Absorption Near-Edge Structure (XANES) 103
5.1 Introduction 103
5.2 Computational modeling 103
5.3 Instrumental backgrounds and data acquisition: 107
5.4 Results and discussions 109
5.4.1 X-ray absorption near edge structure (XANES) and charge transfer 109
5.4.2 Ir $L_{2,3}$ X-ray linear dichroism (XLD) and anisotropy 112
5.4.3 Angle-dependence of Co K pre-edge and hybridization 113
5.4.4 Co K shoulder peaks and hybridization 117
5.4.5 In-plane vs out-of-plane pre-edge and octahedral distortion 119
5.5 Conclusions 120
Chapter 6 : Spin State Transition and Electrical Transport Properties 121
6.1 Electrical transport properties 121

6.1.1 Transport properties of $SrCoO_3$ 122
6.1.2 Kondo effect and electronic reconstruction in superlattice 123
6.2 Branching ratio and spin state 124
Chapter 7 : Outlook and Conclusions 126
7.1 Superlattice- set 1 126
7.2 Superlattice- set 2 128
7.3 Superlattice- set 3 128
7.4 $SrCoO_x$ 129
7.5 Outlooks on tantalum-based systems 129
7.6 Conclusions and prospects 130
References: 133

List of Tables

Table 1.1: Different charge transfer mechanisms in oxide heterostructures. (Adapted from [16]) 23
Table 1.2: A comparison of relative strengths among different competing interactions in 3d, 4d, and 5d systems. (Adapted from [34]) 28
Table 2.1: Materials properties of different systems grown by MBE vs other methods. (Adapted from [73]) 41
Table 5.1: R2SCAN crystallographic parameters of SCO and SIO 104
Table 5.2: Layer resolved orbital occupancy 20-atom heterostructures; 5x5x4; IS=-5. 106
Table 5.3: Layer resolved orbital occupancy, 40-atom heterostructures; 5x5x4; IS=-5 107
Table 5.4: List of all sampled studied with XAS 109
Table 5.5: Pre-edge fitting results from Figure 5.8 and Figure 5.9 115
Table 5.6: Shoulder peak positions in Figure 5.11 (SCIO- unannealed data was not in the figure, but included in the table) 118

List of Figures

Figure 1.1: Interactions between different degrees of freedom lead to rich physics in complex oxides. (Adapted from [6]) 19
Figure 1.2: An ideal Perovskite structure and the corresponding structure parameters. (Adapted from [9])..... 20
Figure 1.3: Chemical elements that can occupy sites in the perovskite structure. (Adapted from [8])..... 21
Figure 1.4: Oxygen continuity in the interface. (Adapted from [20]) 24
Figure 1.5: (a) Alignment of oxygen states at the interface, (b)The final equilibrium state. ε_p and ε_d are the local energy levels of oxygen p and TM- d states, (c) DFT reference data for $SrBO_3$. (Adapted from [17])..... 24
Figure 1.6: A schematic of an SIO/SCO superlattice..... 25
Figure 1.7: $SrCoO_x$ film in perovskite (left), and brownmillerite (right) phase. (Adapted from [30])..... 26
Figure 1.8: Crystal structure of orthorhombic perovskite $SrIrO_3$. Sr, Ir, and O atoms are shown in aqua, blue, and red. (Adapted from [24])..... 26
Figure 1.9: Structure of (a) $SrCoO_3$, (b) $SrIrO_3$, and (c) double perovskite Sr_2CoIrO_6. Sr, Co, Ir, and O ions are shown in green, yellow, blue, and red, respectively. (Adapted from [21])..... 29
Figure 1.10: splitting of the degenerate d-orbitals. (Orbital shape has been adapted from [57) .. 30
Figure 1.11: d-Level splitting in various crystal fields. (Adapted from [56]) 31
Figure 1.12: Schematic representation of the valence and spin states of Cobalt in three different oxidation states..... 33
Figure 1.13: SOC in Rydberg energy units as a function of atomic numbers by different models. (Adapted from [61])..... 34
Figure 1.14: SOC and compressive strain effect on energy levels of Iridates. 35
Figure 1.15: (a) The Anderson model of magnetic impurity assumes that it has just one electron level below the Fermi energy of the metal (red). This level is occupied by one spin-up electron (blue). Quantum mechanically, the spin-up electron may tunnel out of the impurity site briefly and be replaced by an electron from the metal, resulting in a spin-flip of impurity, (b) Many such

events combine to produce the Kondo effect, which leads to the appearance of an extra resonance at the Fermi energy. (Adapted from [65]) 37
Figure 2.1: (a) Typical thin film deposition system in vacuum., (b) The growth models of the thin films. (Adapted from [67]) 38
Figure 2.2: Residual (a) tensile, (b) compressive strain in a thin film. F_i are stress-induced forces and M is the induced bending moment. (Adapted from [70]) 40
Figure 2.3: A schematic of the MBE system in Auburn FINO Lab. (Adapted from [74]) 42
Figure 2.4: Schematic illustration of the essential parts of an MBE growth system. (Adapted from [68]) 45
Figure 2.5: Auburn FINO Lab MBE system. 46
Figure 2.6: The manipular with the growth stage. 47
Figure 2.7: Sr effusion cell. 47
Figure 2.8: The XPS chamber and sample holder 47
Figure 2.9: A top-view of the effusion cells once the manipular removed. 47
Figure 3.1: RBS spectra from two TaSix, films of different thicknesses on Si substrates. Particles scattered from Ta at the $TaSi_x$ - Si interface of the 230-nm film have a final energy of about 1.9 MeV (labeled B) after escaping from the sample, while for the 590-nm film, they have a final energy of about 1.7 MeV (labeled C). (Adapted from [89]) 51
Figure 3.2: (left) In IBM geometry incident beam, exit beam and surface normal of the sample are in the same plane, (right) In Cornell geometry, incident beam, exit beam and the rotation axis of the sample are in the same plane. (Adapted from [90]) 52
Figure 3.3: Kinematic factor as a function of atomic mass. 52
Figure 3.4: RBS analysis using SIMNRA software. 52
Figure 3.5: A simple RHEED set up. (Adapted from [97]) 53
Figure 3.6: Diffractometer combined with molecular beam epitaxial growth. The glancing angle of incidence ϑi is varied by a combination of electrostatic deflection and sample motion. The diffracted beams are scanned across a phosphor screen by a small magnetic field. The diffracted intensity is measured with a photomultiplier. (Adapted from [94]) 54
Figure 3.7: A unit cell with three-unit vectors. (Adapted from [99]) 56

Figure 3.8: (a) The five plane lattices (left) and plane reciprocal lattices (right) indicating the corresponding unit cells, (b) reciprocal space in 1D, 2D and 3D. (Adapted from [98] and [100]) 57
Figure 3.9: Bragg scattering from two parallel planes. Ray 2 travels $2d_{hkl} \sin \theta$ further than Ray 1. Bragg scattering from two parallel planes. (Adapted from [99] 57
Figure 3.10: Example of Ewald construction (a) A two-dimensional reciprocal lattice and a slide of an Ewald sphere with radius |**K**in |, (b) The intersection of the rods (in reciprocal lattice) and the Ewald sphere conserves both energy and parallel momentum. The intersection of the Ewald sphere and the single plane of the rods, shown, is a circle. (Adapted from [94] and [99]) 58
Figure 3.11: Kikuchi lines in a $SrIrO_3$ film. 59
Figure 3.12**:** Schematics of various types of realistic surfaces: real-space morphologies, corresponding reciprocal space representations, and associated RHEED patterns. (Adapted from [95]) 60
Figure 3.13: Components of a diffractometer. (Adapted from [102]) 63
Figure 3.14: Schematic of the notation used for the angles and degrees of freedom in a typical diffractometer used for thin film measurements. (Adapted from [102]) 64
Figure 3.15: Basic setup for a coupled scan. (Adapted from [103]) 65
Figure 3.16: Geometry of a standard XRR measurement. Solid rays are incident and reflected X-rays at the surface, and dashed rays are refracted X-rays in the thin film. (Adapted from [105]) 66
Figure 3.17: Reciprocal space maps of hetero-epitaxial layer. (Adapted from [107]) 67
Figure 3.18: The process of X-ray core-level photoemission. (Adapted from [111]) 70
Figure 3.19: Schematic of an XPS chamber configuration. (Adapted from [112]) 71
Figure 3.20: An example of a survey scan (only Ir and O elements are labeled). 72
Figure 3.21: Co 2p multiplex with two peaks due to spin-orbit coupling (dashed orange circles represent corresponding satellite peaks). 72
Figure 3.22: X-ray interactions with matter. (Adapted from [55]) 75
Figure 3.23: (a) Schematic diagram of the different X-ray excitations giving rise to K, L and, (b) A schematic of the photoexcitation process, indicating the threshold energy E_0, kinetic energy of the photoelectron, E_K, and the energy of the incident X-ray photon E. (Adapted from [55]) 75
Figure 3.24: Transitions in Co L and K edges. 76
Figure 3.25: Dipole and Quadrupole transitions of Co K edge in $LaCoO_3$. 77

Figure 3.26: Ligand-to-metal charge transfer induced shake-down transition (orange arrow). (Adapted from [55]) 78
Figure 3.27: Schematic diagrams of processes relevant to $1s \rightarrow 4p_z$ and LMCT shake-down transition. (Adapted from [55]) 79
Figure 3.28: (A) A schematic of the shake-up transition. (B) The Ni K-edge XAS of NiO, where broad features marked with the orange arrows are thought to be shake-up transitions. (Adapted from [55]) 79
Figure 3.29: XAS detection modes. (Adapted from [122]) 81
Figure 3.30: An example of search light effect in K-edge. (Adapted from [123] 82
Figure 3.31**:** Polarization-dependent core to valence transition intensities for **E** along the principal coordinate axes. The intensities shown for the four basic symmetry cases: $s \rightarrow p_i$ (i = x, y, z), $p \rightarrow d_{ij}$ ($i \neq j$ = x, y, z), $p \rightarrow d_{x2-y2}$ and $p \rightarrow d_{3z2-r2}$. All intensities are per orbital per spin in units of atomic radius squared (AR^2). (Adapted from [124] 82
Figure 3.32: A schematic diagram of a STEM instrument. (Adapted from [128] 83
Figure 3.33: (a) interactions between the electron beam and the target material, (b) Schematic diagram of STEM detector set up. (Adapted from [129] and [130]) 85
Figure 4.1: Elemental Sr Source. 87
Figure 4.2: Rutherford backscattering spectroscopy simulation. 88
Figure 4.3: Plasma annealing effect. 89
Figure 4.4: (a) RHEED and (b) XRD of $SrCoO_3$ 90
Figure 4.5: (a) Sr rich, (b) Co Rich, (c) Ideal Stoichiometric $SrCoO_3$ film. 91
Figure 4.6: $SrCoO_3$ film crystalline quality (a) without (b) with $SrIrO_3$ capping 91
Figure 4.7: (a) Co 2p, (b) Co 3p XPS data of $SrCoO_3$ with references samples. 92
Figure 4.8: (a) Co L-edge XAS data of $SrCoO_3$ films (b) Reference data- adapted from [139]. . 93
Figure 4.9: (a) O K-edge XAS data of 2 $SrCoO_3$ films (b) Reference data- adapted from [32]. . 94
Figure 4.10: Crystal structure data of $SrIrO_3$. (Adapted from [76]) 95
Figure 4.11: Sr rich (top) and Ir rich (bottom) $SrIrO_3$ films. 95
Figure 4.12: (a) Schematic diagram of the (b= 10 uc) superlattice film, (b) corresponding RHEED data 97
Figure 4.13: STEM and RSM data of the (b= 10 uc) superlattice film. 98

Figure 4.14: XRD data of the three superlattices (XRR fitting is in inset), (b) XRD of (b= 10 uc) SL film in 6 months. 98
Figure 4.15: (a) RHEED, (b) XRD and (c) XPS of Sr_2CoIrO_6 with HAXPES of (b= 10 uc) superlattice film. 99
Figure 4.16: (a) RHEED, (b) XRD data of $LaCoO_3$ film of 10-unit cells of thickness. 100
Figure 4.17: an image of residuals from a fire occurred during Ir source refilling. 101
Figure 5.1: Crystal structure and the corresponding bond lengths of the superlattice structures (Blue= Co, Yellow= Ir) 105
Figure 5.2: The glancing angle stage with 8 spinners (sample positions). (Adapted from [166]) 107
Figure 5.3: Background subtraction in IP Ir-L2 edge for the SL-3 sample. 108
Figure 5.4: XAS Co K-Edge data for superlattice samples (a), (c) In-plane data (Normalized and First derivative of spectra), (b)(d) Out-of-plane data (Normalized and First derivative of spectra). 110
Figure 5.5**:** XAS Co K-Edge data for Double Perovskite samples (a), (c) In-plane data (Normalized and First derivative of spectra), (b)(d) Out-of-plane data (Normalized and First derivative of spectra)..... 111
Figure 5.6: (a) Ir L_2 edge of the superlattices, (b) Ir L_3 edge of the double perovskites. 112
Figure 5.7: X-ray linear dichroism data for (a) Ir L_2 edge of superlattices, (b) Ir L_3 edge of double perovskites (c) Co K edge of the superlattices..... 113
Figure 5.8: Co K Pre-edge fitting for the superlattices. 114
Figure 5.9: Co K Pre-edge fitting for the double perovskites. 114
Figure 5.10: References with significant dichroic contributions to the pre-edge (a) Calculated Ti K edge spectra at the of a-TiO2 for different angles of incidence θ with the sum of dipolar and quadrupolar components (thick lines) and with quadrupolar components only. (Adapted from [180]), (b) Mn K pre-edge amplitude variation of the $[Rh(en)_3][Mn(N)(CN)_5].H2O$(Mn(V)-nitrido) compound that follows a $\cos^2 \theta$ trend. (Adapted from [179]) 116
Figure 5.11: Shoulder peaks in the Co K edge data. 117
Figure 5.12: Second derivative of IP vs OOP data for selected films. 119
Figure 6.1: A parallelepiped sample with thickness d. (Adapted from [190]) 121
Figure 6.2: Hall resistivity data of the $SrCoO_3$ film. 122

Figure 6.3: Temperature dependent resistivity (left) and Kondo scattering term (right-top) for SIO films on different substrates. (Adapted from [76]) 123
Figure 6.4: Longitudinal resistivity vs Temperature (a) Zero Field cooling (ZFC), (b) comparison of ZFC and FC for the (b= 8 uc) superlattice sample, (c) Hall co-efficient versus Field. 124
Figure 6.5: Branching ratio values of pure SCO (left) and SCO/SIO superlattice (b=10 uc) (right). 125
Figure 7.1: RHEED of a representative superlattice and XRD of 3 superlattices in Set 1. 126
Figure 7.2: STEM and EDX from of the sample SIO/ $[SCO/SIO]_3$/ LSAT (b= 10 uc) from Superlattice set 1. 127
Figure 7.3: Transport data of Set 1 along with a superlattice of $LaCoO_3$-$SrIrO_3$ and pure $SrIrO_3$. 127
Figure 7.4: RHEED figures of (a) SL 1, (b) SL 2, (c) STEM image of SL 2, (d) RSM data of (b= 8 uc) SL of Set 2. 128
Figure 7.5: XRD (left) and XRR (right) data of 3 superlattices of Set 3. 128
Figure 7.6: Co K edge of $SrCoO_x$ in (most likely in the BM Phase). 129

List of Abbreviations

MBE	Molecular Beam Epitaxy
SL	Superlattice
RBS	Rutherford Backscattering Spectrometry
RHEED	Reflection High-Energy Electron Diffraction
XPS	X-ray Photoelectron Spectroscopy
XRD	X-ray Diffraction
XRR	X-ray Reflectivity
XAS	X-ray Absorption Spectroscopy
XANES	X-ray Absorption Near Edge Spectroscopy
STEM	Scanning Transmission Electron Microscopy
EELS	Electron Energy Loss Spectroscopy
SCO	$SrCoO_3$
SIO	$SrIrO_3$
SCIO	Sr_2CoIrO_6
LCO	$LaCoO_3$
STO	$SrTiO_3$
LSAT	$(LaAlO_3)_{0.3}$ $(Sr_2AlTaO_6)_{0.7}$

Chapter 1 : Backgrounds and Motivation

1.1 Introduction

Thin film science involves depositing a small amount of material- often as a continuous layer- onto a substrate to tailor its properties for specific applications. Epitaxial thin film refers to the growth of a crystalline layer on (*epi*) the surface of a crystalline substrate, where the crystallographic orientation of the substrate surface imposes a crystalline order (*taxis*) onto the thin film. This implies that film elements can be grown, up to a certain thickness, in crystal structures differing from their bulk [1,2].

Thin films provide a versatile platform for exploring novel physical phenomena, with charge transfer emerging as a key driving mechanism. This dissertation focuses on charge transfer phenomena, and this chapter presents an overview of thin film systems relevant to this dissertation, along with the corresponding physics.

1.2 Complex oxides

Complex oxides are compounds consisting of oxygen and usually with a greater number of chemical elements than conventional semiconductors, having more complex crystal structures [3]. These materials display the full spectrum of electronic, optical, and magnetic properties- including insulating, semiconducting, metallic, superconducting, ferroelectric, pyroelectric, piezoelectric, ferromagnetic, multiferroic, and nonlinear optical behaviors- all within structurally compatible frameworks. This remarkable diversity makes complex oxides highly promising for advanced electronic applications [4].

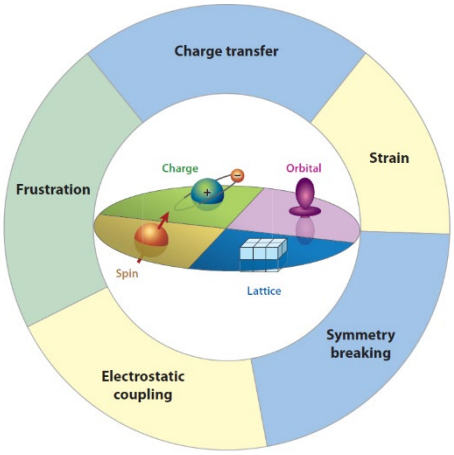

Figure 1.1: Interactions between different degrees of freedom lead to rich physics in complex oxides. (Adapted from [6])

The rich variety of phenomena observed in oxides is largely driven by the role of oxygen. Oxygen's strong electronegativity draws electrons away from neighboring atoms, creating intense local electric fields at the atomic scale. These fields can give rise to substantial electron electron-correlations in neighboring atoms, leading to rich physics phenomena [3,5]. As depicted in Figure 1.1 [6], additionally, the complex interactions between charge, orbital, spin, and lattice degrees of freedom can cause drastic changes in the electronic states upon subtle extrinsic perturbations, leading to exciting new physics [6,7].

1.2.1 Perovskite oxide thin films and heterostructures

One particular complex oxide- perovskite-structured transition metal oxide- has attracted significant attention due to their structural versatility and rich physical properties. The typical chemical formula of a perovskite is ABO_3, where A and B represent two different cations: A-site cations are typically large and 12-coordinated. B-site cations are smaller and 6-coordinated [8]. The ideal perovskite has a cubic lattice (Figure 1.2) [9], where a is the cubic unit cell parameter. In this ideal structure, atoms are in contact with one another, forming a highly symmetric arrangement.

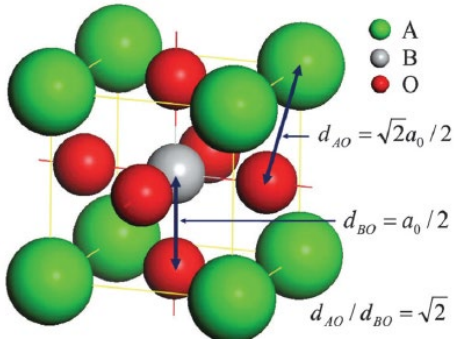

Figure 1.2: An ideal Perovskite structure and the corresponding structure parameters. (Adapted from [9])

However, just few compounds exhibit the perfect cubic structure, many oxides adopt distorted variants with lower symmetry, such as orthorhombic, tetragonal, monoclinic, rhombohedral etc. These distortions arise due to differences in the ionic radii of the A and B cations. They influence the electronic structure, dipole moments, and crystal field effects, making them critical to the material's behavior [10].

Many perovskite oxides exhibit significant oxygen or cation deficiencies. Despite these imperfections, they are still classified as perovskites due to their large lattice energy and structural framework [8]. One typical polymorph of the perovskite structure is brownmillerite ($A_2B_2O_5$) structure. Brownmillerite (BM) is an oxygen deficient type of perovskite in which the

oxygen vacancy is ordered. The unit cell contains BO_6 and BO_4 units in an ordered arrangement. Because of the oxygen deficiency, the coordination number of A-site cations decreases to 8.

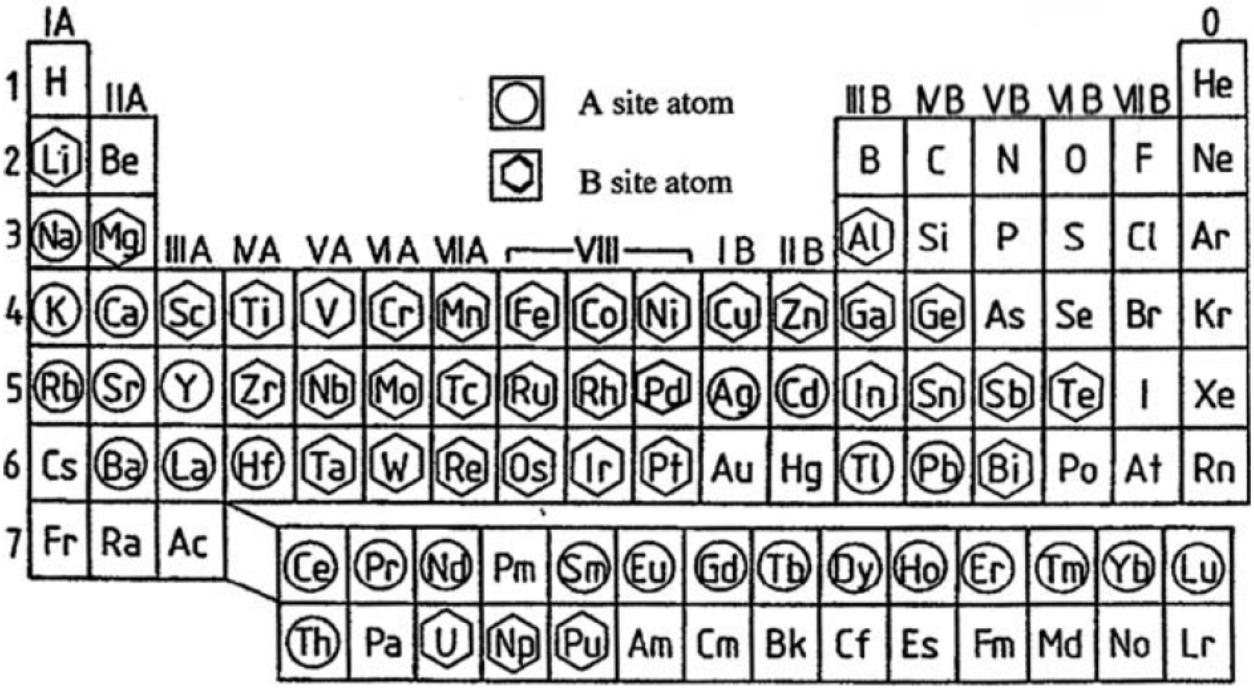

Figure 1.3: Chemical elements that can occupy sites in the perovskite structure. (Adapted from [8])

As shown in Figure 1.3 [8], various combinations of cation charges have been observed in perovskite compounds, such as 1+5, 2+4, and 3+3. These combinations allow a wide range of chemical elements to be accommodated within the perovskite structure. Given the chemical and structural compatibility, this malleable structural host offers an opportunity to customize electronic, magnetic, and optical properties in ways not possible with conventional semiconductors [4]. At the same time, the structural compatibility of these compounds allows them to be stacked on top of each other into complex multifunctional heterostructures with relative ease [6]. This way, in their interfaces, their properties can be further tuned through symmetry breaking, charge transfer, strain, and other effects.

1.3 Interfacial charge transfer and its significance

Physics phenomena at interfaces of solids have stimulated intense research activity in recent decades. In his Nobel Lecture in 2000, Herbert Kroemer said, "the interface is the device", referring to the remarkable properties found in the interface of two layers.

When two different transition-metal oxide (TMO) thin films are stacked together, in certain cases, charge transfer can occur from one film to the other. Consequently, the properties of the interface and nearby atomic layers can be fundamentally different from the constituent layers due to a modification of the d-orbital occupancy [1].

Interfacial charge transfer has been established experimentally as a powerful mechanism that can induce emergent phenomena. A classic example is the discovery of high mobility two-dimensional electron gas in the interface of $LaAlO_3/SrTiO_3$, although both constituent layers are wide band gap insulators [11]. Other examples include observation of interfacial ferromagnetism in superlattices composed of antiferromagnetic and paramagnetic layers [12–14], High-temperature superconductivity [15] etc. A list of emergent phenomena in oxide heterostructures is shown in Table 1.1 [16].

Table 1.1: Different charge transfer mechanisms in oxide heterostructures. (Adapted from [16])

Mechanisms	**Examples**	**Emergent Phenomena**
Polarity difference	$LaAlO_3/SrTiO_3$	The interface is metallic, magnetic, and superconducting, although the constituents are insulators in bulk.
Occupancy difference	$LaTiO_3/SrTiO_3$	The interface is metallic, although $LaTiO_3$ is a Mott insulator and $SrTiO_3$ is a band insulator.
Electronegativity difference	$LaTiO_3/LaNiO_3$	Ni at the interface is in a d^8 Mott insulating state, although Ni in $LaNiO_3$ is in a d^7 metallic state.
	$LaTiO_3/LaNiO_3/LaAlO_3$	Ni at the interface has a huge orbital polarization, although Ni in $LaNiO_3$ has negligible orbital polarization.
	$LaMnO_3/LaNiO_3$	The interface can be either insulating or metallic depending on the thickness of $LaMnO_3$ and $LaNiO_3$, although $LaMnO_3$ is an insulator and $LaNiO_3$ is a metal.
	Ba_2VFeO_6	Ba_2VFeO_6 is ferroelectric although both $BaVO_3$ and $BaFeO_3$ have cubic structures (not ferroelectric).
	$SrVO_3/SrMnO_3$	Mn at the interface is doped and becomes metallic although $SrMnO_3$ is an insulator.
	Manganite/Cuprate	At the interface, Cu has a multi-orbital Fermi surface, although it is single-band in bulk; and Mn forms different magnetic domain structures from bulk.

1.4 Theory of charge transfer in complex oxides

There are established frameworks such as Anderson's or the Schottky-Mott rule to explain charge transfer in semiconductors [17,18]. However, the application of these rules to transition metal oxides remains challenging because work functions in TMOs are extremely sensitive to specific surface terminations and microscopic details of the surface [19]. Strong correlations in TMOs make calculating electronic structure more challenging, leading to a search for a more general theory [16]. Experimental verification of existing theories is critical towards advancing this effort.

Zhong and Hansmann developed a model to predict both magnitude and direction of charge transfer in interfaces of complex oxides [17]. They pursued this goal by setting a continuous oxygen matrix in the interface of two perovskites $ABO_3/AB'O_3$, as shown in Figure 1.4 [20]**.** This results in a mismatch of the Fermi energy, as shown in Figure 1.5(a) and acts as a driving force for charge transfer between the layers**.** The results of their density functional theory (DFT) calculations are summarized in Figure 1.5(c**)**, which shows the average energy of oxygen 2p states (filled symbols) and the average energy of partially filled d orbitals (empty symbols) with respect to the Fermi level. A prediction of the theory is that, given the monotonous behavior of ε_p within one group over different periods, electrons will also be transferred from the heavier to the lighter B elements.

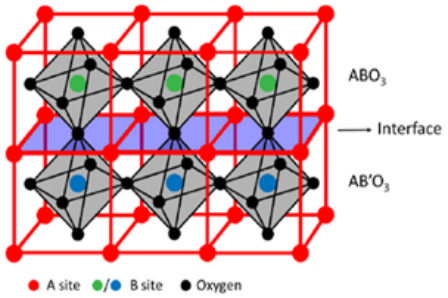

Figure 1.4: Oxygen continuity in the interface. (Adapted from [20])

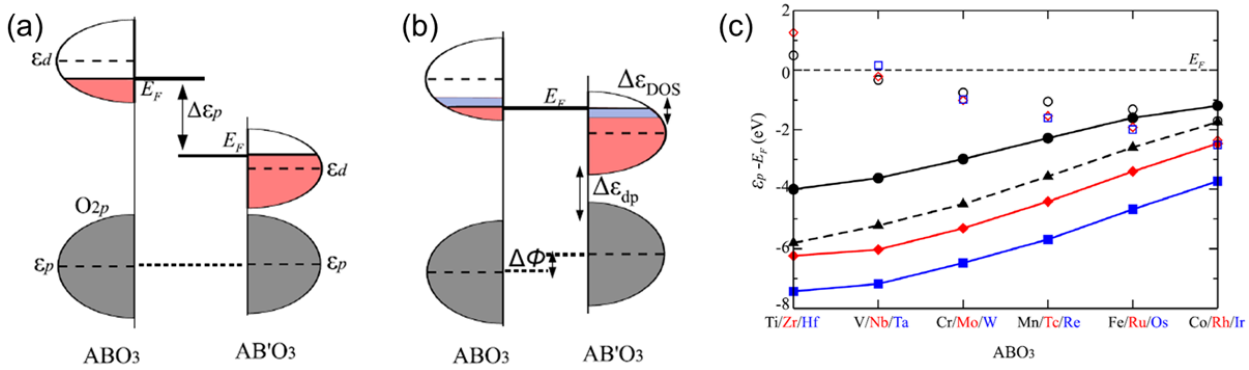

Figure 1.5: (a) Alignment of oxygen states at the interface, (b)The final equilibrium state. ε_p and ε_d are the local energy levels of oxygen p and TM- d states, (c) DFT reference data for $SrBO_3$. (Adapted from [17])

Therefore, the theory suggests that in the superlattice consisting of $SrCoO_3$ (SCO) and $SrIrO_3$ (SIO), shown schematically in Figure 1.6, Ir will donate electrons to Co. The authors implied similar conclusions for Sr_2CoIrO_6 double perovskites, which consists of SIO/SCO layers in the (111) direction [21]. Motivated by their work, the superlattice system was investigated both computationally using density functional theory (DFT) modeling and experimentally through molecular beam epitaxy (MBE) synthesis and spectroscopic characterization, while the double perovskite was studied experimentally. The interface study of 5d $SrIrO_3$ (SIO) and 3d $SrCoO_3$ (SCO) has potentiality of producing rich physics arising from interplay of strong electron correlation due in cobalt-based [22] and strong spin–orbit coupling in iridium-based systems [23,24].

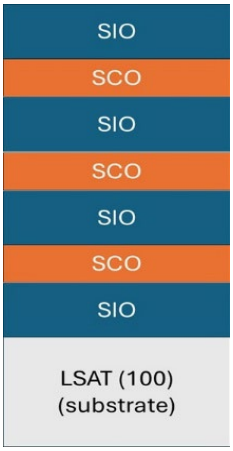

Figure 1.6: A schematic of an SIO/SCO superlattice.

1.5 About $SrCoO_3$ and $SrIrO_3$ thin film systems

$SrCoO_3$ (SCO) is a ferromagnetic metal with a Curie temperature between 280K - 305K [25–27]. It crystallizes in a cubic perovskite structure in the space group Pm-3m [27]. However, due to the multivalent nature of Co, the perovskite (P-SCO) phase can readily degrade into the brownmillerite $SrCoO_{2.5}$ (BM-SCO) phase- an antiferromagnetic insulator [28,29]. Both of these configurations are shown in Figure 1.7 [30], which depicts the picture of oxygen vacancy/injection to transform from one phase to the other. Although $SrCoO_3$ thin films are widely synthesized to study its intrinsic properties, its metastable nature poses significant challenges in its potential for real-life applications.

Density functional theory (DFT) predict that, a moderate tensile strain of 2.0% induces a transition from a ferromagnetic (FM) metallic state to an antiferromagnetic (AFM) metallic state [31]. However, experimental results from highly tensile-strained samples show contrasting behavior [32,33], though the authors [32] observes a metal-to-insulator transition along with the increase of the tensile strains, consistent with theoretical predictions. These predictions suggest that $SrCoO_3$ can be engineered near a strain-tunable phase boundary, and an alternative mechanism, such as charge transfer has the merit for investigation.

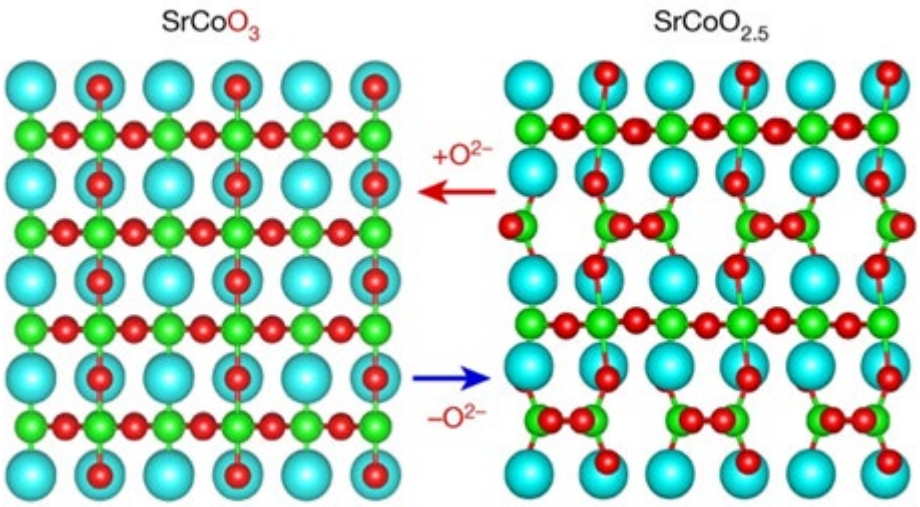

Figure 1.7: $SrCoO_x$ film in perovskite (left), and brownmillerite (right) phase. (Adapted from [30])

On the other hand, $SrIrO_3$ (SIO) is a paramagnetic semi-metal crystallizing in Pbnm structure, representing the end member of the $Sr_{n+1}Ir_nO_{3n+1}$ Ruddlesden-Popper series with $n= \infty$ [34]. Within this series, as the number of neighboring Ir^{4+} atoms increase from 4, 5 to 6, the 5d bandwidth broadens modifying the ground state, from a Mott insulator (Sr_2IrO_4) to a weak insulator ($Sr_3Ir_2O_7$), and ultimately to a correlated metal ($SrIrO_3$). In thin $SrIrO_3$ (SIO) films the strain effect can induce a metal-insulator transition [35,36].

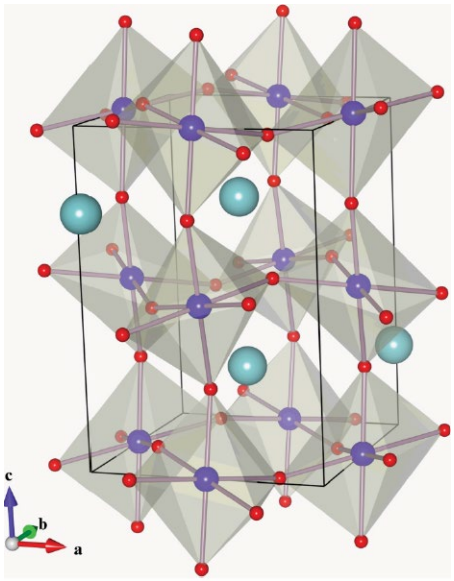

Figure 1.8: Crystal structure of orthorhombic perovskite $SrIrO_3$. Sr, Ir, and O atoms are shown in aqua, blue, and red. (Adapted from [24])

Figure 1.8 illustrates the crystal structure of orthorhombic perovskite $SrIrO_3$, where Sr, Ir, and O atoms are represented by aqua, blue, and red spheres, respectively [24]. As shown, the IrO_6 octahedra are rotated about the z-axis and tilted along the [110] direction. These distortions result in four formula units per unit cell and lead to a deviation from ideal octahedral symmetry. The rotation angle of the IrO_6 octahedra for $SrIrO_3$ films grown on $SrTiO_3$ substrate (~1% lattice mismatch) is approximately $\alpha \approx 15.2°$ (14.4°) [37] .

Such octahedral distortions are commonly observed in iridate systems and are closely linked to their emergent quantum phenomena [37,38].

Iridates have recently attracted significant attention due to their strong spin-orbit interactions (SOI) and the consequent influence on their physical properties. In iridates, under octahedral the O_h symmetry, the five-degenerate d-orbitals split into a lower-energy t_{2g} and a higher-energy e_g doublet (explained in the sub-section 1.7.1). In the strong spin-orbit coupling (SOC) limit, the t_{2g} manifold further splits into states characterized by an effective total angular momentum: a $J_{\text{eff}} = \frac{3}{2}$ (quartet) and a $J_{\text{eff}} = \frac{1}{2}$ (doublet) [24,39]. The $J_{\text{eff}} = \frac{3}{2}$ states lie lower in energy and the states are separated by an energy gap $\frac{3\lambda}{2}$ [34]. In the $J_{\text{eff}} = \frac{3}{2}$ multiplet, the spin and orbital angular momenta are aligned (parallel), whereas in the $J_{\text{eff}} = \frac{1}{2}$ multiplet, they are anti-aligned (antiparallel) [40].

1.6 Significance of 3d-5d interface study and $SrCoO_3$ / $SrIrO_3$ heterostructures

Superlattices are a class of engineered thin film heterostructures composed of alternating layers of two or more dissimilar materials, typically with individual layer thicknesses on the order of a few nanometers. These periodic structures are designed to exploit quantum confinement and interfacial effects, enabling the emergence of novel physical phenomena not present in the bulk constituents [41–43]. These structures further allow for precise control over band alignment, strain, and orbital hybridization. This dissertation investigates superlattice structures composed of alternating layers of $SrCoO_3$ and $SrIrO_3$, with a final capping layer of $SrIrO_3$ to stabilize the topmost $SrCoO_3$ layer. A schematic representation of the structure is provided in Figure 1.6.

A unique feature of iridates is the presence of strong spin- orbit coupling (SOC), which competes with crystal field (FC), electron-electron (U) and other interactions, as shown in

Table 1.2, leading to highly tunable and novel electronic and magnetic ground states [34,44]. The delicate balance of these interactions is influenced by factors such as local atomic configuration [45], structural dimensionality [46], and chemical doping [47,48]. Studying charge transfer in superlattices comprised of $SrIrO_3$ therefore provides an excellent platform to probe the intricate interplay of the competing interactions that can offer wide-ranging opportunities for

the discovery of exotic states and engineer novel device functionalities. On the other hand, electron-electron interactions play a pivotal role in driving emergent quantum phenomena in strongly correlated systems [49]. Therefore, studying a strongly spin-orbit coupled 5d $SrIrO_3$ in a superlattice with a strongly correlated 3d $SrCoO_3$ [22,44] can further make the system more interesting and give rise to rich physics. For example, a manipulation of the magnetic anisotropy has been demonstrated in the ferromagnetic $La_{2/3}Sr_{1/3}MnO_3$ (LSMO) by tuning the $SrIrO_3$ dimensionality [50]. In superlattices comprised of 3d $La_{1-x}Sr_xMnO_3$ ($0 \leq x \leq 1$) and 5d $SrIrO_3$, ferromagnetism is observed despite the fact that $La_{1-x}Sr_xMnO_3$ is antiferromagnetic for $x > 0.5$ [51].

Table 1.2: A comparison of relative strengths among different competing interactions in 3d, 4d, and 5d systems. (Adapted from [34])

System	Coulomb repulsion U (eV)	SOI strength λ (eV)	Spin state	Relative strength
3d	5-7	0.01-0.1	HS	U > CF > λ
4d	0.5-3	0.1-0.3	LS / IS	U ~ CF > λ
5d	0.4-2	0.1-1	LS	U ~ CF ~ λ

Synthesis of 3d-5d superlattices and heterostructures where both constituent layers are metallic oxides remain largely unexplored [52]. Therefore, a comprehensive investigation of the SIO/SCO system can serve as an important step toward bridging this gap.

On the other hand, Sr_2CoIrO_6 (SCIO) can be viewed as a superlattice composed of alternating $SrCoO_3$ and $SrIrO_3$ layers in the (111) direction [21]. Therefore, it can provide another compelling platform to explore electronic and magnetic phenomena driven by the interplay of spin-orbit coupling, electron correlations, and structural distortions. Sr_2CoIrO_6 has been reported to crystallize in the monoclinic structure with the space group I2/m and pseudocubic lattice constants a = 0.3909 nm, b = 0.3925 nm, and c = 0.3921 nm [53]. A schematic of SCIO is shown in Figure 1.9 [21].

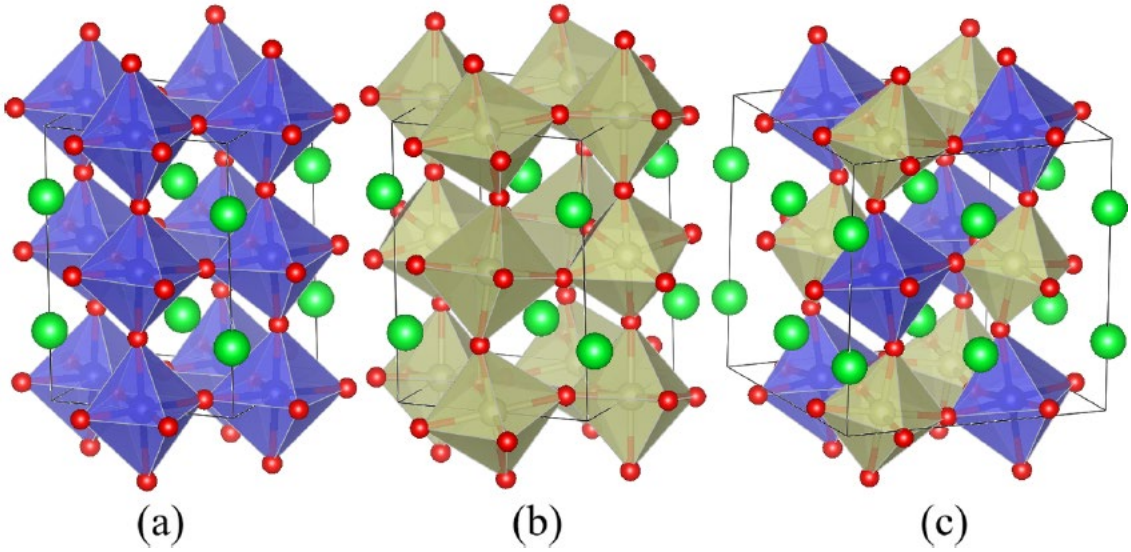

Figure 1.9: Structure of (a) $SrCoO_3$, (b) $SrIrO_3$, and (c) double perovskite Sr_2CoIrO_6. Sr, Co, Ir, and O ions are shown in green, yellow, blue, and red, respectively. (Adapted from [21])

Theoretically, SCIO has been predicted to exhibit an antiferromagnetic Mott insulating ground state, characterized by antiparallel alignment of Co and Ir magnetic moments along the [110] crystallographic direction [21]. While $SrIrO_3$ is a semimetal with a quenched spin and orbital moment, remarkably in SCIO, a substantial enhancement of the Ir magnetic moments has been predicted, with spin and orbital contributions of 1.21–1.25 μB and 0.13 μB, respectively [21]. However, experimental investigations using x-ray absorption spectroscopy (XAS) and x-ray magnetic circular dichroism (XMCD) at the Ir-$L_{2,3}$ edges, reports a nearly zero orbital contribution to the Ir magnetic moment [54].

A noticeable charge transfer from Ir to Co in the SCIO double perovskite has been reported [21], resulting in mixed valence state comprising predominantly Ir^{5+} ($J_{eff} = 0$) and Co^{3+} ($S = 2$) with a small portion of (~10%) Ir^{6+} ($S = 3/2$) and Co^{2+} ($S = 3/2$) [53,54].

1.7 Physics corresponding to cobaltite and iridate systems

1.7.1 Crystal field theory

Crystal Field Theory (CFT) describes the interaction between a central metal ion and surrounding ligands purely in terms of electrostatic forces. It assumes that ligands behave as point charges, creating an electrostatic field that interacts with the metal d-electrons through Coulombic repulsion, known as the crystal field. This field perturbs the degenerate energy levels of the metal ion's d-orbitals. Ligand field theory (LFT), a modification of crystal field theory additionally considered covalent bonding between the metal and its ligand [55]. LFT is essentially a molecular orbital approach that provides a more accurate description of bonding and electronic structure in coordination complexes. The basic idea can be explained in terms of a Co ion as follows.

A Co atom free from the influence of the rest of the universe would have five d orbitals of equal energy (degeneracy). However, when placed in a crystal environment, the surrounding negatively charged ligands generate an inhomogeneous electric field that lifts this degeneracy [5]. Let's consider six ligands approaching the metal ion symmetrically along the Cartesian axes, forming an Octahedral (O_h) geometry. Due to electrostatic repulsion between the ligand electrons and the metal's d-electrons, the five d-orbitals split into two energy levels: e_g and t_{2g} [56,57]. The e_g orbitals have lobes that point at the ligands and so will ascend in energy. The t_{2g} orbitals have lobes that lie between ligands and so will descend in energy.

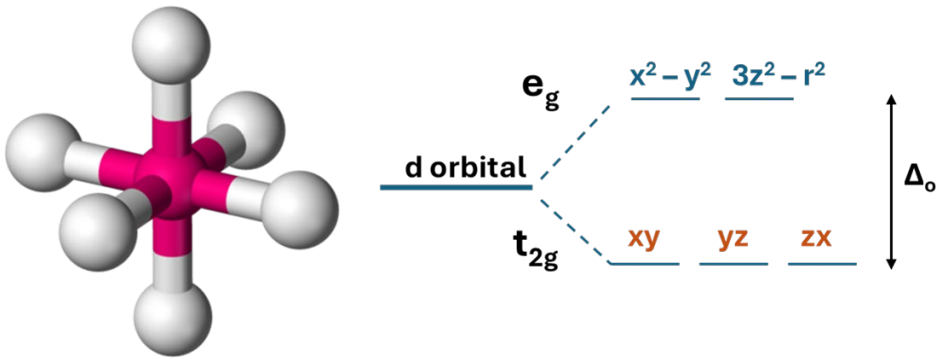

Figure 1.10: splitting of the degenerate d-orbitals. (Orbital shape has been adapted from [57)

The energy difference between these two sets (Δ_o), sometimes referred to as 10Dq, is called the ligand field splitting and given by [58]:

$$10\mathrm{Dq} = 10 \cdot \frac{35}{4a^5} \cdot \frac{2Z_L}{105} \langle R_{nl}(r)|r^4|R_{nl}(r)$$

The crystal field strength with O_h symmetry is therefore proportional to electron radial expectation [$\langle R_{nl}(r)|r^4|R_{nl}(r)\rangle$,], ligand bond length reciprocal quintic value a^{-5}, and ligand effective charge Z_L. When the two bonds in z- and z+ direction are prolonged or compressed in length as compared to four in-plane bonds, the O_h symmetry is distorted to D_{4h} tetrahedral symmetry.

The local structural symmetry of solid crystal material is denoted as specific point group. Group theory plays a major role in finding the degeneracy and the symmetry types of the electronic levels in the crystalline field. The type of new energy levels is dependent on the type of crystal potential, and the energy levels are often written in lowercase (e_g, t_{2g}) when referring to molecular orbitals.

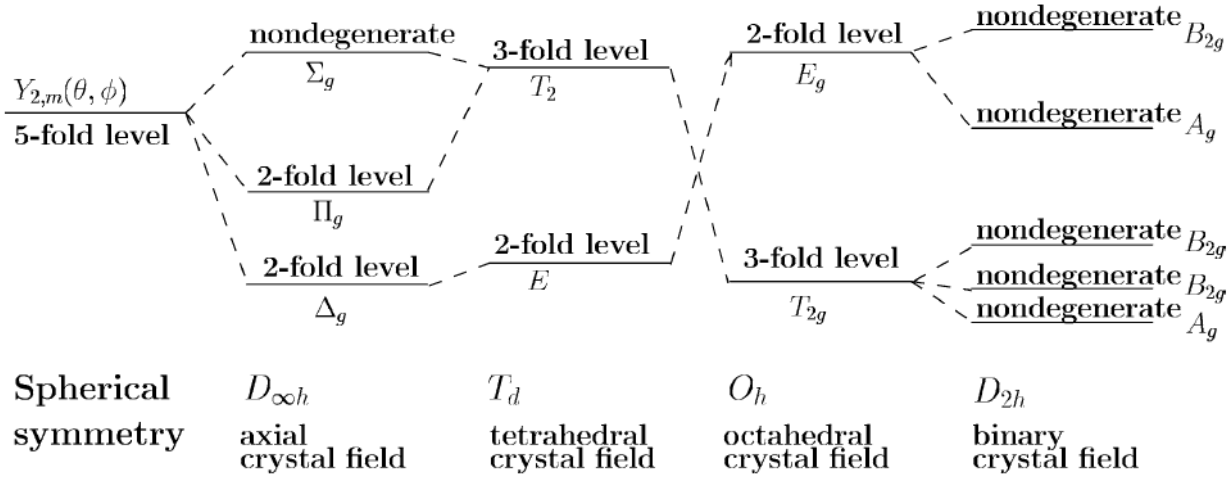

Figure 1.11: d-Level splitting in various crystal fields. (Adapted from [56])

1.7.2 Pairing energy (vs crystal field) and spin-state

The mean pairing energy P is the energy cost associated with placing two electrons in the same orbital, primarily due to electron- electron repulsion [55,59]. For configurations d^1 - d^3 and d^8 - d^{10} there is only one ground state configuration. For configurations d^4 – d^7, there are two possible filling schemes- high spin and low spin, depending on the relative strength of Δ_o and P. For a given metal ion, the pairing energy is relatively constant, so the spin state depends upon the magnitude of the field strength Δ_o [60]. If $\Delta_o > P$, electrons preferentially pair in the lower-energy t_{2g} orbitals a low-spin metal ion. Conversely, if $\Delta_o < P$, a high-spin state configuration appears to minimize pairing by spreading the electrons across both the t_{2g} and e_g levels [55,59].

First-row transition metals with weak-field ligands typically form high-spin complexes, while strong-field ligands favor low-spin configurations. The crystal field splitting energy (Δ_o) increases with the oxidation state and across the transition series. A general trend in Δ_o values for common metal ions is [55]:

$Mn^{2+} < Ni^{2+} < Co^{2+} < Fe^{2+} < V^{2+} < Fe^{3+} < Cr^{3+} < V^{3+} < Co^{3+}$

Meanwhile, 4d and 5d complexes are usually low spin, this is because the increased nuclear charge arising from larger atoms gives rise to a larger splitting.

Spin-state crossover in cobaltites:

Co oxides have garnered significant attention due to their diverse and intriguing physical and chemical properties. Among these, spin-state crossover is particularly notable, arising from the small energy differences between various spin configurations. The spin state crossover can lead to a change in the density of states near the Fermi level, resulting in unconventional transport properties such as the metal- insulator transition [22].

Co ions can exist in multiple valence states Co^{2+}, Co^{3+} and Co^{4+} spanning over three spin configurations: low-spin (LS), intermediate-spin (IS), and high-spin (HS) states, as shown in Figure 1.12. For instance, in the case of trivalent Co (Co^{3+}), which has six 3d electrons, the spin state depends on the electron configurations: $t_{2g}^6\ e_g^0$, $t_{2g}^5\ e_g^1$, and $t_{2g}^4\ e_g^2$, respectively, correspond to the LS, IS, and HS states of Co^{3+} [22]. The actual spin state adopted by the ion is determined by the competition between crystal field splitting energy and electron pairing energy as described above.

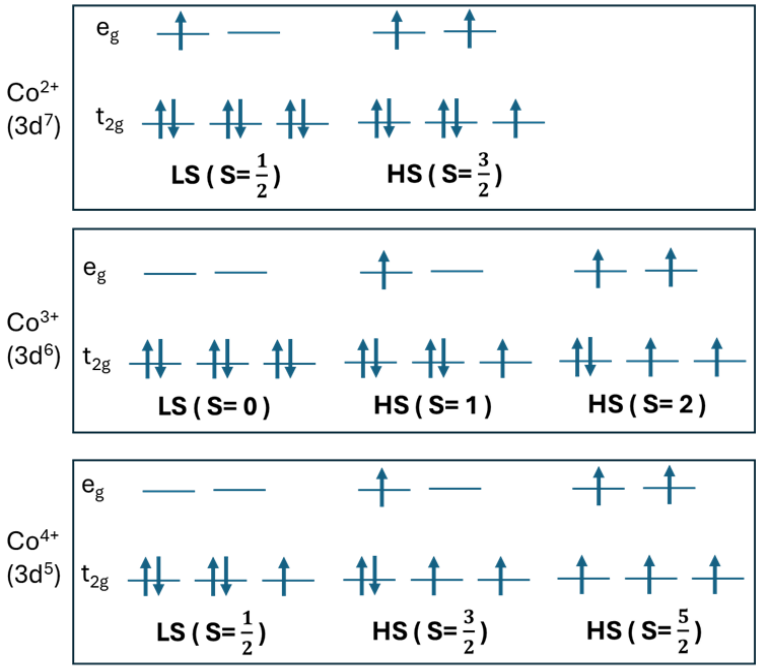

Figure 1.12: Schematic representation of the valence and spin states of Cobalt in three different oxidation states.

The HS state corresponds to the configuration with the maximum spin angular momentum (S = 2). The existence of IS Co^{3+} or IS Co^{4+} implies the wave function of 3d electron cannot be approximated by atomic 3d orbitals. Although this state is normally energetically unstable, it can be stabilized by lowering the crystal field symmetry (Jahn- Teller effect), which splits both t_{2g} and e_g orbitals, allowing an electron to occupy the e_g orbital and thereby realizing the IS configuration [22].

1.7.3 Spin-orbit coupling (SOC)

Spin-orbit interactions can have significant impact on the electronic, transport and magnetic properties of 4d and 5d transition metal oxides because of their larger atomic numbers. The interaction of electron's spin dipole moment with the orbital magnetic field in a central field of potential V(r) can be expressed as (including Thomson precession) [61,62]:

$$\mathcal{H}_{SO}(r) = \frac{r^{-1}}{2m^2c^2}\frac{\partial V(r)}{\partial r}$$

Here, m is the mass of the electron**, L** and **S** are the orbital and spin angular momentums operators, λ is the spin-orbit interaction strength.

For the hydrogenic wavefunctions R_{nl} (r), it can be found that [61]:

$$\lambda_{nl} = \int_0^\infty R_{nl}^2 \lambda(r) d^3r = \frac{\alpha^2 Z^4}{n^3 l(l+1/2)(l+1)} \mathrm{R_y}$$

Here, α is the Fine-structure constant, n and l are principal and orbital angular momentum quantum numbers, and R_y is Rydberg unit of energy. The above equation suggests that spin-orbit coupling strength increases as Z^4. However, in the solid, the outer electrons are the relevant electrons, whose quantum numbers nl change with Z. If one considers the outermost electrons for the atoms without worrying about nl, then Landau and Lifshitz have argued that the spin-orbit interaction strength should scale more like Z^2 [61].

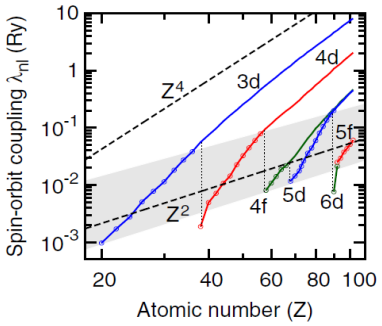

Figure 1.13: SOC in Rydberg energy units as a function of atomic numbers by different models. (Adapted from [61])

$$\lambda = A\alpha^2 Z^2 \mathrm{R_y}$$

where A is of the order of one. The spin-orbit coupling strength λ_{nl} for atoms is shown as a function of the atomic number Z in Figure 1.13. The color lines represent the calculated results by Herman and Skillman [61,63], obtained using the Hartree-Fock method. The upper dashed line represents the hydrogenic Z^4 dependence. For the outermost electrons- represented by circles and the shaded region- relevant in the context of solids, the quantum numbers n and l vary with Z^2. In this regime, the spin-orbit interaction increases more gradually, approximately following the Landau-Lifshitz Z^2 scaling (lower dashed line). As described in section 1.5, as a result of strong spin-orbit coupling in iridates, the t_{2g} orbitals splits into: $J_{\mathrm{eff}} = \frac{3}{2}$ (quartet) and a $J_{\mathrm{eff}} = \frac{1}{2}$ (doublet) states [24,39]. Figure 1.14 depicts SOC effect on iridates along with the effect of compressive strain, an important impact on the e_g energy levels [49].

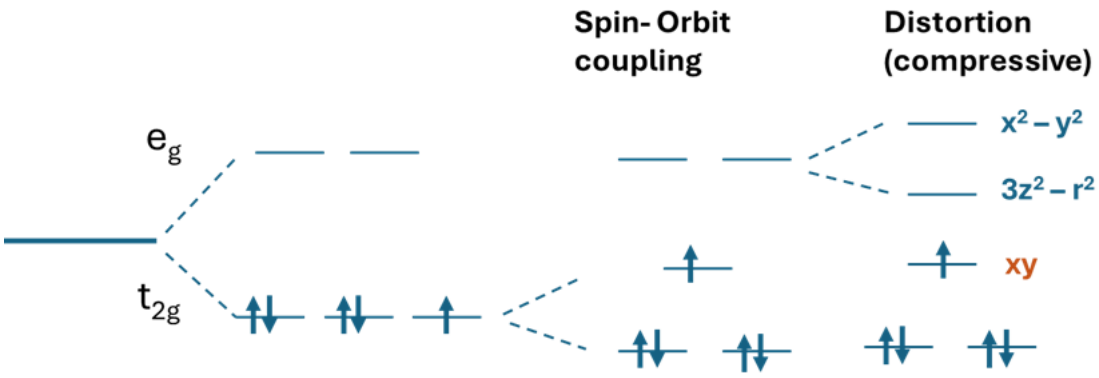

Figure 1.14: SOC and compressive strain effect on energy levels of Iridates.

1.7.4 The Kondo effect

The Kondo effect is a fundamental quantum many-body phenomenon that arises when magnetic impurities in a metal interact with conduction electrons. It was first explained by Japanese theorist Jun Kondo in 1964. Kondo discovered that when conduction electrons scatter off a localized magnetic impurity, the second-order term in the perturbation series could be much larger than the first, leading to a logarithmic increase in electrical resistance as temperature decreases [64]. This explained the observed upturn in resistance at low temperatures. However, the theory also makes the unphysical prediction that the resistance will be infinite at even lower temperatures. This was resolved in 1974 by Kenneth Wilson, who proved that below a characteristic Kondo temperature T_k, the impurity's magnetic moment becomes fully screened by conduction electron spins. This spin-screening is analogous to charge screening in metals, though the mechanisms differ [65].

The Kondo effect only arises when the defects are magnetic - in other words, when the total spin of all the electrons in the impurity atom is non-zero. The simplest model of impurity was introduced by Phil Anderson in 1961. This model describes a single electron level with energy ε_0. The electron can quantum mechanically tunnel from the impurity and escape provided its energy lies above the Fermi level, otherwise it remains trapped.

The mechanism underlying the Kondo effect involves exchange processes that can flip the impurity spin from up to down (or vice versa) [65]. Imagine a magnetic impurity (an ion) sitting in a metal lattice. The impurity's highest energy electron has an energy less than that of the

Fermi-sea of the lattice. In some circumstances this electron can tunnel to an unoccupied state near the surface of the Fermi-sea, however, this would require a substantial amount of energy (on the order of several eV) [65,66]. Classically, it is forbidden to take an electron from the defect without putting energy into the system. In quantum mechanics, however, the Heisenberg uncertainty principle allows such a configuration to exist for a very short time - around $h/|\varepsilon_o|$, where h is the Planck's constant. The magnetic impurity's electron can spontaneously tunnel from the impurity to the lattice's Fermi-sea within the timescale, if an electron from the Fermi sea tunnels to the available state in the impurity. In this case, the spins of these two electrons do not need to be identical - we can have a spin exchange. This spin exchange qualitatively changes the energy spectrum of the system Figure 1.15(a) (right) [65]. When many such exchange processes occur collectively, they generate a new quantum state known as the Kondo resonance, which has the same energy as the Fermi level [65,66]. Such a resonance is very effective at scattering electrons with energies close to the Fermi level. Since the same electrons are responsible for the low-temperature conductivity of a metal, the strong scattering contributes greatly to the resistance.

The Kondo resonance always aligns with the Fermi energy, regardless of the initial impurity level. The only requirement for the effect to occur is that the metal is cooled to sufficiently low temperatures below the Kondo temperature T_K. This phenomenon only occurs at low temperatures because the Fermi distribution (of filled vs unfilled states) broadens as temperature increases [66].

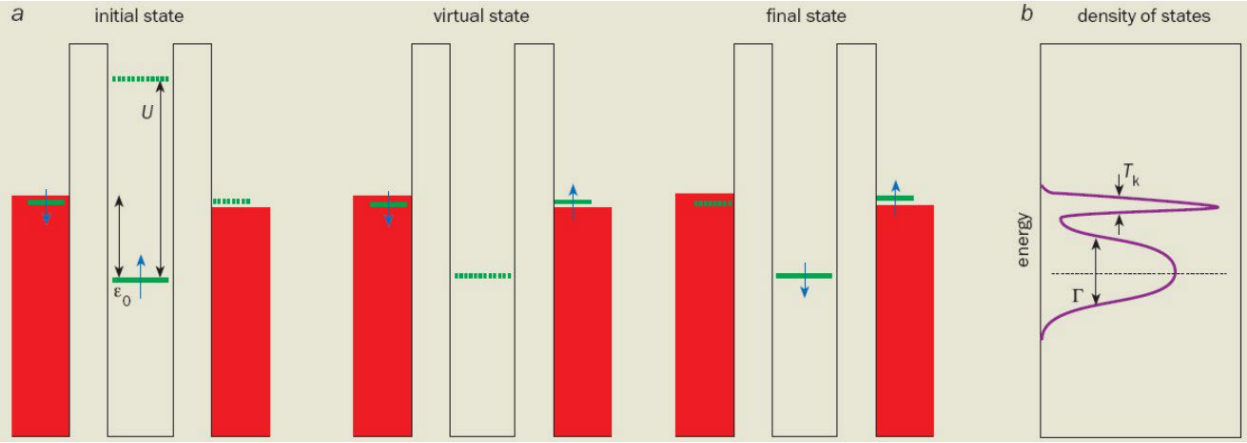

Figure 1.15: (a) The Anderson model of magnetic impurity assumes that it has just one electron level below the Fermi energy of the metal (red). This level is occupied by one spin-up electron (blue). Quantum mechanically, the spin-up electron may tunnel out of the impurity site briefly and be replaced by an electron from the metal, resulting in a spin-flip of impurity, (b) Many such events combine to produce the Kondo effect, which leads to the appearance of an extra resonance at the Fermi energy. (Adapted from [65])

Mathematically, using a perturbative Hamiltonian, the transition probability per unit time from an initial state a to a final state b is given to second order in the Born approximation by [64,66]:

$$W(a \to b) = \frac{2\pi}{\hbar}\delta(E_a - E_b)\left[H'_{ab}H'_{ba} + \sum_{c\neq a}\frac{H'_{ac}H'_{cb}H'_{ba} + \text{h.c.}}{E_a - E_c}\right]$$

where a, b and c are total states of the system, with respective energies E_a, E_b and E_c. The term of order H'^2 describes a single-step scattering process from a to b which is independent of temperature. The other term on order H'^3, includes processes with an intermediate state c. Expanding the second term and considering a possible two-step scattering processes for a spin-up electron with momentum k, the resistivity can be expressed as [64,66]:

$$\rho_{\text{spin}} = c\rho_M\left[1 + \left(\frac{3zJ}{\epsilon_F}\right)\log(T)\right]$$

Here, *c* is the concentration of impurities, J is an experimentally determined constant relating the interaction strength. This expression contains log(T) temperature dependence, first identified by Jun Kondo.

Chapter 2 : Thin Film Growth Method

2.1 Introduction

For the research presented in this dissertation, thin films were grown using the Molecular Beam Epitaxy (MBE) method in the *Films, Interfaces, and Nanostructures of Oxides* (FINO) lab at Auburn University (the lab has moved to the Department of Materials Science and Engineering at the University of Delaware). This chapter begins with a brief overview of thin films and epitaxial thin films. To provide context for the growth process, a schematic explanation of the MBE system is included, along with a description of a typical growth procedure. The chapter concludes with photographs of selected instruments used in the FINO lab.

2.2 Thin films and epitaxial growth

Thin films are low-dimensional materials formed by depositing atoms, molecules, or ions onto a substrate. Their growth is a complex, multi-stage process that begins with deposition and leads to the formation of a continuous film. Typically, thin films are deposited through thermal evaporation of source materials in a vacuum environment as shown in Figure 2.1 (a). A typical growth process of thin films on a substrate is illustrated in Figure 2.1(b) [67].

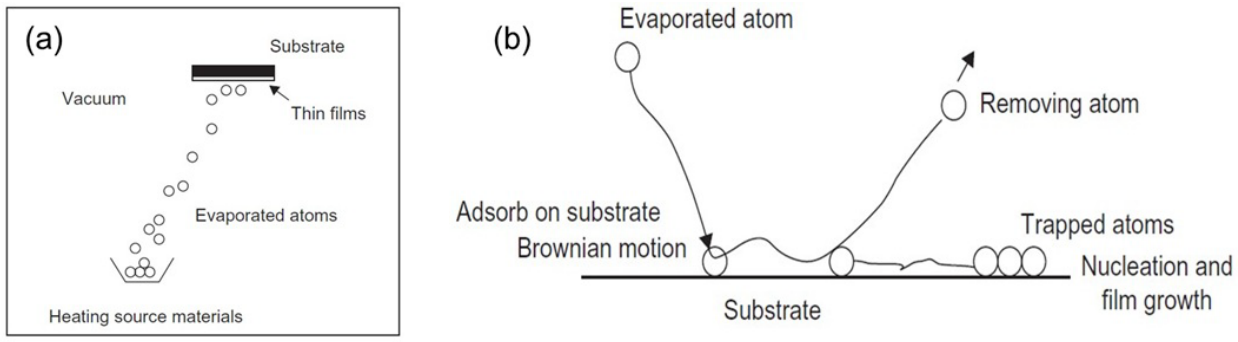

Figure 2.1: (a) Typical thin film deposition system in vacuum., (b) The growth models of the thin films. (Adapted from [67])

The thin film growth exhibits the following features [67]:

1. It starts a random nucleation process followed by nucleation and growth stages.

2. The nucleation and growth stages are dependent upon various deposition conditions, such as growth temperature, growth rate, and substrate surface chemistry.

3. The nucleation stage can be modified by external agencies, such as electron or ion bombardments.

4. Film microstructure, associated defect structure, and film stress depend on the deposition condition of the nuclear stage.

5. Crystal phase and crystal orientation of thin films are governed by the deposition conditions

Techniques for growing thin films in high vacuum can be broadly categorized based on the mode of material transport: physical or chemical [68]. In Physical Vapor Deposition (PVD), like the Molecular Beam Epitaxy, the material- either the compound or its constituent elements- is vaporized from polycrystalline or amorphous sources at high temperatures. These vaporized species are then transported through the vacuum chamber to the substrate as vapor or thermal-energy beams, without undergoing any chemical transformation. In contrast, Chemical Vapor Deposition (CVD) involves the generation of volatile precursor species containing the film's constituent elements. These species are introduced into the reactor as vapor streams or beams and transported to the reaction zone near the heated substrate. There, they undergo chemical reactions or thermal dissociation to produce the reactive species that contribute to film growth on the substrate surface.

Epitaxial thin film growth refers to the growth of a crystalline thin film on the surface of a crystalline substrate, where the crystallographic orientation of the substrate surface imposes a crystalline order (taxis) onto the thin film [69]. This implies that film elements can be grown, up to a certain thickness, in crystal structures differing from their bulk. When the film and substrate share the same crystal structure but have different lattice constants, the film experiences strain, resulting in a lattice mismatch that alters its lattice constant from the bulk value.

As shown in Figure 2.2 (a), the growing film may initially shrink relative to the substrate. However, since the film and substrate must remain bonded, the film stretches to match the substrate length, resulting in tensile strain [70]. Conversely, Figure 2.2(b) illustrates a film under

compressive stress, where the film tends to expand and thus contracts relative to the substrate [70]. By convention, tensile strain is assigned a positive sign, corresponding to concave curvature of the film/substrate system, while compressive strain is assigned a negative sign, corresponding to convex curvature.

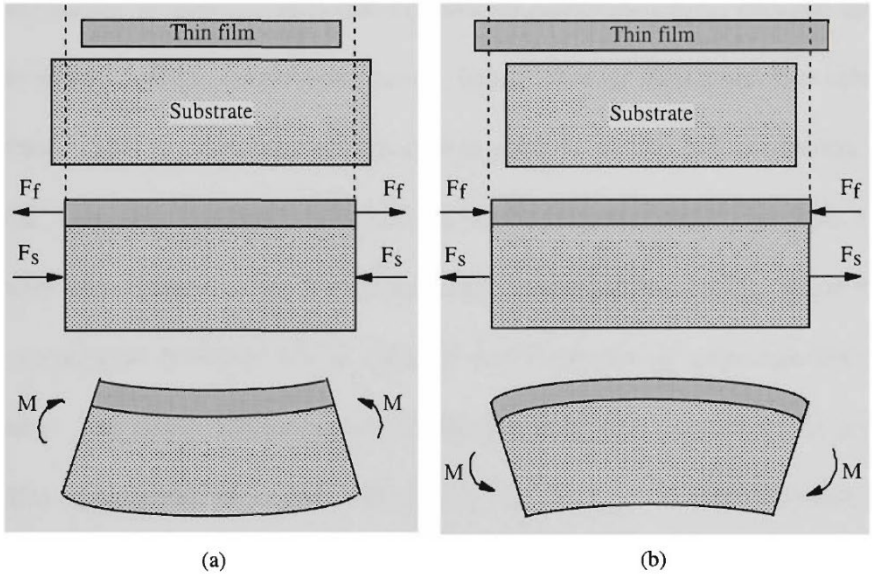

Figure 2.2: Residual (a) tensile, (b) compressive strain in a thin film. F_i are stress-induced forces and M is the induced bending moment. (Adapted from [70])

2.3 Molecular Beam Epitaxy (MBE)

Molecular beam epitaxy (MBE) is a thin-film deposition technique in which source materials are thermally evaporated in a controlled manner and directed onto a heated crystalline substrate under ultrahigh vacuum. Thin films crystallize through reactions between thermally energetic molecular or atomic beams of the constituent elements and the heated substrate surface [68,69,71]. The process occurs far from thermodynamic equilibrium and is governed mainly by the kinetics of the surface processes occurring when the impinging beams react with the outermost atomic layers of the substrate crystal [68].

It was originally developed for the growth of GaAs and (Al,Ga)As, but due to its unparalleled ability to control layering at the monolayer level and compatibility with surface-science techniques to monitor the growth process as it occurs, its use has expanded to other

semiconductors as well as metals and insulators [72]. A comparison of material properties between MBE and Non-MBE growths is shown in Table [73].

Table 2.1: Materials properties of different systems grown by MBE vs other methods. (Adapted from [73])

Material	Best value by MBE	Best value by non-MBE
ZnO	μ_e = 230,000 $cm^2/(V \cdot s)$ at 1 K	μ_e = 5,500 $cm^2/(V \cdot s)$ at 1 K
$SrTiO_3$	μ_e = 53,200 $cm^2/(V \cdot s)$ at 1 K	μ_e = 6,600 $cm^2/(V \cdot s)$ at 1 K
$SrRuO_3$	R_{300} K / R_{10} K = 115	R_{300} K / R_{10} K = 14
$SrVO_3$	R_{300} K / R_5 K = 222	R_{300} K / R_5 K = 2
EuO	Metal-insulator transition: $\Delta R/R=10^{11}$	Metal-insulator transition $\Delta R/R= 5*10^4$

2.4 Auburn FINO Lab MBE system

The Films, Interfaces, and Nanostructures of Oxides (FINO) lab operates an oxide MBE system specifically designed for the growth of complex oxide materials. It was designed by Mantis Deposition Ltd (unfortunately, the company is no longer in business). Figure 2.3 shows a schematic diagram of Auburn FINO lab MBE system [74].

2.4.1 Instruments

- Located at the base of the system, effusion cells are the primary source of elemental flux. Each cell contains a crucible that holds the source material, which is thermally evaporated to form a molecular beam. These sources are precisely temperature-controlled- typically using high-performance PID controllers with thermocouple feedback- achieving flux stability better than ±1% [68]. The crucible material is selected based on phase compatibility with the source to prevent melting or intermixing [73]. Shutters on each cell allow for precise temporal control of deposition.
- For refractory elements such as Ir, Ta, Nb, Ti, and Hf, which require temperatures around 2000 °C or more, metal-organic precursors are used instead. These precursors decompose at significantly lower temperatures (e.g., Ir at ~160 °C, Nb at ~75 °C), enabling efficient

incorporation into the film. The addition of a metal-organic gas delivery system classifies this setup as hybrid MBE [75–77]

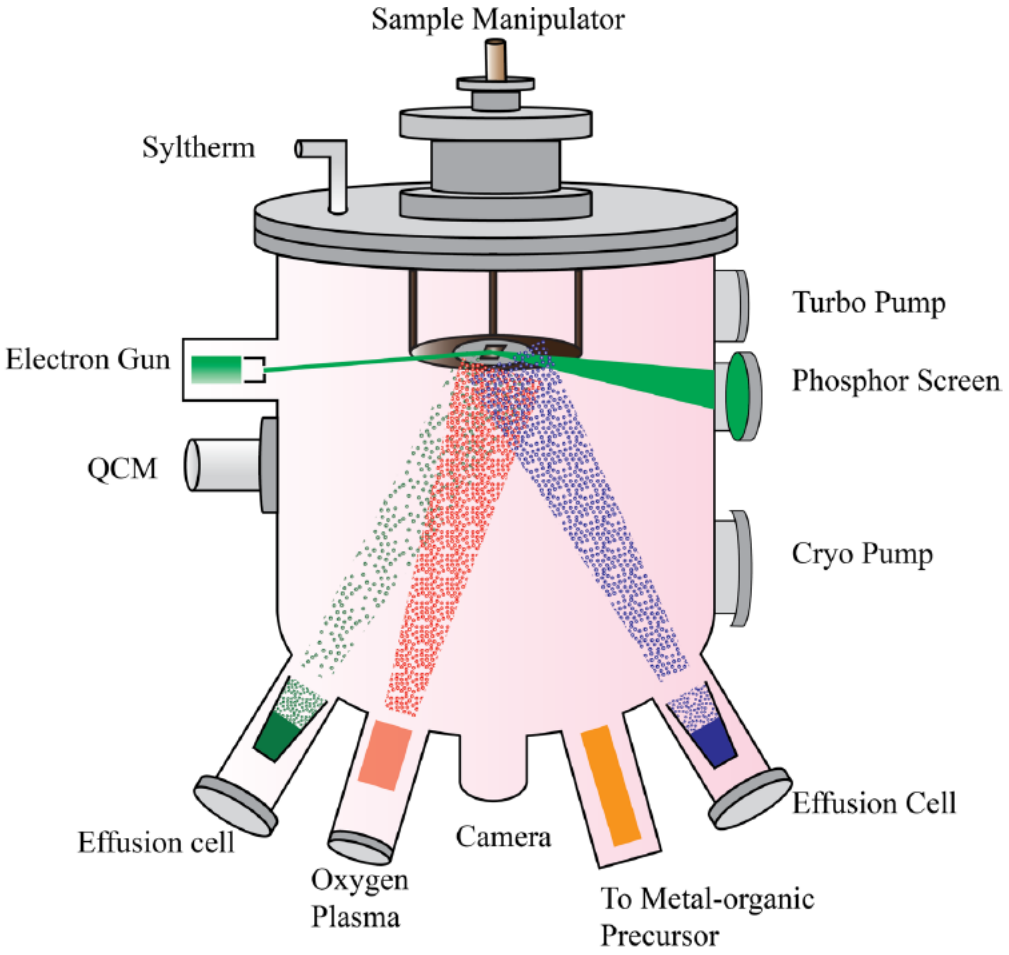

Figure 2.3: A schematic of the MBE system in Auburn FINO Lab. (Adapted from [74])

- A radio frequency (RF) plasma source operating at 300 Watts provides reactive oxygen species, essential for oxidizing complex oxides like cobaltites and for decomposing metal-organic precursors during growth.
- The Quartz Crystal Microbalance (QCM) is a highly sensitive instrument used in MBE systems to measure flux rates at specific temperatures. It operates on the piezoelectric effect of quartz, which oscillates at a resonant frequency when an alternating voltage is applied. As mass accumulates or is removed from the crystal surface, this frequency shifts. The shift in frequency is directly related to the amount of mass added or removed,

allowing flux monitoring [78,79]. This helps to determine if the temperature of a certain element needs to be modified.

- A 15 keV of electron beam generated by an electron gun probes the surface during growth. The diffracted electrons are detected on a phosphor screen. The corresponding technique, Reflection high-energy electron diffraction (RHEED**),** is an integral in-situ characterization tool that provides real-time feedback on surface structure and growth dynamics.
- A camera positioned at the bottom of the chamber is used to guide inserting and retracting the substrate holder into the stage. It also helps to track the RHEED beam as it is impinged on the film/substrate and make any necessary adjustments in the stage/beam position get the most useful RHEED data.
- The substrate manipulator holds and positions the substrate during growth. It has sophisticated heating systems that can ramp up temperature required to the desired phase of the film. The manipulator allows precise substrate positioning and rotation, essential for acquiring proper RHEED data.
- A closed-loop chiller circulates SYLTHERM XLT™ coolant to maintain the chamber shroud at low temperatures, minimizing background pressure and contamination [80].
- The core of the MBE system is its Ultra High Vacuum (UHV) chamber, which provides a long mean free path for molecular beams, essential for high-purity film growth [81]. The FINO lab system operates at a base pressure of ~10^{-9} Torr. A series of sophisticated pumping systems are used to achieve and maintain such a high level of vacuum. Following a venting, the chamber pumping begins with a scroll pump. Once the pressure drops below 50 mTorr, a turbomolecular pump is activated. When the pressure reaches 10^{-5} Torr, the ion pump is turned on. Additionally, a cryogenic pump is employed to further enhance vacuum quality. The MBE system is integrated with an X-ray photoelectron spectroscopy (XPS) system via a high-vacuum transfer line. The XPS chamber is maintained under vacuum using a titanium sublimation pump.

2.4.2 Growth steps:

1. Substrate selection: The first step for an MBE growth process involves selecting the appropriate substrate. For the works of this dissertation, the primary goal was to grow high quality films. Therefore, to minimize strain and defects, substrates were chosen to closely match the lattice parameters of the target film [82].
2. Substrate preparation: Substrates were cleaned via sonication in acetone and isopropanol. However, residues were found in some cases, so RHEED was used to assess surface quality and guide further treatment. The cleaned substrate was mounted in a substrate holder and loaded into the load-lock chamber for vacuum transfer.
3. Flux Calibration: To grow a thin film in the desired phase, there are two key factors: the right composition and the right growth conditions. For example, for growing $SrCoO_3$ film, the Sr and Co ratio must be 1:1. The QCM is used to determine the flux rate, hence the necessary temperature for the growth materials. A different technique called Rutherford backscattering spectroscopy (RBS), explained in Chapter 3, was used to correlate the flux rate to the actual film deposition. Typical Oxide MBE growth occurs at elemental vapor pressures (created by source vapors) on the order of~ 10^{-3} - 10^{-4} Torr [73]. Arrhenius plots help correlate temperature with vapor pressure. If the desired flux is not achieved, the source temperature is adjusted accordingly. For Sr and Co sources, the flux rate equation from the kinetic gas theory [2] provided reliable predictions for estimating the temperature change required to reach the target flux.
4. Determining growth conditions: Optimal growth conditions- such as substrate temperature and chamber pressure- are often established through iterative trial and error. The growth temperature is usually a balance the competing processes of adsorption and desorption of atoms on the substrate [73,83]. Ellingham diagrams, which illustrate the thermodynamic stability of compounds as a function of temperature and oxygen partial pressure, serve as valuable tools for selecting initial growth parameters and predicting phase stability during deposition, especially in new material phases [84,85].

2.5 Primary physical processes in an MBE growth

The essential elements of an MBE system are shown schematically in Figure 2.4. Following beam generation, the system undergoes two other functional zones, each associated with distinct physical processes [68,86,87]:

- Beam Interaction Zone: In the mixing zone in the MBE vacuum reactor, molecular beams from different sources intersect. However, the physical phenomena occurring in this region are not well understood. This is primarily because the mean free path of the molecules is typically much longer than the dimensions of the mixing zone, meaning that collisions or interactions between different molecular species are rare. As a result, the beams largely pass through each other without significant interaction before reaching the substrate.
- Crystallization Zone: This is the substrate region where epitaxial growth occurs. A series of surface processes are involved in the growth, as shown in the Figure, which includes: 1) adsorption of the constituent atoms or molecules impinging on the substrate surface, 2) surface migration and dissociation of the adsorbed molecules, 3) incorporation of the constituent atoms into the crystal lattice of the substrate or the epilayer already grown, 4) thermal desorption of the species not incorporated into the crystal lattice.

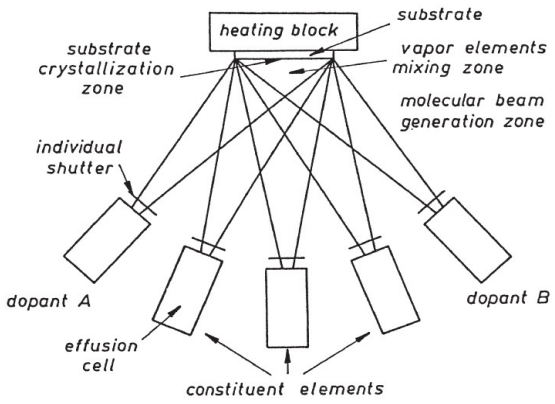

Figure 2.4: Schematic illustration of the essential parts of an MBE growth system. (Adapted from [68])

The substrate crystal surface is divided there into so-called crystal sites with which the impinging molecules or atoms may interact. Each crystal site is a small part of the crystal surface characterized by its individual chemical activity. A site may be created by a dangling bond, vacancy, step edge, etc. [68,88].

2.6 Instruments in the Auburn FINO Lab

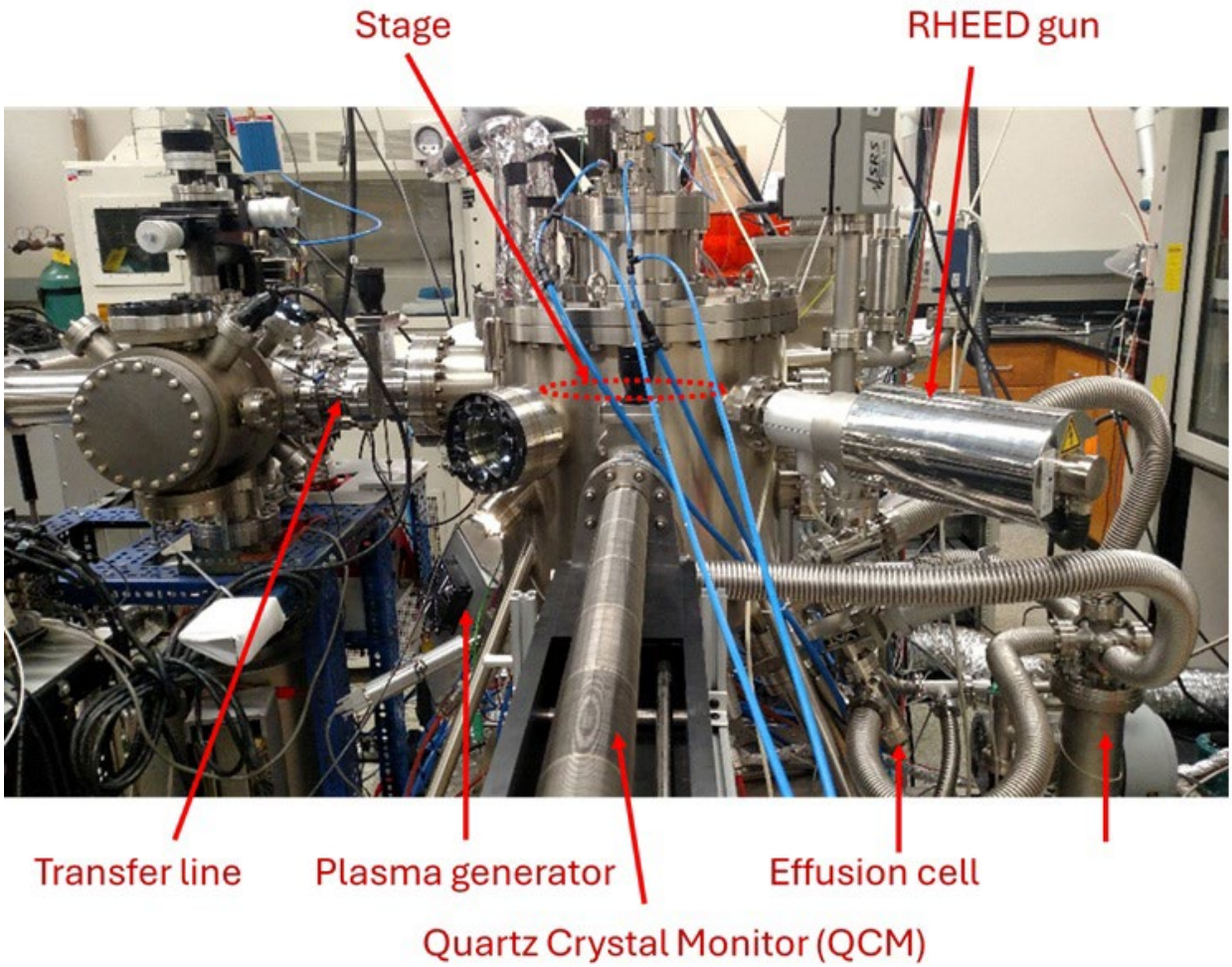

Figure 2.5: Auburn FINO Lab MBE system.

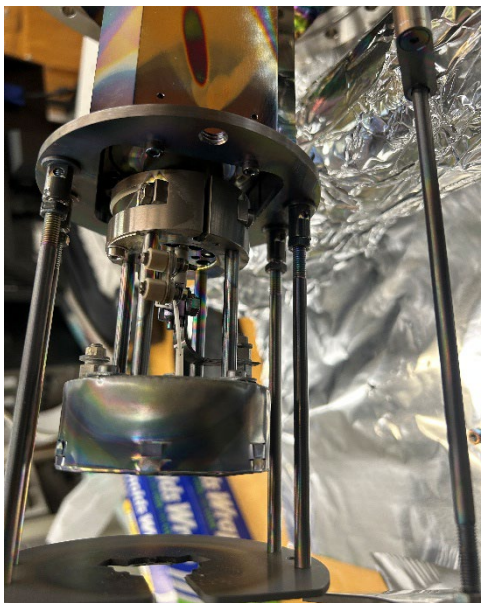

Figure 2.6: The manipular with the growth stage.

Figure 2.7: Sr effusion cell.

Figure 2.9: A top-view of the effusion cells once the manipular removed.

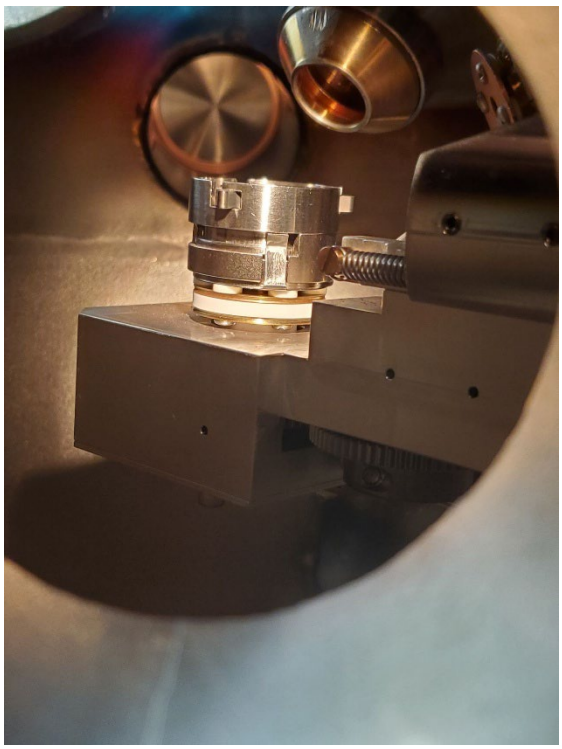

Figure 2.8: The XPS chamber and sample holder

Chapter 3 : Experimental Backgrounds

3.1 Introduction

This chapter presents a detailed overview on experimental backgrounds that include corresponding theory, basic working principle, overview on instruments and techniques on data acquisition. The molecular beam epitaxy (MBE) growth process starts with Rutherford backscattering spectroscopy (RBS) at Auburn University Physics department. Primary characterizations including in-situ Reflection High-Energy Electron Diffraction (RHEED) and in-vacuo X-ray Photoelectron Spectroscopy (XPS) are performed in the Auburn FINO Lab. Ex-situ structural analysis using X-ray Diffraction (XRD) is carried out in the Auburn University Chemistry Department. Xray absorption spectroscopy (XAS) studies were conducted at Brookhaven and Argonne National labs. Electrical transport properties measurements- performed in Auburn Electrical and Computer Engineering department- is briefly described along with discussions in Chapter 6.

3.2 Rutherford Backscattering Spectrometry (RBS)

Rutherford Backscattering Spectrometry (RBS) is an ion beam analysis technique based on elastic collisions between incident high-energy ions (He or H ions) and atomic nuclei within a target material [89–91]. When a collimated beam of intensity falls on a target in the form of a thin foil, the incident particles get scattered from the scattering centers and the target atoms get recoiled. The scattering process is governed by the repulsive Coulomb force between the positively charged incident ions (α-particles) and the target nuclei. This force follows an inverse square law, resulting in the scattered ions following hyperbolic trajectories.

RBS has the following characteristics [90]:

- Nondestructive and multi-elemental analysis technique for elements with depth concentration profiles

- Matrix independent (unaffected by chemical bonding states).
- High precision (typically ±3%).
- Increased sensitivity for heavier elements and best suited for analysis of heavier elements or layer on lighter substrates.
- Depth range ~ up to 2 μm for He and 20 μm for H ions.
- Depth resolution: 5–50 nm.
- Detection limit ~ 10^{18} cm^{-3}.
- Spatial definition: Beam spot size 0.5–2.0 mm.

The technique is named after Lord Ernest Rutherford, who first proposed the nuclear model of the atom. RBS as a method for materials analysis was first described in 1957 by Rubin et al. [92]. Today, RBS is commonly employed for three primary purposes: quantitative depth profiling, measurement of areal concentrations (in atoms/cm^3), and analysis of crystal quality and impurity lattice sites. Additionally, it is used to detect surface and subsurface contaminants and to investigate crystal structures [89]. An example of thickness study is illustrated in Figure 3.1. In our study, RBS was utilized exclusively for the compositional analysis of thin films.

3.2.1 Principle of RBS

In RBS, the high-energy ions can penetrate samples and undergo billiard ball-like interactions with the nucleus of the atoms in the material and result in backscattering. The ratio of the projectile energy after a collision to the projectile energy before a collision is defined as the kinematic factor. In other words, the energy fraction (E_1/E_0) transferred from primary to scattered particles, governed by the laws of conservation of energy and momentum, is given by the kinematic factor K. To derive the relation for the kinematic factor, it is assumed that the interaction is elastic, projectile energy E_0 is much larger than the binding energy of the atom in the target and the nuclear reactions and resonance must be absent. The Kinematic factor (K) is given by the following relation [89] assuming $M_2 > M_1$:

$$K=\left(\frac{\sqrt{1-\left(\left(\frac{M_1}{M_2}\right)\sin\theta\right)^2}+\left(\frac{M_1}{M_2}\right)\cos\theta}{1+\left(\frac{M_1}{M_2}\right)}\right)^2$$

Where M_1 is the mass of the incident α-particle ($^4He^{2+}$); M_2 is the mass of the target atom; and θ is defined as the angle between the trajectory of the α-particle before and after scattering. The interactions between projectile and target atoms are usually divided into two separate processes [90]. First, the energy is reduced by a discrete amount due to elastic collisions with sample atom nuclei (nuclear stopping power) and is characteristic of the atom struck (momentum transfer). On its way into the sample an individual ion loses energy in a continuous manner through a series of inelastic collisions with electrons (electronic stopping power), depending on the depth it travels. Therefore, a particle, which backscatters from an element at some depth in a sample, will have measurably less energy than a particle that backscatters from an element on the sample surface. Thus, the overall energy spectrum of the emerging back scattered ions reveals both the elemental composition and the depth distribution of those elements. To note, the amount of energy a projectile loses per distance traversed in a sample depends on the projectile, its velocity, the elements in the sample, and the density of the sample material. Typical energy losses for 2 MeV Helium range between 100 and 800 eV nm^{-1}.

In a typical RBS setup, the detector is positioned to collect ions scattered at angles close to 180° (backscattering geometry). The technique measures both the number and energy distribution of the backscattered ions from the near-surface region of the sample. The energy of the backscattered ions will depend on their incident energy and on the mass of the sample atom. The amount of energy transferred during the collision is determined by the mass ratio between the ion and the target atom. Therefore, by analyzing the energy spectrum of the scattered ions, one can deduce the chemical composition of the sample.

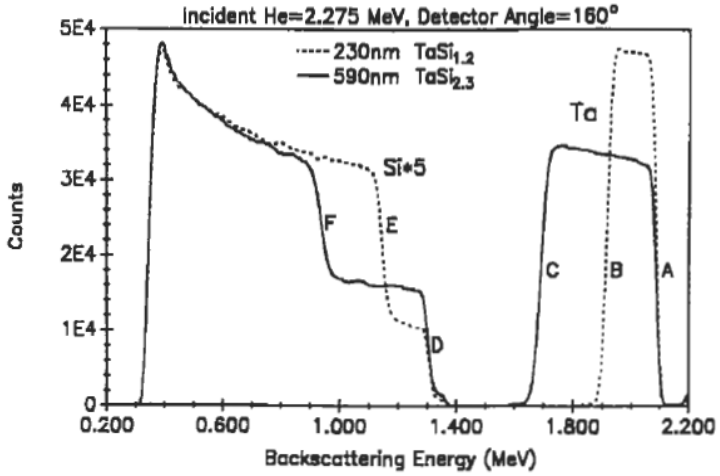

Figure 3.1: RBS spectra from two TaSix, films of different thicknesses on Si substrates. Particles scattered from Ta at the $TaSi_x$ - Si interface of the 230-nm film have a final energy of about 1.9 MeV (labeled B) after escaping from the sample, while for the 590-nm film, they have a final energy of about 1.7 MeV (labeled C). (Adapted from [89])

3.2.2 Rutherford scattering cross-section

After scattering, the incident particles can be deflected in any direction. The likelihood of an α-particle scattering from a target nucleus in a specific direction is described by the differential cross-section. The differential cross-section is equal to the fraction of the initial particle flux that is scattered into a given solid angle. The total Rutherford (scattering) cross-section can be derived by integrating over the total solid angle, it can be expressed as [90]:

$$\sigma_R(E,\theta) = \left(\frac{Z_1 Z_2 e^2}{8\pi\varepsilon_0 E}\right)^2 \cdot \frac{1}{\sin^4\theta} \cdot \frac{\left[M_2\cos\theta + \sqrt{M_2^2 - M_1^2\sin^2\theta}\right]^2}{M_2\sqrt{M_2^2 - M_1^2\sin^2\theta}}$$

Here, E is the energy of the incident atom immediately before scattering, and e is the electronic charge.The above equation indicates that scattering cross section in RBS is approximately proportional to the square of the atomic number (Z^2) of the target atom. As the mass of the target atom increases, the energy of the backscattered particle asymptotically approaches the incident particle energy. Consequently, RBS is significantly more sensitive to heavy elements than to light ones. In other words, RBS has good mass resolution for light elements, but poor mass resolution for heavy elements, as illustrated with K values for different atoms in Figure 3.3. This is because a significant amount of momentum is transferred from an incident particle to a light target atom.

3.2.3 RBS experiments for our samples:

A list of K-values for atoms in films in our research group:

M_1= 4 amu, Incident particle energy= 2 MeV, Scattering angle (θ) = 170°

Element	Atomic mass (M_2) in amu	Kinematic factor (K)	Backscattering Energy
O	16	0.3627	0.7254
Mg	24.31	0.5173	1.0346
Al	26.98	0.5527	1.1054
Co	58.93	0.7634	1.5268
Sr	87.62	0.8341	1.6682
Nb	92.91	0.8428	1.6856
La	138.91	0.892	1.784
Ta	180.95	0.916	1.832
Ir	192.22	0.9207	1.8414

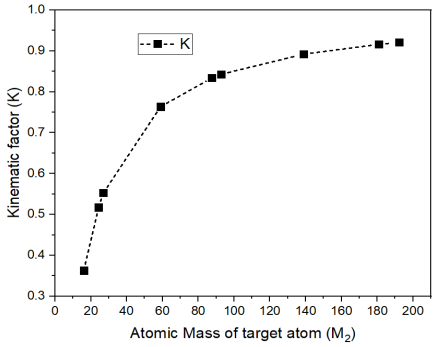

Figure 3.3: Kinematic factor as a function of atomic mass.

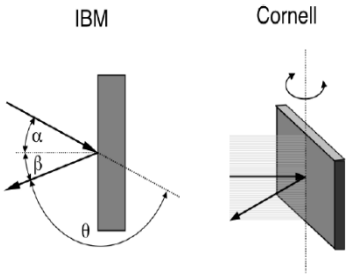

Figure 3.2: (left) In IBM geometry incident beam, exit beam and surface normal of the sample are in the same plane, (right) In Cornell geometry, incident beam, exit beam and the rotation axis of the sample are in the same plane. (Adapted from [90])

We performed our RBS measurements using Helium ion at 2 MeV of incident energy in the IBM geometry. The measurements were performed at Auburn University Dual Source Tandem Accelerator. We thank Tamara Isaacs-Smith for taking care of RBS measurements. The simulation was performed using SIMNRA 7.04. [93]. The target atom was characterized by Area density which provided a precise measurement of the number of atoms per cm^2.

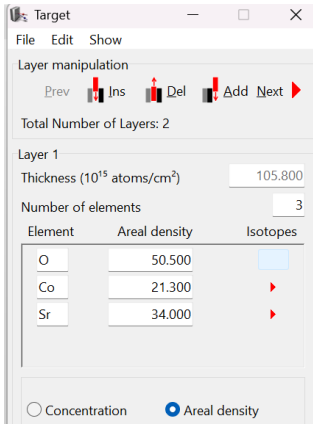

Figure 3.4: RBS analysis using SIMNRA software.

3.3 Reflection high-energy electron diffraction (RHEED)

Reflection High-Energy Electron Diffraction (RHEED) is an in-situ technique used during thin film growth to monitor surface quality and structure. It involves projecting electrons at a shallow angle on the growing film surface, making it highly surface-sensitive.

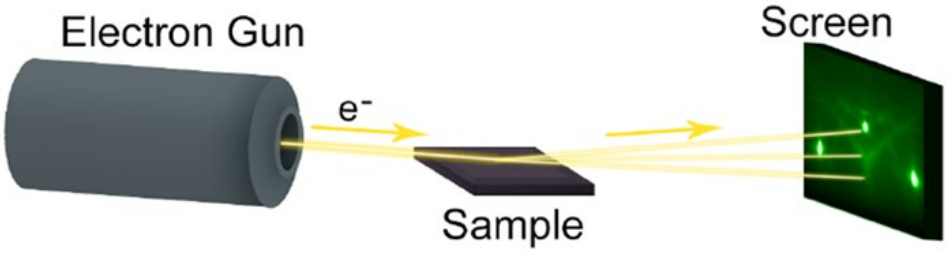

Figure 3.5: A simple RHEED set up. (Adapted from [97])

The first RHEED experiment was conducted by Nishikawa and Kikuchi in 1928 [94]. The technique is widely used to study surface ordering and structural characteristics during epitaxial growth, particularly in single crystal and epitaxial films under ultrahigh vacuum (UHV) conditions. It can provide a list of information including [95,96] : 1) In-situ crystalline quality, 2) Growth modes, 3) sizes of grains/domains of surface structures and microcrystals grown on the surface, 4) parameters characterizing structural phase transitions, 5) the periodicity (unit cells) in atomic arrangements, 6) surface roughness, 7) determining growth rate and stoichiometric conditions. To note, RHEED can be performed in two modes: reflection and transmission. The discussion here focuses only on the reflection mode, as it was the only mode used in the experiments.

3.3.1 RHEED instruments:

In RHEED, a high-energy electron beam (typically 8–20 keV) strikes a crystal surface at a grazing angle of 1-4°, making the technique extremely surface-sensitive [94]. The electrons scatter off the surface, and the diffracted beams (also in shallow angle) are captured on a detector, often a phosphor-coated, indium-tin-oxide (ITO) coated Pyrex screen to prevent charging. The basic RHEED setup includes an electron gun, sample holder, and screen as shown

in Figure 3.5 [97]. The electron beam is deflected magnetically or electrostatically to strike the sample, and the resulting diffraction pattern reveals surface structure. Commercial systems can focus the beam over distances of 40–70 cm. The angular divergence is maintained to be compatible with the sample flatness. In advanced RHEED systems, as shown in Figure 3.6 [94], one has the capability to measure RHEED intensity oscillations, to measure the lattice parameter, and step distributions. The sample can be rotated about the surface normal to change the incident electron azimuthal angle ϕ. This allows the full symmetry of a reconstruction to be determined.

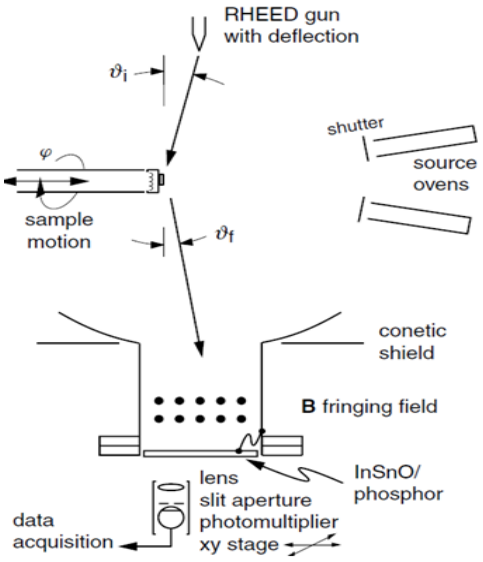

Figure 3.6: Diffractometer combined with molecular beam epitaxial growth. The glancing angle of incidence ϑi is varied by a combination of electrostatic deflection and sample motion. The diffracted beams are scanned across a phosphor screen by a small magnetic field. The diffracted intensity is measured with a photomultiplier. (Adapted from [94])

3.3.2 Principles of RHEED operation

The principle of diffraction was first developed using X-rays, and the underlying theory is identical for both electron and X-ray diffraction. Diffraction is typically explained using two main theoretical frameworks: the Laue approach and the Bragg approach [98]. Max von Laue viewed crystals as three-dimensional arrays of atoms acting like a 3D diffraction grating, emphasizing the vector nature of diffraction. His equations reflect the full three-dimensionality of crystal structures and diffracted beam directions. In contrast, the Braggs (Henry Bragg and his son Lawrence Bragg) envisaged crystals as parallel atomic planes that reflect X-rays, producing strong beams when the path difference between reflections equals an integer multiple of the wavelength. Bragg's law, a scalar equation, is simpler and more practical for numerical calculations, and it is a special case of Laue equations and is widely used for its simplicity.

Another Physicist, Paul Peter Ewald, provided the obvious way of interpreting the geometry of the diffraction patterns- by means of a construction which he called the reciprocal lattice and a sphere determined by the mode of incidence of the X-rays on the crystal (the Ewald sphere) [98]. Ewald's synthesis is a geometrical formulation or expression of Bragg's law which involves the reciprocal lattice and a 'sphere of reflection'.

3.3.3 RHEED Theory

Reciprocal Space: the significance

Diffraction experiments such as X-ray, electron, atom, and neutron diffraction are widely used to determine real-space lattice structures. It is helpful to go through briefly Reciprocal lattice that provides a simple geometrical basis for the theory.

Diffraction experiments rely on the wave-like behavior of particles, described by the de Broglie relation [99]:

$$\lambda = \frac{h}{p}$$

where λ is wavelength, h is Planck's constant (=6.63 × 10^{-34} J·s), and p is the magnitude of momentum. The propagation of a wave is described by the advancement of a wave front. Assuming a plane wave propagation, the wavevector kin is perpendicular to the plane wave front. The relationship between **p** and **k** is

$$\mathbf{p} = \frac{\mathrm{h}}{2\pi}\mathbf{k}$$

From the above two equations, one obtains

$$|\mathbf{k}| = \frac{2\pi}{\lambda}$$

The wavevector **K** has a unit of inverse length. It is therefore convenient to define a reciprocal space lattice in the momentum space that is related to the real space lattice [99].

Reciprocal Space: About

The atoms in a crystal can be mathematically represented as points in a three-dimensional real space lattice. If these lattice points are arranged in a periodic fashion, then one can define real space unit vectors a, b, and c and the angles α, β, and γ, as in Figure 3.7 [99].

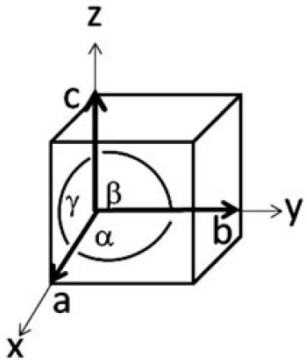

Figure 3.7: A unit cell with three-unit vectors. (Adapted from [99])

In lattices in which every site is indistinguishable from any other are called Bravais lattices. Thus, a Bravais lattice is one that consists of all points described by the position vector **R**, given as [94,99]:

$$\mathbf{R} = n_1\mathbf{a} + n_2\mathbf{b} + n_3\mathbf{c}$$

where n_1, n_2, and n_3 are integers, and a_1, a_2, and a_3 are linearly independent (non-coplanar) vectors called the primitive vectors of the lattice.

Reciprocal space, on the other hand, consists of reciprocal lattice points and reciprocal vectors defined by:

$$\mathbf{a}^* = \frac{2\pi(\mathbf{b} \times \mathbf{c})}{\mathbf{a} \cdot (\mathbf{b} \times \mathbf{c})}$$

$$\mathbf{b}^* = \frac{2\pi(\mathbf{c} \times \mathbf{a})}{\mathbf{a} \cdot (\mathbf{b} \times \mathbf{c})}$$

$$\mathbf{c}^* = \frac{2\pi(\mathbf{a} \times \mathbf{b})}{\mathbf{a} \cdot (\mathbf{b} \times \mathbf{c})}$$

The reciprocal lattice vector is defined by: $\mathbf{G} = h\mathbf{a}^* + k\mathbf{b}^* + l\mathbf{c}^*$

The two set of vectors are related to each other with the following relations [99]:

$$\mathbf{a}^* \cdot \mathbf{a} = \mathbf{b}^* \cdot \mathbf{b} = \mathbf{c}^* \cdot \mathbf{c} = 2\pi$$

Therefore, the symmetry of a real space and the corresponding reciprocal space are related. Figure 3.8 [98,100] provides a visual illustration of the relationship between the two spaces.

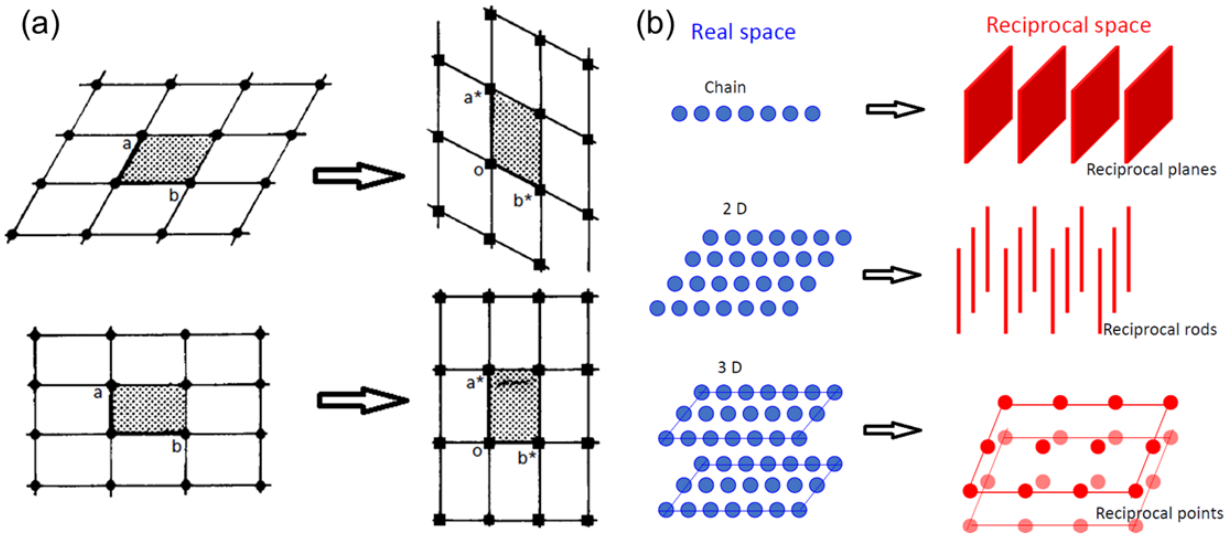

Figure 3.8: (a) The five plane lattices (left) and plane reciprocal lattices (right) indicating the corresponding unit cells, (b) reciprocal space in 1D, 2D and 3D. (Adapted from [98] and [100])

Bragg Condition

Bragg condition in real space defines conditions for diffraction which is given by the well-known formula [98,99]:

$2d_{hkl} \sin\theta = n\lambda$

Here, d_{hkl} is the spacing between atomic planes in the crystal, θ is the angle of incidence/reflection to the plane, λ is the wavelength of the incident wave, n the order of the reflection.

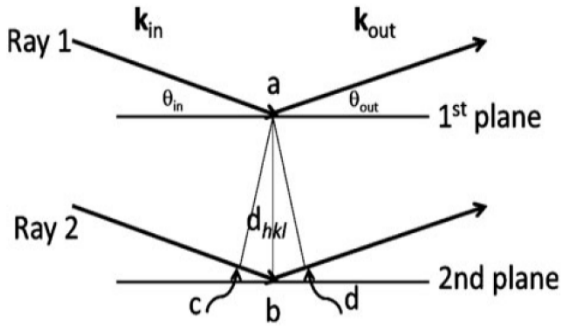

Figure 3.9: Bragg scattering from two parallel planes. Ray 2 travels $2d_{hkl} \sin\theta$ further than Ray 1. Bragg scattering from two parallel planes. (Adapted from [99]

Because diffraction is conveniently explained in reciprocal space, it's helpful to write Bragg condition in reciprocal space [99], which is:

$$\mathbf{K_{out}} - \mathbf{K_{in}} = \frac{2\pi n}{d_{hkl}}$$

To note, the other diffraction theory- the Laue conditions for maximum intensity are satisfied when the change in momentum ($\mathbf{K_{out}} - \mathbf{K_{in}}$) is equal to the reciprocal space vector (which is the Bragg condition) [99]:

$$\mathbf{K} = \mathbf{G}(\mathrm{hkl}) = \mathrm{h}\mathbf{a}^* + \mathrm{k}\mathbf{b}^* + \mathrm{l}\mathbf{c}^*$$

Ewald Sphere:

An Ewald sphere is a graphic construction in the reciprocal space that helps visualize diffraction planes that satisfy the Bragg (diffraction) conditions [95,100]. An Ewald sphere is shown in Figure 3.10 [94,99], which is constructed to ensure both elastic scattering and diffraction conditions (energy and momentum conservations) are fulfilled simultaneously [94]. The reciprocal lattice points that fall on the perimeter of the circle correspond to diffraction conditions.

In RHEED, tens of kiloelectron volt electrons have a short mean free path. Because of these electrons' glancing-angle incident geometry, the diffraction patterns obtained are from the near-surface region. This means the number of planes with a unit vector c in the direction perpendicular to the surface involved in diffraction is small, and the reciprocal lattice has a rod-

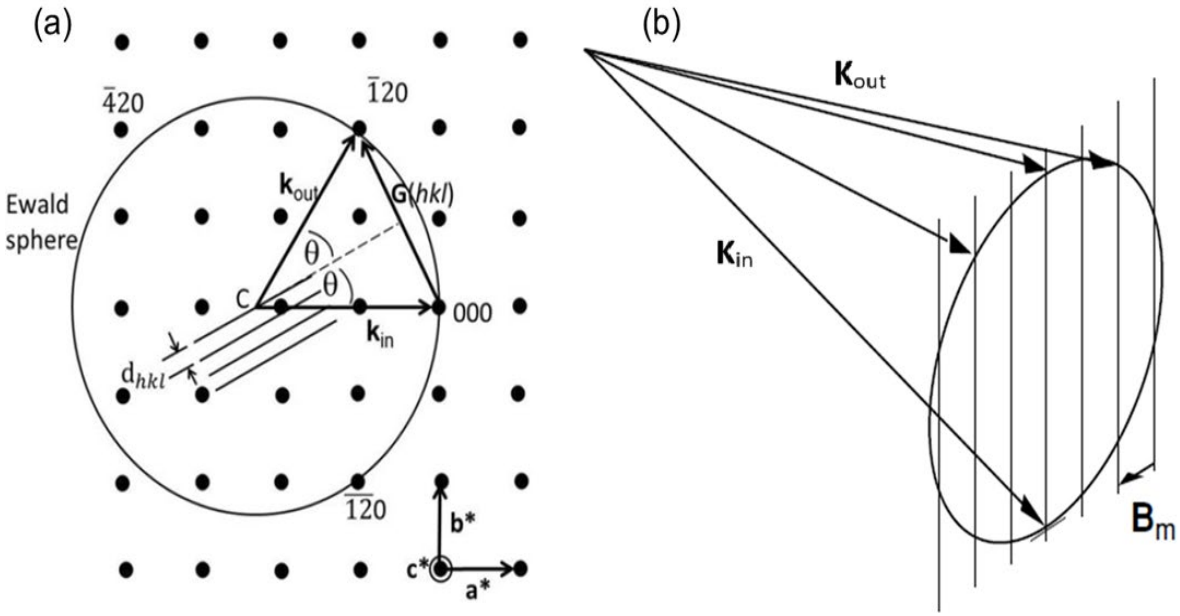

Figure 3.10: Example of Ewald construction (a) A two-dimensional reciprocal lattice and a slide of an Ewald sphere with radius |**K**in |, (b) The intersection of the rods (in reciprocal lattice) and the Ewald sphere conserves both energy and parallel momentum. The intersection of the Ewald sphere and the single plane of the rods, shown, is a circle. (Adapted from [94] and [99])

like structure perpendicular to the surface Figure 3.10(b) [99,100]. The diffraction spots in RHEED patterns from a two-dimensional (2D) lattice are thus always on the circles (Laue zones).

Kikuchi Lines:

Kikuchi lines are often observed in Reflection High-Energy Electron Diffraction (RHEED) which are produced by inelastically scattered electrons [94]. These patterns provide valuable information about the crystal structure and surface morphology. The intensity and sharpness of Kikuchi lines are highly sensitive to surface quality. Scattering from small terraces and atomic steps tends to broaden the lines, whereas sharp Kikuchi lines are typically observed in crystals with atomically flat surfaces and well-ordered bulk lattices. These lines appear more pronounced in heavier elements [94].

The formation of Kikuchi lines can be described by a two-step scattering model [94,101]: Incident high-energy electrons undergo inelastic collisions within the crystal, resulting in a diffuse, forward-scattered electron distribution. For single-plasmon scattering, this diffuse cone has an angular spread of approximately 0.1°, while multiple thermal diffuse scattering can broaden this to over 10°. If the energy loss in this first collision is small compared to the electron energy, the resulting electron distribution corresponds to an electron source of (almost) the initial energy, with isotropic emission within the crystal. The inelastically scattered electrons in this diffuse cone can subsequently be diffracted by the crystal lattice planes, depending on their angle. These two scattering processes combine to give rise to the appearance of Kikuchi lines at specific exit angles. The resulting pattern is essentially a diffraction image of an isotropic electron source with a narrow energy spread. The Kikuchi lines cannot arise from electrons that travel more than a few inelastic mean free paths. Since the outgoing electrons exit at a few degrees to the surface, this means that at most about 10 layers contribute to the pattern. This suggests that one might be able to use the intensity of the Kikuchi pattern to monitor the quality of a thin film. An example of Kikuchi lines in one of our films is shown in Figure 3.11.

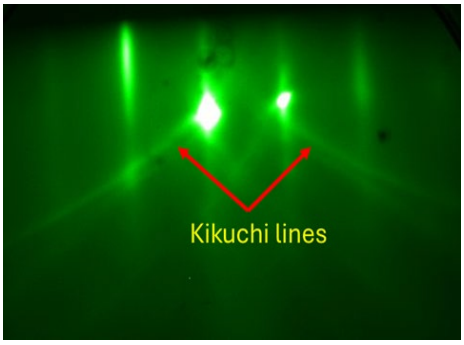

Figure 3.11: Kikuchi lines in a $SrIrO_3$ film.

As an example of application of RHEED, Figure 3.12 illustrates various surface structures and their corresponding RHEED patterns [95]:

Figure 3.12(a) shows that an atomically flat, single-crystalline surface produces sharp reciprocal rods with uniform intensity, assuming RHEED probes only the top layer. In reality, however, electron penetration into multiple layers causes intensity modulation due to interlayer interference, making some diffraction spots stronger than others. Figure 3.12(b) highlights RHEED for surface with small, out-of-phase domains. Domains smaller than the electron coherence length cause broadening the reciprocal rods due to finite-size effects. This results in elongated diffraction streaks, from which domain size can be estimated.

Figure 3.12(c) shows that for surfaces with two-level terraces of atomic height, reciprocal rods become complex. Off-Bragg conditions cause destructive interference, splitting the rods laterally. The spacing of these satellite streaks is proportional to terrace width, allowing estimation of average terrace size. As shown in Figure 3.12(d), in multilevel stepped surfaces, superposition of multiple two-level terrace patterns leads to modulated reciprocal rods which are sharp at on-Bragg points, broader at off-Bragg. This leads to produce streaks with perpendicular intensity variation.

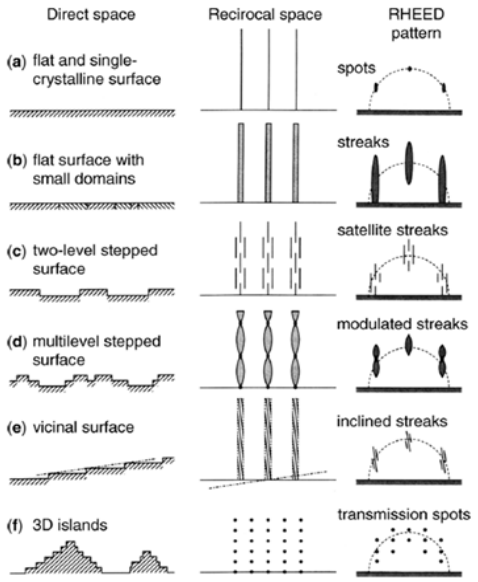

Figure 3.12**:** Schematics of various types of realistic surfaces: real-space morphologies, corresponding reciprocal space representations, and associated RHEED patterns. (Adapted from [95])

Figure 3.12(e) shows that, for surfaces with regular steps, if terrace widths are smaller than the electron coherence length, reciprocal rods become complex- broader at off-Bragg conditions, containing finer rods aligned with the overall surface. This results in inclined satellite streaks, with spacing inversely related to terrace width. Figure 3.12(f) shows RHEED pattern for 3D islands which we observed in our Co rich $SrCoO_3$ films. When the surface has 3D islands and the electron beam strikes at a low glancing angle, it transmits through the protruded parts of islands, producing a transmission (not reflection) diffraction pattern. If the islands are epitaxially grown, the resulting pattern corresponds to a 3D reciprocal lattice typical of bulk crystals.

3.4 X-ray diffraction (XRD)

X-ray diffraction (XRD) is a powerful and versatile technique widely used for obtaining a variety of structural information. It is one of the most essential tools for characterizing thin films. XRD can provide detailed insights into a number of aspects of thin film materials including: crystalline phase and lattice parameters, degree of crystallinity, residual stress/strain in the film, film thickness, periodicity, presence and nature of structural defects [102,103].

3.4.1 How X-rays are generated

Because this thesis work utilizes a variety of X-ray experiments, both laboratory-based and synchrotron-based facilities at national laboratories, it is worthwhile providing an overview of how X-rays are generated,

In lab-based systems, X-rays are typically generated using X-ray tubes or hot cathode tube, which operate based on the interaction between high-energy electrons and a metal target [104]**.** The hot filament that generates the electrons is negatively charged (the cathode) and the target is positively charged (the anode). When the electrons strike the target, X-rays are generated. At higher voltages, higher energy X-rays are generated. At higher currents, more X-rays are emitted by the anode, and the X-ray beam becomes brighter. When the incident electrons strike the anode in an X-ray tube, two processes are responsible for generating X-rays [104]:

Bremsstrahlung (White Radiation): Electrons are decelerated by electrostatic interactions with atoms in the metal target, emitting X-rays of varying energies. This produces a broad, continuous spectrum. The spectrum of white radiation depends on the voltage used to accelerate the electrons but is largely independent of the composition of the target.

Characteristic Radiation: the incident electrons knock electrons out of core orbitals in the atoms of the metal target**.** The resulting vacancies in the core orbitals are filled by outer-shell electrons giving rise to Sharp peaks of X-rays with specific energies. The energies of the characteristic X-rays are independent of the voltage but depend on the composition of the target. When an electron falls from a higher energy orbital into a vacancy generated in the 1s orbital (the K-shell), the emitted light is called K-radiation. L-radiation, resulting from transitions to the 2s or 2p orbitals, is generally not used for X-ray diffraction experiments, mostly because the yield of L-

radiation from a hot cathode tube is much smaller than the yield of K-radiation of the same wavelength. For certain X-ray experiments requiring a highly intense and focused beam, a synchrotron (a type of particle accelerator) is used to produce extremely intense X-ray beams, approximately 100 to 10,000 times stronger than $K\alpha_1$ radiation from standard X-ray tubes [98]. In a synchrotron, electrons travel near light speed in a circular path within a storage ring, by the action of magnets placed at intervals around the ring**.** The resulting synchrotron radiation, emitted tangentially due to continuous radial acceleration, spans wavelengths from infrared to hard X-rays. This radiation is then directed to a crystal monochromator, which selects the desired wavelength for the experiment.

We used lab-based instruments in generating X-rays for X-ray diffraction (XRD) and Xray Photoelectron Spectroscopy (XPS) measurements, and synchrotron-based facilities for Xray Absorption Spectroscopy (XAS) measurements.

3.4.2 Principles of XRD

The principle of diffraction has already been discussed in the RHEED chapter, this section therefore instead emphasizes the physics of scattering, responsible for the observed diffraction pattern.

The electrons in atoms contribute exclusively to the scattering of X-rays, and the scattering amplitude of an atom is determined by summing the contributions from all Z electrons, with the summation taking into account the path or phase differences between all the Z scattered waves. The result of this analysis is expressed by a simple number, f, the atomic scattering factor [98]:

$$\text{atomic scattering factor } f = \frac{\text{amplitude scattered by atom}}{\text{amplitude scattered by a single electron}}$$

The scattering amplitude of a unit cell is determined by summing the scattering amplitudes from all the atoms in the unit cell and expressed by, F_{hkl}, the structure factor

$$\text{structure factor } F_{hkl} = \frac{\text{amplitude scattered by the atoms in the unit cell}}{\text{amplitude scattered by a single electron}}$$

Summing the contributions from all unit cells in a crystal is complex due to attenuation of the incident X-ray beam as it scatters through the crystal. Additionally, reflected beams travel at the Bragg angle and are re-reflected in directions parallel to the incident beam, interfering destructively and further weakening the direct beam. This interplay is described by the dynamical theory of X-ray diffraction, which accounts for interactions among the incident, reflected, and re-reflected beams. However, when the crystal is sufficiently small, beam attenuation is minimal and diffracted intensities are weak compared to the direct beam. In such cases- common in XRD- the observed intensities can be approximated as proportional to the square of the structure factor.

3.4.3 Instruments for XRD experiment

X-ray diffraction (XRD) experiment involves rotating a small crystal in an X-ray beam. The resulting diffracted beams (reflections) emerge in various directions, revealing the size and shape of the unit cell (from angles) and atomic positions (from intensities). The apparatus commonly used in X-ray diffraction experiments is called a diffractometer consisting of five major components [102,104]: The X-ray source, the detector, the incident (or primary beam) optics, the receiving (or diffracted beam) optics, and the goniometer (which turns the crystal in the X-ray beam), as shown in Figure 3.13 [102].

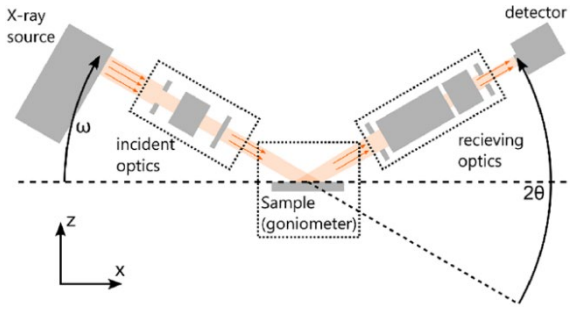

Figure 3.13: Components of a diffractometer. (Adapted from [102])

The goniometer consists of a goniometer head, to which the crystal is attached or mounted, and a series of gears that rotate the head and the crystal precisely. The goniometer head is designed to control the angles between the source, detector, and sample surface. The most commonly used setups involve the angle between the X-ray source and the sample surface (ω), and the angle between the incident beam and the detector (2θ). To analyze in-plane texture using pole figures, additional degrees of freedom are needed: the tilt angle (χ) and the azimuthal or rotation angle (φ). The tilt angle χ is often related to another angle ψ by the relation: $\chi = 90° - \psi$, as illustrated in Figure 3.14 [102]**.** The X-ray detector converts X-ray photons into electrical signals that can be used to determine the reflection intensities and scattering angles. Detectors are often defined by their dimensionality, and can be point detectors (0D), line detectors (1D), or area detectors (2D).

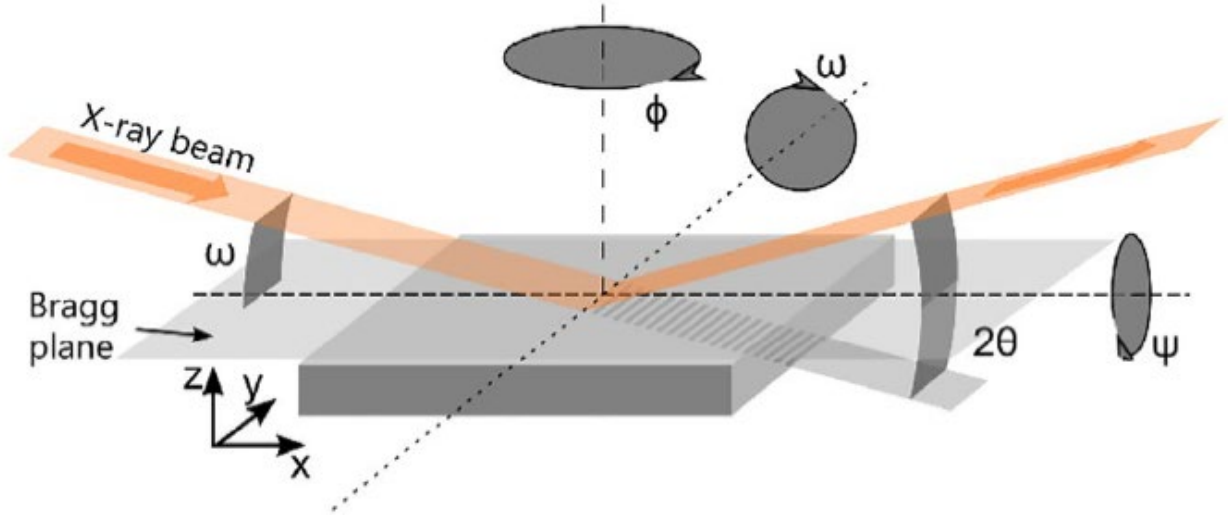

Figure 3.14: Schematic of the notation used for the angles and degrees of freedom in a typical diffractometer used for thin film measurements. (Adapted from [102])

There are two primary optical modes that diffractometers can be configured in: Bragg- Brentano (BB) optics and Parallel Beam optics (PB) [102]. Bragg-Brentano optics are widely employed in powder X-ray diffractometry due to their ability to generate high-intensity diffraction signals from a divergent X-ray beam [102]**.** In this configuration, the X-ray source and receiving slit move along a diffractometer circle centered on the sample surface. Divergent X-rays strike the sample at various points and are focused onto the receiving slit, forming a focusing circle whose radius depends on the Bragg angle (θ). This geometry, however, introduces several sources of error, therefore, Parallel Beam optics is usually used for thin films analysis.

Divergent X-rays from the source can be conditioned into a parallel beam using narrow slits with parallel plate collimators (rotated Soller slits) or multilayer mirrors (e.g., parabolic or Göbel mirrors), achieving beam divergence as low as a few 0.01°. This ensures a uniform incident angle across the sample and minimizes systematic errors inherent in Bragg- Brentano geometry. The X-ray diffraction experiments of this dissertation were performed in PB mode.

3.4.4 XRD measurement modes

X-ray diffraction has numerous applications in various modes, and only those relevant to this dissertation are discussed here. In essence, when an X-ray beam strikes a film, it diffracts through the crystal planes and reflects in multiple directions. Constructive interference (thus a detectable diffraction pattern) occurs only in directions that satisfy the Bragg condition.

Coupled 2θ/ω scan:

A coupled scan is used to measure the Bragg diffraction angle. The basic set-up is shown in Figure 3.15 [103], where the incident angle (ω) is defined between the X-ray source and the sample, and the diffracted angle (2θ) is defined between the incident beam and detector angle. This scan provides is a plot of scattered X-ray intensity vs 2θ, but ω is always coupled with 2θ such that: ω = ½ (2θ) (+ any offset). The Bragg peak position, therefore, a coupled scan can provide information on lattice mismatch, relaxation, and can help identify different phases present in the material. The width of the film's Bragg peak and the thickness fringes can be used to quantify the film thickness.

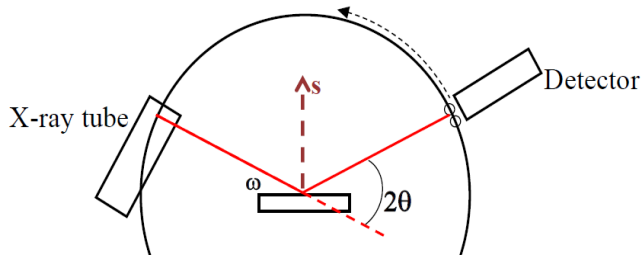

Figure 3.15: Basic setup for a coupled scan. (Adapted from [103])

In a 2θ/ω scan, peaks from the substrate will often dominate the pattern whereas peaks from the film may be very low in intensity due to the much lower film thickness. Therefore, it is common to plot patterns from thin films on a logarithmic intensity scale [102].

X-ray reflectivity:

X-ray reflectivity (XRR) involves scanning the film at very small angles. The simplified geometry, often called the kinematical condition, of a standard XRR measurement is shown in Figure 3.16 [105]. Only total external reflection occurs for X-rays at small angles of incidence below a critical angle, which is why we observe a relatively horizontal line below this angle.

Refraction starts to occur above the critical angle, but because n_1 for X-ray is smaller than 1 unlike visible light, the angle θ_r is smaller than the angle θ) according to Snell's law:

$$n_1 \cos \theta_r = n_0 \cos \theta$$

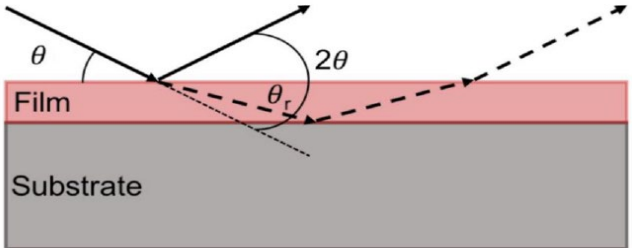

Figure 3.16: Geometry of a standard XRR measurement. Solid rays are incident and reflected X-rays at the surface, and dashed rays are refracted X-rays in the thin film. (Adapted from [105])

The refracted X-rays travel through the thin film to film-substrate interface and are reflected back to the surface. They produce constructive and destructive interference oscillations called Kiessig fringes, whose width is inversely proportional to the film thickness.

For analysis, generally, an X-ray experimental reflectivity curve is compared to the theoretical curve calculated based on a layer structure model [106]. The solution with optimal parameter values of thickness, density, and roughness of the interface in the multilayer film is obtained when the residual between the measured and calculated reflectivity data reaches a minimum.

Rocking curve:

In a rocking curve measurement, the detector is fixed at a certain 2θ angle, and the sample is tilted (or 'rocked') in the axis such that planes no longer parallel with the sample surface are brought onto the Bragg plane [102,107] . This result is a single bell curve, known as a rocking curve, which gives the distribution of planes as a function of tilt. The width of the rocking curve depends upon the mosaic spread of the grains, density of dislocations, and substrate curvature, which disrupt the parallel nature of the lattice planes. Therefore, the full-width half-maximum (FWHM) of the rocking curve is often recorded and is generally used as an indication of the quality of intended epitaxial growth, or indication of preferential orientation.

Reciprocal space mapping:

The reciprocal lattice point spreads caused by changes in crystal structure or degradation in crystallinity can be attributable to changes or spread in the crystal orientation or the lattice constants. The reciprocal space mapping measurement records diffraction intensity distributions by scanning a series of 2θ scans at different ω settings [108].

The distributions of the directions and intensities of reciprocal points perpendicular to the sample surface are observed using the in-plane measurement method instead of using the out of- plane measurement. To analyze the data, it is very useful to express the positions and shapes of reciprocal lattice points using the Cartesian coordinates system (i.e., q_x, q_y) instead of 2θ and ω for calculating the d-spacings [107], where both qx and qz are the inverse of lattice spacing.

$$q_x = \frac{2}{\lambda} sin\left(\frac{2\theta}{2}\right) sin\left(\frac{2\theta}{2} - \omega\right) = \frac{1}{\lambda}\{cos\,\omega - cos(2\theta - \omega)\}$$

$$q_z = \frac{2}{\lambda} sin\left(\frac{2\theta}{2}\right) cos\left(\frac{2\theta}{2} - \omega\right) = \frac{1}{\lambda}\{sin\,\omega - sin(2\theta - \omega)\}$$

The relative positions of the reciprocal lattice points of an epitaxial film and its substrate change, depending on lattice matching and the presence or absence of lattice relaxation. This is illustrated in Figure 3.17 [107].

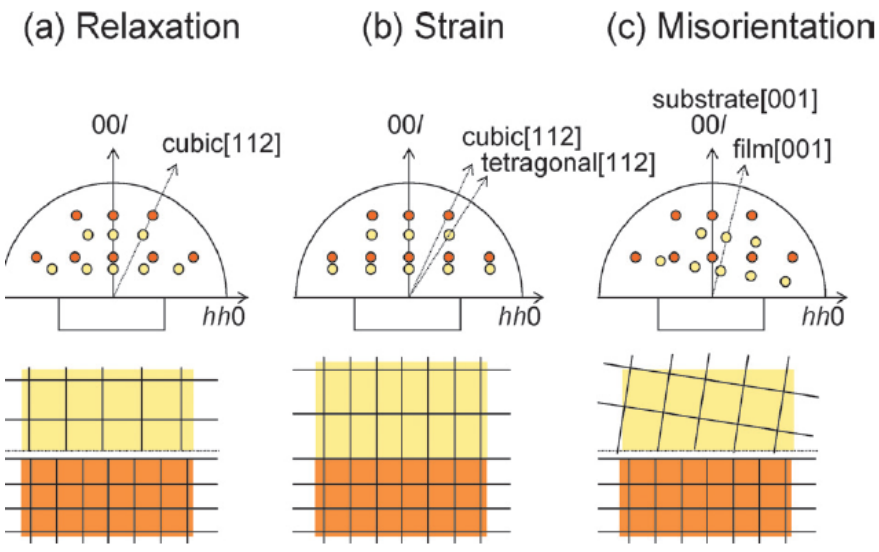

Figure 3.17: Reciprocal space maps of hetero-epitaxial layer. (Adapted from [107])

3.4.5 Crystal structure determination and phase identification

A given substance always produces a characteristic diffraction pattern, whether that substance is present in the pure state or as one constituent of a mixture of substances. The determination of an unknown structure proceeds in three major steps [109]:

1. The shape and size of the unit cell are deduced from the angular positions of the diffraction lines. A comprehensive database of diffraction patterns enables the identification of unknown substances by comparing their recorded patterns with those of known materials. For powder specimens in which the crystals are randomly orientated, the set of d spacings and their relative intensities serves as a 'fingerprint' (or 'genetic strand') from which the phase can be identified by comparison with the 'fingerprints' of phases in the X-ray Powder Diffraction File.

2. The number of atoms per unit cell is then computed from the shape and size of the unit cell, the chemical composition of the specimen, and its measured density.

3. Finally, the positions of the atoms within the unit cell are deduced from the relative intensities of the diffraction lines.

3.4.6 X-ray diffraction from single crystal thin films and multilayers

As the angle θ is varied, reflections occur whenever Bragg's law is satisfied. For a single crystal, with only one set of planes parallel to the surface, there will only be one Bragg reflection. For multilayer specimens, which may consist of a sequence of thin crystal films (like superlattice) mounted on a single crystal substrate, there will be three Bragg reflections- one from the substrate and one each from the thin films (of different crystal structure).

However, there are more diffraction phenomena to be recorded. First, since the layers are generally thin- of the order 10 nm- Bragg peaks are substantially broadened, and this may be used to estimate the thickness of the layers by means of the Scherrer equation [98].

Second, the repeat distance, or superlattice wavelength Λ of the layers can be determined from the angles of 'satellite' reflections which occur (given a multilayer specimen with a long-range structural coherence) on either side of the (high angle) Bragg peaks. The value of may be determined from the equation [98]:

$$\Lambda = \frac{\lambda}{2(\sin\theta_2 - \sin\theta_1)}$$

where λ = the X-ray wavelength and $\sin\theta_1$, $\sin\theta_2$ are the Bragg angles of adjacent satellite peaks. The repeat distance Λ of the layers also gives rise to low-angle Bragg reflections (of the order $2\theta = 2 - 5^o$), between which a further set of satellite peaks or fringes called Keissig fringes which may be used to determine the total multilayer film thickness $N\Lambda$ using the relation [98]:

$$\frac{1}{N\Lambda} = \frac{1}{d_{k2}} - \frac{1}{d_{k1}}$$

where d_{k1}, d_{k2} are the notional d-spacings of any pair of adjacent Keissig fringes. Meanwhile, the phenomenon of long-range order is called superlattice formation and can give rise to superimposed reflections in the diffraction pattern- observed in our superlattice films.

3.4.7 Diffraction in real films

In the theory of diffraction, it was treated geometrically, with incident and reflected beams represented as perfectly narrow and parallel, reflecting only at precise Bragg angles. However, real X-ray beams have finite width, and they are not perfectly parallel to an extent, depending on the experimental setup. These instrumental factors cause broadening of the reflected beams: the reflections peak at the Bragg angles and decrease to zero on either side. Broadening is not solely due to such instrumental factors but much more importantly also arises from the specimen itself [98]. Measurable diffraction can occur at angles slightly off from the exact Bragg angle due to crystal imperfections which can disrupt the conditions for perfect destructive interference, allowing weak scattering at nearby angles. Moreover, crystalline size can contribute to this. If the path difference between scattered X-rays is only slightly off from an integer multiple of the wavelength, full cancellation requires many atomic planes. In very small crystals, these planes may not exist, preventing complete destructive interference. This results in peak broadening-diffraction at angles close to, but not exactly at, the Bragg angle. On other hand, Real crystals deviate from the ideal of infinite, perfectly periodic lattices. Dislocations and sub-grains introduce local misalignments. Many crystals exhibit a mosaic structure, composed of small, slightly misoriented blocks, which also contribute to diffraction broadening [109].

3.5 X-ray photoelectron spectroscopy (XPS)

X-ray Photoelectron Spectroscopy (XPS) was primarily employed to determine elemental composition and chemical states, particularly the oxidation states of transition metals. It was also used for element identification, to estimate film thickness and to compare surface versus bulk chemical characteristics.

3.5.1 XPS principles

The XPS technique is based on the theory of photoelectric effect. The main components of an x-ray source in an XPS system are: a filament, a target material and a power supply [110]. The energy of the emitted photon depends on the target material employed in the process (Al Kα : 1486.8 eV, Mg Kα: 1253.6 eV)**.** Monochromators are used to isolate a specific X-ray emission line (like) from the X-ray source.

XPS employs X-rays of a certain energy to photoexcite core electrons, which are then emitted from their parent atoms with a kinetic energy characteristic of their initial atomic energy level and element **(**Figure 3.18). The kinetic energy, E_k, of the emitted photoelectrons is given by [111]:

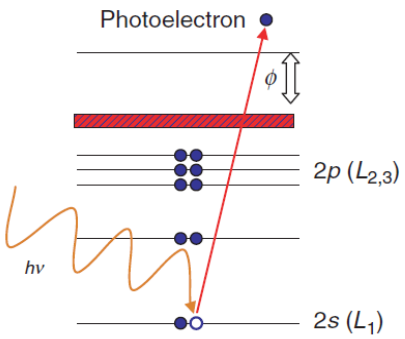

Figure 3.18: The process of X-ray core-level photoemission. (Adapted from [111])

$$E_k = h\nu - E_B + \varphi$$

Where hν represents the incident photon energy, E_B is the binding energy of the atomic energy level and φ is the combined workfunction of the sample and the electron analyzer.

Photoelectrons are readily absorbed or scattered by air, so the photoemission process is almost always performed under ultra-high vacuum using the experimental arrangement shown in Figure 3.19 [112]. To analyze the energy of emitted electrons, energy-selective electron analyzers are used which employ tunable magnetic fields, typically in a concentric hemispherical analyzer (CHA) configuration. In this configuration, a voltage is applied across an inner and an outer hemisphere, and electrons entering the analyzer are guided through the gap between the

hemispheres. Electrons travelling too quickly collide with the outer hemisphere, while those travelling too slowly are attracted to the inner hemisphere. This was only electrons in a narrow energy region succeed in travelling around the hemispherical arc to the detector, ensuring for precise energy resolution. A series of electron lenses are placed before the CHA, which can be used to retard the incoming electrons to a fixed 'pass energy' [111].

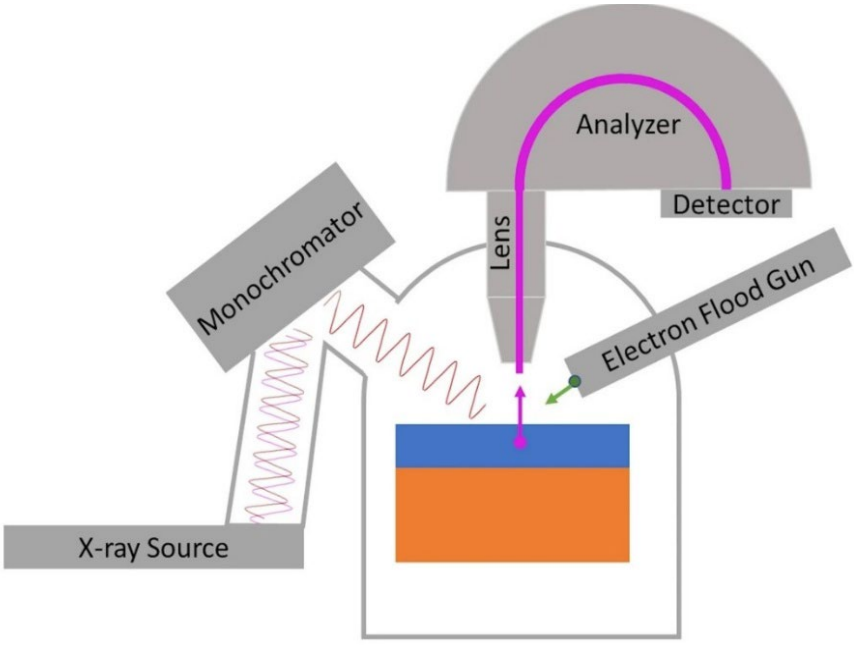

Figure 3.19: Schematic of an XPS chamber configuration. (Adapted from [112])

3.5.2 Measurements and quantifications

XPS measurements can be classified into two categories: Survey and Multiplex scans. A rapid compositional analysis of a sample can be performed within minutes by acquiring a survey scan over the widest energy range accessible with the X-ray source, as shown in Figure 3.20. Each element has a unique set of well-defined energy levels, which allows their identification through matching the photoelectron binding energies in the survey spectra to those of tabulated atomic energy levels. All elements except hydrogen and helium can be analyzed using X-ray photoelectron spectroscopy (XPS) [111].

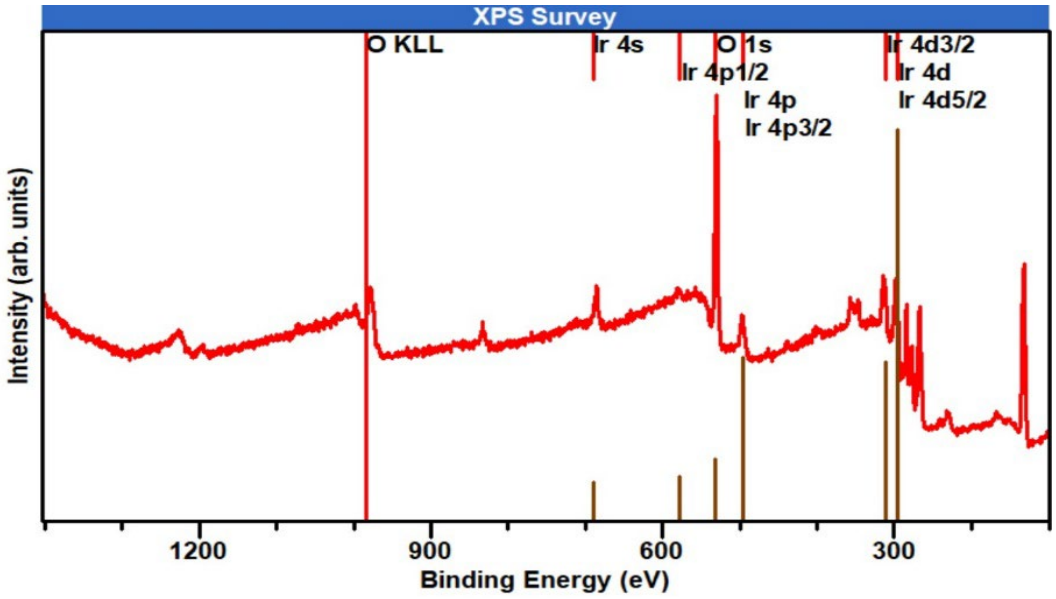

Figure 3.20: An example of a survey scan (only Ir and O elements are labeled).

Multiplex scans are High-resolution spectra that take several hours to complete. They reveal information about the chemical nature of the element, and fine structure arising from the spin-orbit coupling (SOC). For example, the Co 2p peak in the XPS data of $SrCoO_3$ appears as two separate peaks (Co $2p_{1/2}$ and Co $2p_{3/2}$), as shown in Figure 3.21.

More complex spectra are often observed for elements in which excitation of electrons to the valence conduction band occurs in parallel to the photoemission process. Ligand-metal charge-transfer effects change the electron configuration of the final excited state, giving rise to satellites that are at high binding energy relative to the main photoemission peak [111], as observed in Co 2p XPS data.

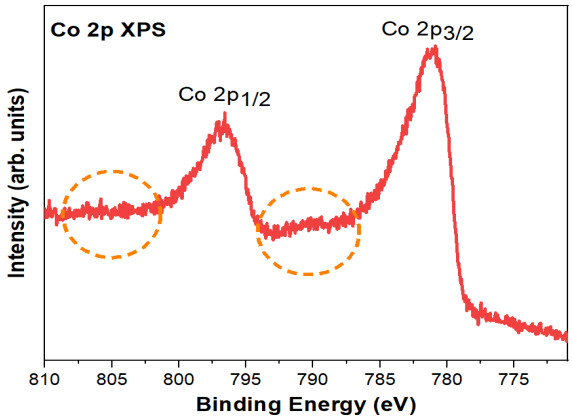

Figure 3.21: Co 2p multiplex with two peaks due to spin-orbit coupling (dashed orange circles represent corresponding satellite peaks).

3.5.3 Film thickness determination using XPS

For measuring the initial films which were 5 nm or below in thickness, XPS was used effectively. For ultra-thin films of around 2 nm, the Beer- Lambert Law provided a good estimation of film thickness that required only two measurements at a certain angle [110,113]:

$$I_d = I_0 \exp\left(\frac{-d}{\lambda \cos \theta}\right)$$

Where, I_0 is the intensity of a certain element in the substrate, I_d is the intensity of the same element from all depths greater than d, θ is the angle between the analyzer and the surface normal, λ is the photoelectron attenuation length. The angle was kept fixed (45^o), the attenuation length was calculated from the NIST Standard Reference Database-82 [114]. An open-source, online tool was used later in thickness calculation for relatively thicker films [115,116]. Note that, these approaches work only for two-layer materials.

3.5.4 Auburn FINO Lab XPS System

XPS measurements at Auburn FINO lab facility were performed using a PHI 5400 system equipped with a monochromatic Al Kα source with photon energy: 14.5 keV. The system supports angle-resolved XPS (ARXPS) with measurement capabilities ranging from 20° to 45°, enabling depth-sensitive analysis of surface and near-surface regions.

Insulating oxide materials often experience surface charging following photoelectron emission, leading to peak shifts and line distortion in XPS spectra [111]. To mitigate these effects, a low energy electron flood gun is employed to neutralize the accumulated positive charge on the sample surface. In XPS measurements, survey scans are typically acquired at a resolution of 0.5 eV/step with a pass energy of 180 eV, while high-resolution (multiplex) scans are performed at 0.05 eV/step with a pass energy of 35 eV. All spectra are calibrated using the O 1s core level peak, referenced at 530.0 eV, to correct for any chemical shifts.

3.5.5 Hard X-ray photoelectron spectroscopy (HAXPES)

Performing XPS studies with X-ray photon energies above 2 keV provides more bulk sensitivity and enables access to transition metal 1s core levels that are inaccessible using conventional laboratory sources. HAXPES measurements thus enable studies of deeply buried interfaces more than 5 nm below the film surface that would be impossible with a lab source [112]. This makes HAXPES an important tool for studying complex oxide interfaces and heterostructures.

For example, at kinetic energies around 10 keV, the inelastic mean free path of photoelectrons increases substantially. As a result, only 50% of the detected signal originates from the top ~6.5 nm of the sample, and just 10% comes from the top 1.0 nm. In contrast, with a typical lab source, 50% of the signal is generated to the top ~1.0 nm, and only ~3% originates from 5 nm below the surface [112]. This difference clearly shows the unique capability of HAXPES to probe deeper into materials.

The HAXPES measurements of the superlattice samples for this research study were performed in a Laboratory-based HAXPES system at Temple University using a high-flux, high-resolution, monochromated 5.4 keV microfocus X-ray source.

3.6 X-ray absorption near-edge structure (XANES)

X-ray absorption near-edge structure (XANES) spectroscopy is a well-established technique providing information on the electronic, structural and magnetic properties of matter. The technique is usually performed using synchrotron radiation [117].

If an assembly of atoms is exposed to X-rays, it will absorb some of the incoming photons. At a certain energy a sharp rise in the absorption will be observed which is called the absorption edge. The energy of the absorption edge is determined by the binding energy of a core level. The energy of an absorption edge therefore corresponds to the core-level energy, which is characteristic for each element, making XANES an element-selective technique. As such XANES is able to provide a detailed picture of the local electronic structure of the element studied [117].

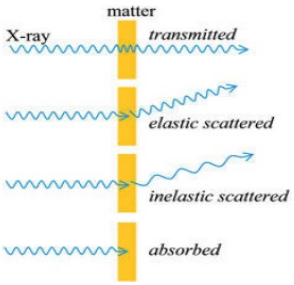

Figure 3.22: X-ray interactions with matter. (Adapted from [55])

3.6.1 X-ray absorption

X-rays interact with matter in several ways: they can be transmitted (passing through unchanged in energy and direction, but not phase), elastically scattered (changing direction but not energy), inelastically scattered (changing both direction and energy), or absorbed [55]. This

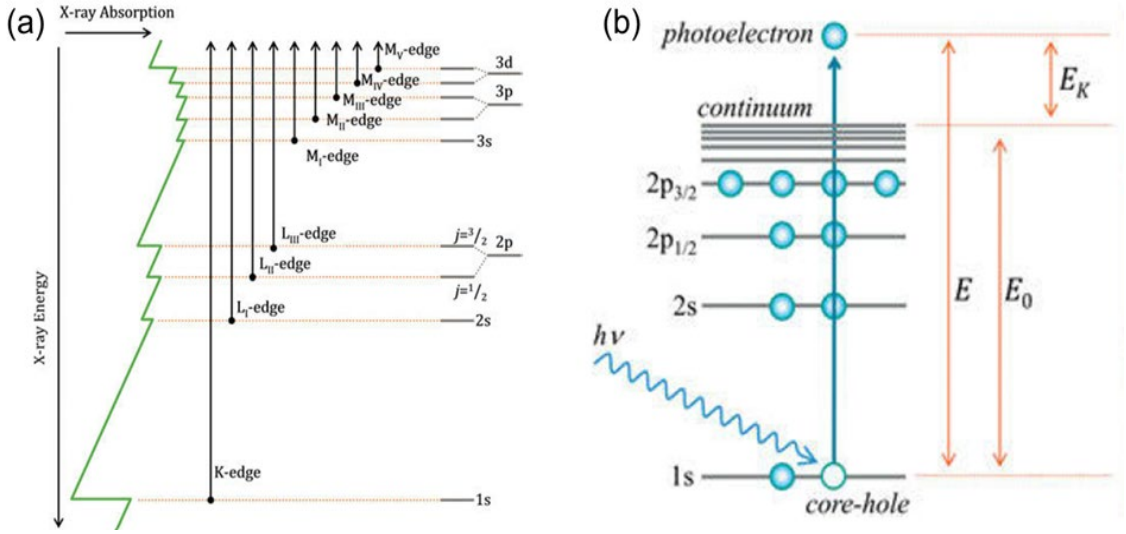

Figure 3.23: (a) Schematic diagram of the different X-ray excitations giving rise to K, L and, (b) A schematic of the photoexcitation process, indicating the threshold energy E_0, kinetic energy of the photoelectron, E_K, and the energy of the incident X-ray photon E. (Adapted from [55])

section focuses on the absorption process, which is described by X-ray absorption coefficient μ(E). This phenomenon depends strongly upon the X-ray energy, and the nature of the matter. X-ray absorption by the electrons belonging to different core levels gives rise to different X-ray absorption edges. This is summarized in Figure 3.23(a) [55], with a schematic diagram of the different core-electron excitations giving rise to K, L and M X-ray absorption edges. Figure 3.23(b) [55] shows a schematic of a K-edge 1s core excitation.

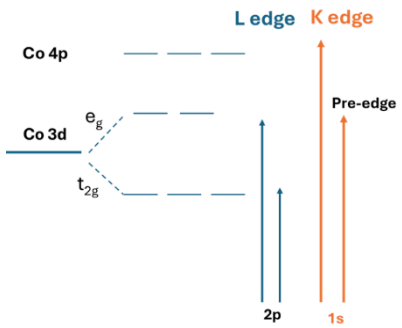

Figure 3.24: Transitions in Co L and K edges.

As a specific example relevant to this dissertation, in a Co atom, the K-edge corresponds to a 1s → 4p electronic transition, while the L-edge corresponds to a 2p → 3d transition (Figure 3.24).

3.6.2 XANES Theory

The X-ray absorption μ(E) can be described by Fermi's golden rule [55]:

$$\mu(E) \propto \sum \left|\langle \psi_f | (e \cdot p) \exp\big(i(k \cdot r)\big) | \psi_i \rangle\right|^2$$

Here, $|\psi_i\rangle$ specifies the initial quantum state and $|\psi_f\rangle$ the final quantum state, e is the X-ray electric vector, p the electron momentum vector, k the X-ray forward propagation vector and r the electron coordinate. The summation is over all final states that contribute to μ(E). Using the first two terms of a series expansion of the exponential gives:

$$\mu(E) \propto \sum \left|\langle \psi_f | (\boldsymbol{e} \cdot \boldsymbol{p}) + i(\boldsymbol{e} \cdot \boldsymbol{p})(\boldsymbol{k} \cdot \boldsymbol{r}) | \psi_i \rangle\right|^2$$

The expansion is limited because only these two terms are expected to contribute to X-ray absorption significantly [118]. The first term is called electric dipole-allowed transitions, characterized $\Delta l = \pm 1$ and is represented by $\mu_D(E)$:

$$\mu_D(E) \propto \sum \left|\langle \psi_f | (e \cdot p) | \psi_i \rangle\right|^2$$

These dipole transitions are the most intense transitions and can be thought of as being stimulated by an oscillating electric field. The second term is the quadrupole transitions, characterized by Δl= ±2 and given by:

$$\mu_D(E) \propto \sum \left|\langle \psi_f | (e \cdot p) | \psi_i \rangle\right|^2$$

Quadrupole transitions are generally of low intensity and can be thought of as being stimulated by the electric field gradient, which for X-rays becomes increasingly significant at high X-ray energies due to the short wavelength. In the case of the pre-edge structures of the metal K-edges, the quadrupole transition is important because the 3d density of states is much larger than the 4p density of states and the quadrupole peaks appear in the pre-edge region where there is no 4p density of states [117].

For a 3d system such as Co, it is expected that the K edge data is dominated by an intense 1s→4p dipolar transition (Δl= +1). In the dipole approximation, the shape of the absorption spectrum should look like the partial density of the (ΔL = ± 1) empty states projected on the absorbing site, convoluted with a Lorentzian. This Lorentzian broadening is due to the finite lifetime of the core-hole, leading to an uncertainty in its energy according to Heisenberg's principle [117].

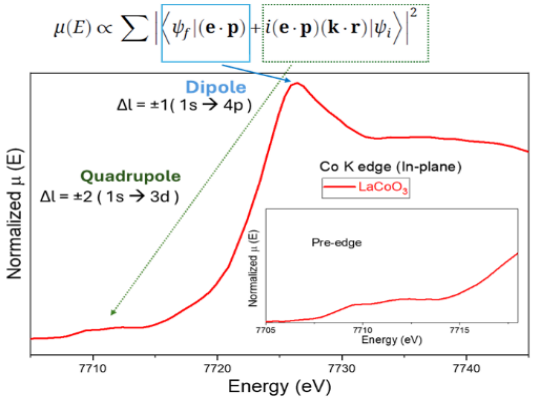

Figure 3.25: Dipole and Quadrupole transitions of Co K edge in $LaCoO_3$.

There is also a weaker quadrupole transition such as 1s⟶3d (Δl= +2) as a pre-edge feature, as shown in Figure 3.25. The intensity of the quadrupole and dipole transitions are related by $\mu_Q / \mu_D = (Z\alpha)^2$, where α = 1/137, is the fine structure constant [55]. For most transition metals, this gives a very small percentage for the quadrupolar term (pre-edge intensity). However, non-centrosymmetric materials (those lacking inversion symmetry) allow a mixing between orbitals of opposite parity (like p and d orbitals) [117]. A 3d-4p mixing causes quadrupole-allowed transitions to gain dipole-allowed intensity, resulting in an enhanced pre-edge intensity [119]. The absorption cross-section due to dipolar transition is isotropic for cubic symmetries such as Octahedral systems, however it varies as ~ $\cos^2\theta$ in Tetragonal systems [118]. Therefore,

analyzing the pre-edge intensity as a function of angle can provide insights into the degree of hybridization in a material. This can help determine any structural distortion in centrosymmetric materials such as in Octahedral coordination environments.

Shake-down and Shake-up transitions:

Shake-down transitions, often observed in the XAS of first-row transition metal K-edges, occur due to significant covalency in metal-ligand bonding.

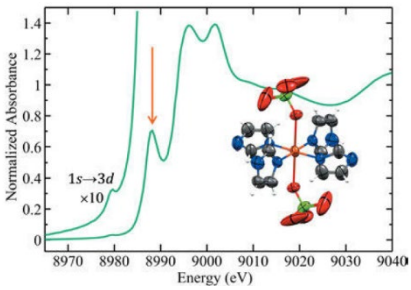

Figure 3.26: Ligand-to-metal charge transfer induced shake-down transition (orange arrow). (Adapted from [55])

Figure 3.27 [55] illustrates this process: Panel A shows the ground state with filled metal 1s and ligand np orbitals, and a vacancy in the 3d orbital. A schematic of a ligand-to-metal transfer transition (LMCT) final state is shown in panel B. Panel C shows a 1s→4p transition, where the core hole causes the outer metal orbitals to relax to lower energies and panel D shows a schematic of both the final state for a 1s→4p and LMCT. The creation of a core hole makes the LMCT (np → 3d) energetically favorable, and the overall final state is energetically lower than that of the pure 1s→4p. Consequently, the shake-down transition, which is dipole-allowed, falls to lower energy by this amount, as shown in Figure 3.26 [55].

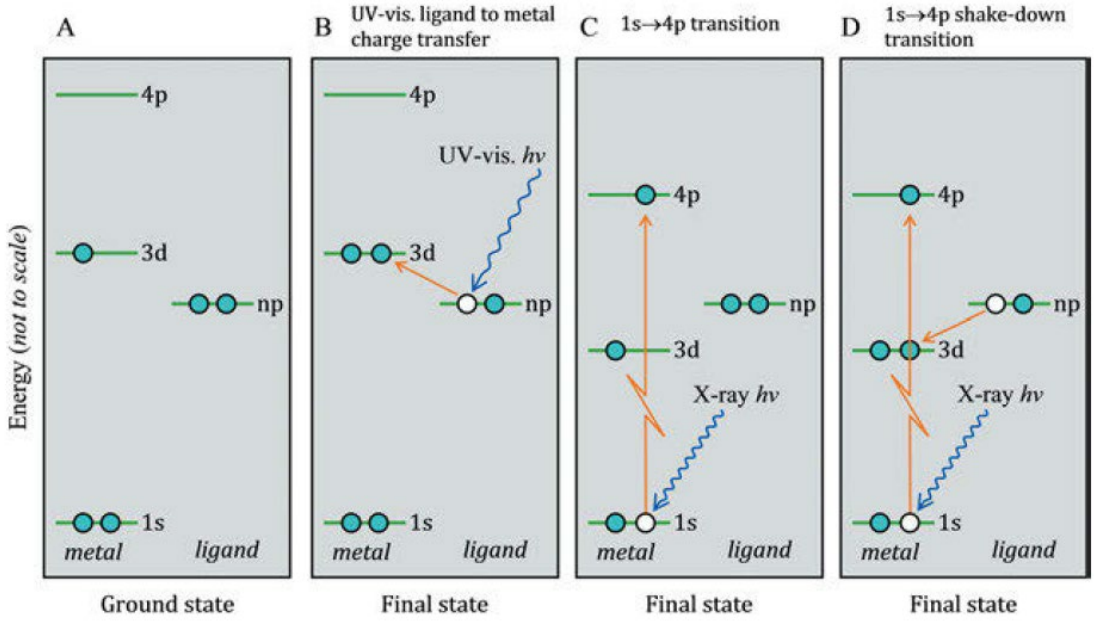

Figure 3.27: Schematic diagrams of processes relevant to 1s→$4p_z$ and LMCT shake-down transition. (Adapted from [55])

A related type of transition is the shake-up transition, shown schematically in Figure 3.28 [55]. A core electron is promoted to a bound state (1s →4p) causing it to relax, but this time this ligand orbital will require energy for np→4p transition. The resulting concerted two-electron one-photon transition requires more energy, thus occurs at higher incident X-ray energies than the corresponding metal-only based one-electron transition.

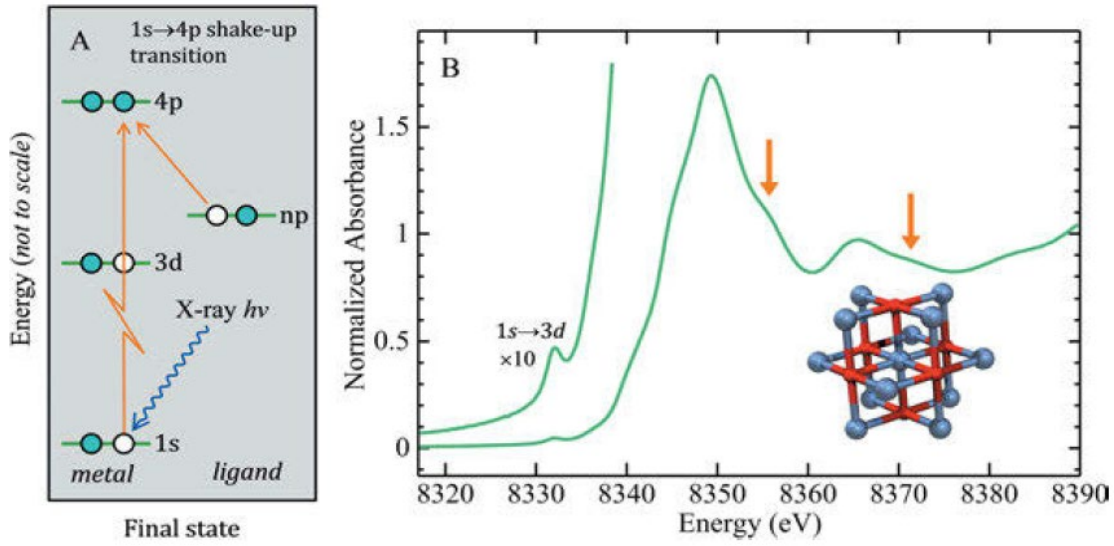

Figure 3.28: (A) A schematic of the shake-up transition. (B) The Ni K-edge XAS of NiO, where broad features marked with the orange arrows are thought to be shake-up transitions. (Adapted from [55])

3.6.3 XANES Analysis

Both K and L-edges can be used to probe the electronic structure of a material of interest and an important step in XANES analysis is the determination of Edge energy.

Metal- K edges: In case of the K-edges of transition metal systems, it is not a trivial task to determine the XANES edge energy position. There are, at least, three different methods to define the energy of the edge [117]: (a) the inflection point, (b) the energy where the intensity is 50% of the edge maximum and (c) the average of the energies at 20% and 80% of the edge maximum. In literature, the inflection point is usually determined from the maximum of the first derivative. However, in the seminal paper, the author referred to the first inflection point in the derivative spectrum [120], not simply the maximum one. Since there is no consensus, the most common procedure- maximum of the first derivative, is used as the Edge energy for this dissertation. On the other hand, the pre-edge energy (E_{pre}) is simply defined as the first maximum of the pre-edge.

Metal- L edges: The L edge energy position shifts with valence, thus L edge can also be used to determine the oxidation state of a constituent atom in a material. Assigning the edge energy is relatively straightforward in L edge, it's simply the maximum of the spectrum called the White line. An experimental parameter that has been often analyzed from L edge data is the branching ratio, defined as: $I(L_3) / [I(L_3) + I(L_2)]$ [121], which can be used to determine the spin state of a metal ion.

3.6.4 Experimental aspects

Prior to doing experiments one has to select an appropriate beamline at a suitable synchrotron radiation facility that must be capable of collecting data over the appropriate energy range of interest. The energy range must be calibrated, for example using metallic reference foils. Furthermore, an internal standard should be used if experiments are going to be performed on the same samples and edges at different beamlines as the energy position may change slightly from beamline to beamline due to different facility characteristics. In addition, for quantitative measurements of oxidation states, a set of standards must be used with well-known oxidation states [117].

3.6.5 XANES detection modes

Some of the most common detection modes are as follows and illustrated in Figure 3.29 [122].

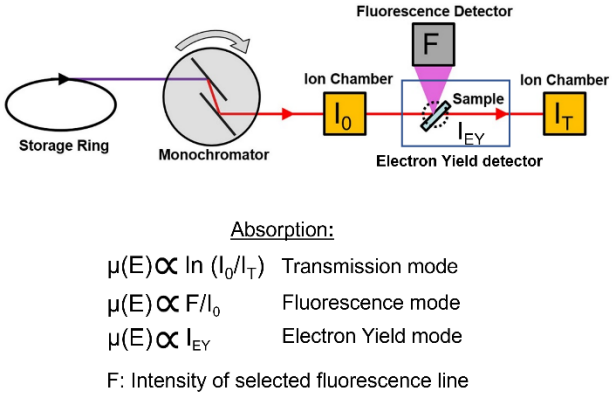

Figure 3.29: XAS detection modes. (Adapted from [122])

Transmission: Transmission detection requires a homogeneous sample, as variations in thickness or pinholes can introduce non-linear effects that distort the spectrum. While transmission is standard for hard X-rays, it is rarely used for soft X-rays due to their short attenuation length [117].

Electron yield: The decay of a core hole produces electrons, photons, and ions that escape from the sample surface. Measuring these decay products allows analysis of samples with arbitrary thickness. Due to strong electron–solid interactions, only electrons from near the surface (1–10 nm) escape, making electron yield a surface-sensitive technique [117].

Fluorescence: The electron subject to photoexcitation in X-ray absorption is typically very tightly bound. Consequently, the core hole created by X-ray absorption will have a very short lifetime and will be rapidly filled by decay of an outer electron. The excess energy from this relaxation is released either as an Auger electron or as an X-ray fluorescence photon. The fluorescence decay of the core hole can be used as the basis for the absorption measurement. The amount of fluorescent decay increases with energy and dominates over Auger decay for hard X-ray experiments [55,117]. For interfacial charge transfer study in our superlattice and double perovskites samples, we used the fluorescence mode.

3.6.6 X-ray linear dichroism (XLD)

Linear dichroism refers to the angle dependent effects when the direction of the linear polarized **E** vector is changed relative to the sample. In an X-ray absorption experiment, for linear polarized X-rays, the electric field vector **E** acts like a search light for the direction of the number of empty valence states. The transition intensity is directly proportional to the number of empty valence states in the direction of **E,** as shown in Figure 3.30 [123]. The charge distribution of the individual p and d orbitals is asymmetric in space in many cases and therefore transitions to individual p and d orbitals will depend on the orientation of the **E**-vector relative to the x, y, z coordinate system of the crystal. This is the origin of the natural linear dichroism effect [124].

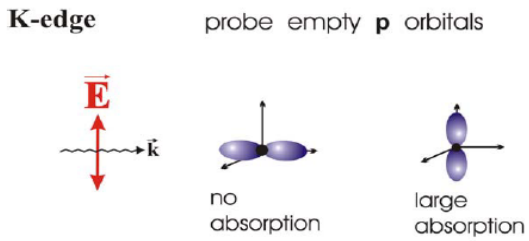

Figure 3.30: An example of search light effect in K-edge. (Adapted from [123]

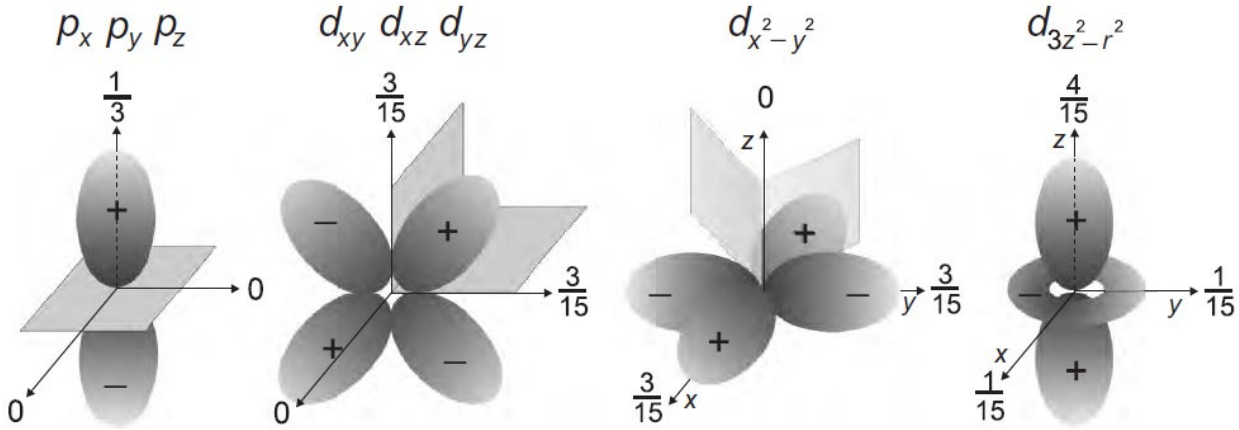

Figure 3.31**:** Polarization-dependent core to valence transition intensities for **E** along the principal coordinate axes. The intensities shown for the four basic symmetry cases: s→ p_i (i = x, y, z), p→ d_{ij} (i ≠ j = x, y, z), p → d_{x2-y2} and p → d_{3z2-r2}. All intensities are per orbital per spin in units of atomic radius squared (AR^2). (Adapted from [124]

XLD is very sensitive to deviations of the local valence charge in the atomic volume from spherical symmetry. By measuring X-ray absorption along three orthogonal directions, we can determine the projection of the number of holes along the three directions, as illustrated in Figure 3.31 [124]. In this figure, for L-edges the transition intensity is zero if the **E**-vector lies along the d orbital nodal axis, which is the intersection of two nodal planes. In our study, we focused on measurements with the **E**-vector oriented parallel and perpendicular to the crystal c-axis. We probe anisotropies in terms of both energy levels and hole density in the two directions.

3.7 Electron Microscopy

Human eye is unable to see individual atoms using traditional light microscopy as optical wavelengths are far too large to resolve individual atoms. However, the wavelengths of electrons are much smaller than atomic dimensions, paving the way for atomic-scale imaging using electron microscopy, thus to seeing the atoms through electrons [125]. Scanning Transmission Electron Microscopy (STEM) represents an advanced electron microscopy, providing atomic-resolution imaging and spectroscopic analysis capabilities using a highly focused electron beam. Currently, STEM resolution has reached sub-angstrom levels, with imaging capabilities down to 0.5 Å [126]. Unlike scanning electron microscopy (SEM) or scanning probe microscopy (SPM), which primarily probe surface features, transmission electron microscopy (TEM) and STEM allow researchers to "see into" the bulk of materials, providing insights into internal structures at the atomic scale [125]. STEM has emerged as one of the most powerful characterization tools employed by material scientists, in large part due to its unmatched spatial resolution and flexibility [127].

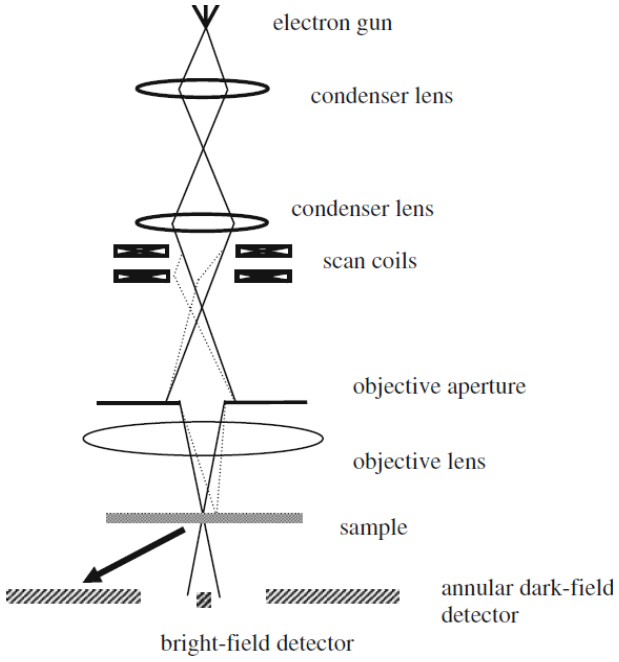

Figure 3.32: A schematic diagram of a STEM instrument. (Adapted from [128]

Figure 3.32 [128] illustrates a schematic of the Scanning Transmission Electron Microscope (STEM) optical configuration. There is a highly coherent electron source consisting of a tip and an anode to generate free electrons, a tube of electrodes to accelerate the electron beam to voltages of 20–300 kV [127].

A series of electromagnetic lenses focuses the electron beam into a fine probe that is directed onto a thin, electron-transparent sample. All lenses preceding the sample are known as condenser lenses, except for the final focusing lens, which is called the objective lens. The primary function of the lens system is to demagnify the finite-sized electron source sufficiently to form an atomic-scale probe at the sample. The objective lens provides the final and most significant demagnification step. However, it also introduces the most prominent optical aberrations in the system. To mitigate these aberrations, an objective aperture is used to limit the numerical aperture of the lens. This has two key consequences: 1) it imposes a diffraction limit to the smallest probe diameter that may be formed and 2) electrons that do not pass through the aperture are lost, and therefore the aperture restricts the amount of beam current available. Scan coils are used to raster the probe across the sample. As the probe scans, various scattered signals are collected and mapped to generate a magnified image. STEM offers a wide range of signal detection modes as shown in Figure 3.33(a) [129], a notable of them are the following.

- In the **Bright Field (BF)** mode, transmitted electrons are detected that exit the sample at low angles relative to the optic axis (usually smaller than the incident beam convergence angle)
- In the **Annular Dark Field (ADF)** mode, transmitted electrons leave the sample at relatively high angles with respect to the optic axis (usually at an angle several times the incident beam convergence angle). One of the most powerful features of STEM is Z-contrast imaging (Z for atomic number), achieved through high-angle annular dark-field (HAADF) detectors (A schematic of these three modes is shown in Figure 3.33(b) [130]). In this mode, image contrast is approximately proportional to the square of the atomic number (Z^2) [128]. Modern STEM imaging experiments typically utilize multiple simultaneous detectors in a far-field diffraction plane including ADF, HAADF, BF and segmented detectors for differential phase contrast (DPC). Despite the measurements

taking place in a diffraction plane, the resulting signals are 2D images (or 1D line traces) where each pixel corresponds to a different probe position on the sample surface [127].

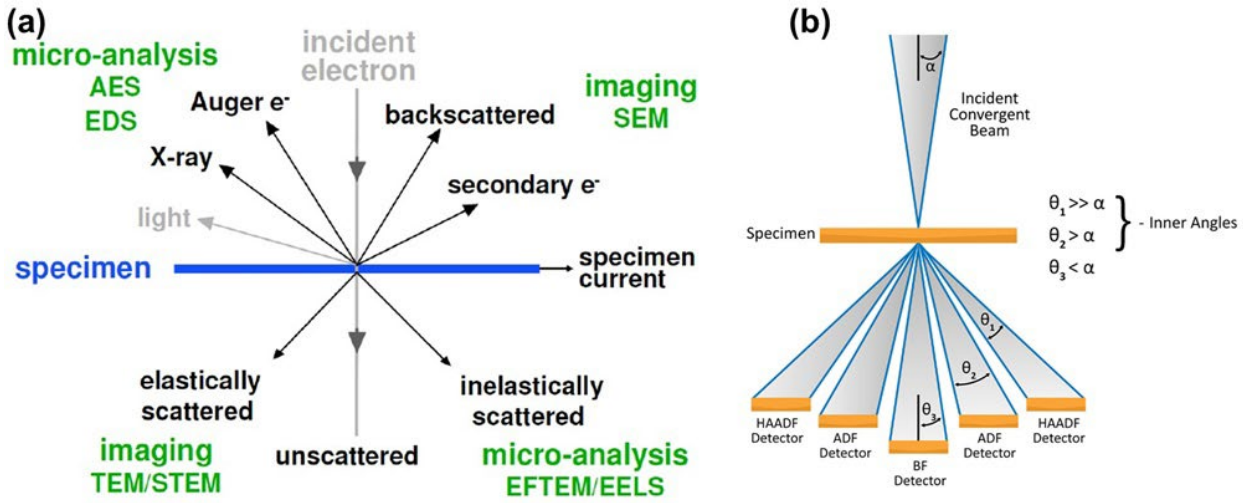

Figure 3.33: (a) interactions between the electron beam and the target material, (b) Schematic diagram of STEM detector set up. (Adapted from [129] and [130])

- **Electron Energy Loss Spectroscopy (EELS)**: Analyzes transmitted electrons that have lost energy while passing through the sample, producing a spectrum based on energy loss. EELS spectrum provides detailed information about electronic structure, chemical bonding, and local atomic environment [131].
- **Energy-Dispersive X-ray Spectroscopy (EDX)** detects characteristic X-rays emitted from the sample due to inelastic interactions. EDX enables quantitative elemental analysis and chemical mapping at the atomic scale [132].

Chapter 4 : Thin Film Growth and Characterizations

4.1 Introduction

High-quality thin films were synthesized using Molecular Beam Epitaxy (MBE) under ultra-high vacuum (UHV) conditions, with a base pressure of approximately 2×10^{-8} Torr. Successful thin film growth using MBE requires careful optimization of several parameters, including the flux ratio calibration, growth environment (temperature and pressure), substrate selection, substrate treatment, annealing (if necessary) etc. Each of these factors plays a critical role. Given the sensitivity of MBE, even minor deviations can result in failure to achieve the desired film quality or phase. Among these parameters, considerable effort was devoted to identifying the optimal temperature and pressure conditions necessary to stabilize the desired phases, especially for $SrCoO_3$ films and $SrIrO_3$/$SrCoO_3$ (SIO/SCO) superlattices.

This chapter begins with a list of operational modes of different instruments that guided back and forth to successful film growth. These tools were essential for real-time feedback and post-growth analysis of film quality. Following that, detailed discussions are presented on the synthesis of $SrCoO_3$ single-phase films, $SrIrO_3$/ $SrCoO_3$ superlattices, and Sr_2CoIrO_6 double perovskites, with a focus on the conditions that led to successful growth. The chapter concludes with a discussion of some of the notable challenges encountered during the growth process and point out some key lessons.

4.2 Characterization backgrounds

To achieve high-quality thin films and optimize growth parameters, a three-stage primary characterization approach was employed for all films. Reflection High-Energy Electron Diffraction (RHEED) was used during film growth to monitor surface morphology and crystallinity in real time. Following growth, the films were transferred to the X-ray photoelectron spectroscopy (XPS) system via an ultra-high vacuum (UHV) transfer line. XPS was used to characterize the chemical state of constituent elements, determine stoichiometry and estimate

film thickness of the thinner samples (≤5 nm). Following that, an ex-situ X-ray diffraction (XRD) was used to determine the crystal structure of the film. Feedback from these characterizations was used iteratively to refine and improve the subsequent growth. The standard operating conditions of the regular set of experiments for thin film synthesis are as follows:

To obtain RHEED data, A KSA 400 RHEED system was operated in a constant accelerating voltage of 15 KV and a filament current of 1.6 - 1.7 Amperes. Stage temperature was measured and monitored using a thermocouple attached directly to the stage heater. For each film and during all stages including temperature ramping up, substrate annealing, film deposition and cooling, we used oxygen plasma generated by a 300-Watts radio-radio-frequency plasma source operating at 13.56 MHz. In-vacuo XPS was performed in a PHI 5400 XPS system using monochromatic Al K-α source (photon energy 14.5 KeV).

Figure 4.1: Elemental Sr Source.

The XRD study was performed in a Rigaku SmartLab system with a Cu K-α source in the parallel-beam geometry operated at 40 KV and 30 mA. Film thicknesses and roughness were further analyzed by X-ray reflectivity (XRR) using the GenX software package [133].
The precursors used for film growth described in this chapter are as following: elemental strontium (Sigma-Aldrich, 99.99%) and iridium(III) acetylacetonate (Strem Chemicals, 98%)

4.3 $SrCoO_3$ (SCO) growth and characterizations

4.3.1 Backgrounds

$SrCoO_3$ thin films were epitaxially grown on $LaAlO_3$ (LAO) (100) and $(LaAlO_3)_{0.3}(Sr_2AlTaO_6)_{0.7}$ (LSAT) (100) substrates obtained from MTI Corporation. Prior to each growth, substrates were sequentially sonicated in Acetone to dissolve organic compounds, followed by Isopropyl alcohol to remove non-polar compounds- each for a minimum of 5 minutes. As the substrates from MTI were already pre-cleaned and vacuum sealed, in several cases, substrates were loaded directly into the chamber and surface treatment was performed using just oxygen plasma. Both sonicated and as-received substrates exhibited excellent surface quality and facilitated the growth of high-quality films. Most of the films were grown on 10 mm × 10 mm substrates, while 5 mm × 5 mm substrates were used to optimize growth conditions in the preliminary samples.

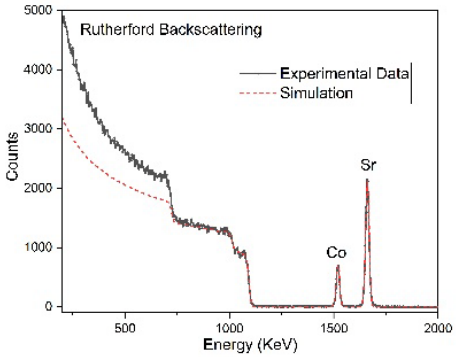

Figure 4.2: Rutherford backscattering spectroscopy simulation.

Elemental strontium and cobalt were used as source materials and thermally evaporated from effusion cells, operating in the range of 440 °C - 490 °C and 1280 °C - 1320 °C respectively. Fluxes were calibrated using a Quartz Crystal Microbalance (QCM) to achieve a 1:1 stoichiometric ratio. Rutherford backscattering spectrometry (RBS) was employed to correlate QCM flux readings with the actual deposition rates (Figure 4.2). RBS was used periodically to verify and adjust flux calibrations. For RBS, MgO, $MgAl_2O_4$, Al_2O_3 were used as substrates as they are free of heavy elements. This helped avoid spectral interference that would have otherwise complicated accurate quantification of Sr and Co concentrations.

Prior to deposition, LAO and LSAT substrates were annealed in Oxygen for about 30 minutes at 800 °C and 850 °C respectively in presence of oxygen plasma. Substrate annealing duration was occasionally adjusted based on the RHEED patterns of the bare substrate. The temperature was subsequently reduced to the growth temperature at a rate of 20°C/min. An optimal growth

temperature window of 580 – 630 °C was determined for the SCO films. Below 580 °C, the films tended to become amorphous, whereas temperatures above this range led to the formation of significant amounts of undesired phases. During deposition, an oxygen flow rate of 1.5 standard cubic centimeters per minute (sccm) was maintained, resulting in a chamber pressure of approximately 1×10^{-5} Torr.

Both layer-by-layer and co-deposition growth methods were explored for growing SCO films. Both methods yielded excellent film quality, though co-deposition method was mostly used to mitigate potential flux variations during extended growth periods. For most of the films, growth rates were in the range of 55- 110 seconds(sec)/unit cell(uc). For growth rates of (55 sec/uc), intermittent annealing was required (up to every 5-unit cell). The optimal annealing duration depended on the growth rate; for instance, a growth rate of 55 sec/unit cell corresponded to an optimal annealing period of 40-70 seconds, which enhanced RHEED streak quality and Kikuchi lines. Prolonged annealing led to surface roughening. For the growth rate of 110 sec/uc or lower, intermittent annealing was not required for film thicknesses up to 10 nm. However, it was preferred to apply annealing every 10 uc to maintain consistent high crystallinity throughout the growth process. Most of the SCO films were synthesized with a thickness of 10 ± 2 nm, while a small set of samples were grown at reduced thickness (5 nm or even less) and at significantly greater thicknesses (up to 50 nm). Post-deposition cooling was performed under an oxygen flow of 2 sccm ($P \sim 2 \times 10^{-5}$ Torr) at a rate of 15–20 °C/min, and no noticeable differences were observed in this cooling range in film quality or following characterizations. In one growth involving an 8 nm thick film, a much slower cooling rate (5 °C/min) was used. This also improved film quality without introducing additional surface roughness (Figure 4.3). Post-growth cooling generally enhanced surface morphology unless the film was Co- or significantly Sr-rich.

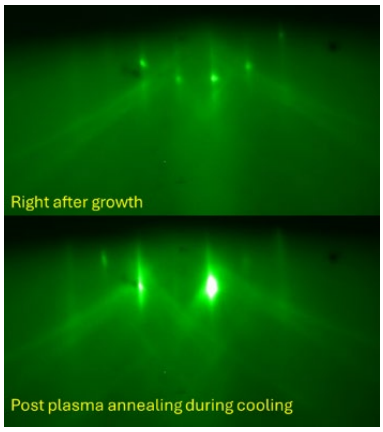

Figure 4.3: Plasma annealing effect.

RHEED was employed for real-time monitoring of surface morphology of the films. Based on experiences with Co-based oxides [134] and $SrIrO_3$ (SIO) film growths [76], the beam was blanked during growth of SCO or SIO layers to prevent reduction of the material except for brief

1-2 second intervals each minute to record a picture. To get insights on the electronic structure of Co and Oxygen, as well as the spin state of Co, soft X-ray Absorption Spectroscopy (XAS) of Co L and O K edges was performed in the Center for Functional Nanomaterials, Brookhaven National Laboratory. For these ex-situ measurements, samples were immediately sealed in vacuum bags upon removal from the load-lock to preserve surface quality and maintain the perovskite phase.

4.3.2 Results and discussions

Figure 4.4(a) presents the RHEED pattern of a $LaAlO_3$ (LAO) substrate immediately prior to film deposition, while Figure 4.4(b) shows the RHEED image of the $SrCoO_3$ (SCO) film on LAO following growth and cooling. RHEED demonstrates excellent quality of the film as indicated by sharp, well-defined diffractions spots and Kikuchi lines. Moreover, a nearly perfect alignment between the substrate and film spots was found, indicating coherent epitaxial growth with minimal interfacial strain or structural defects. It's one of the best RHEED images compared to the existing literature which indicates higher quality of our films. This can be

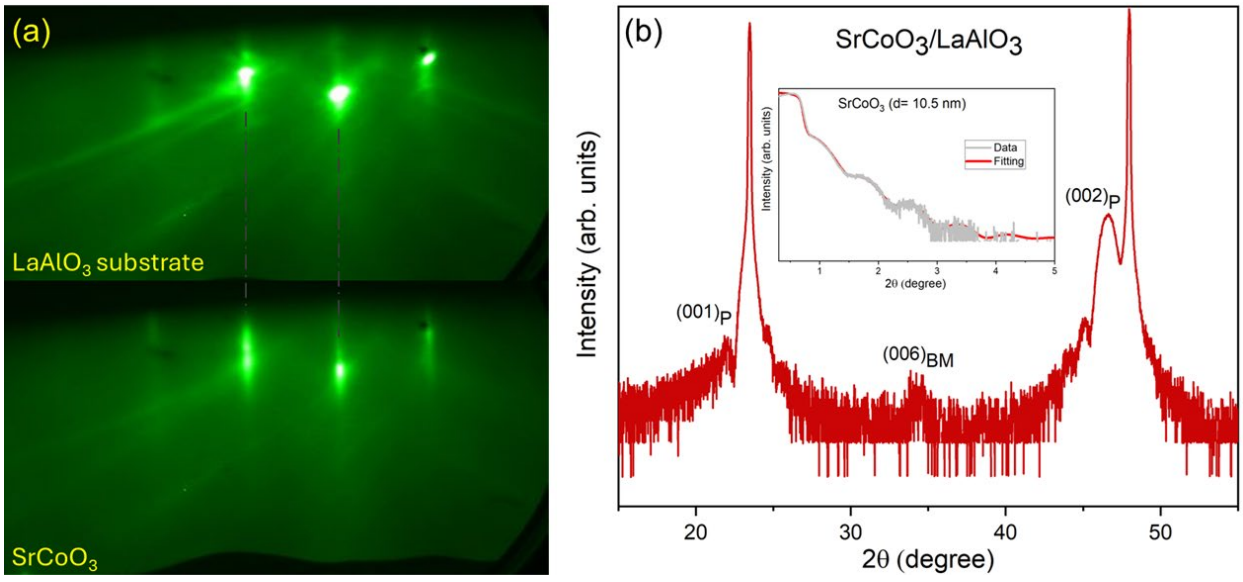

Figure 4.4: (a) RHEED and (b) XRD of $SrCoO_3$.

attributed to the superior stoichiometric control offered by MBE compared to pulsed laser deposition (PLD)- the most common growth method for the SCO films [30,32].

$SrCoO_3$ films exhibited extreme sensitivity to excess Co content. For example, Figure 4.5(b) shows the post-growth RHEED image of a film with only 22% excess Co (Sr: Co= 45%: 55%) than ideal stoichiometric ratio, yet it resulted in a significant amount of secondary phases. Notably, such undesirable extra phases were observed even in ultrathin films only a few unit cells thick with excess Co. On the other hand, SCO films exhibited greater tolerance to excess Sr, though its level depended upon film thickness. For 10 nm thick films with a ratio of Sr: Co= 55%:45%, films still maintained a reasonable quality. The RHEED morphology of the off-stoichiometric films provides clear indicators of whether the films are Sr or Co rich. As shown in Figure 4.5(a) RHEED patterns of Sr-rich films appear streaky, while Co-rich films exhibit spotty patterns.

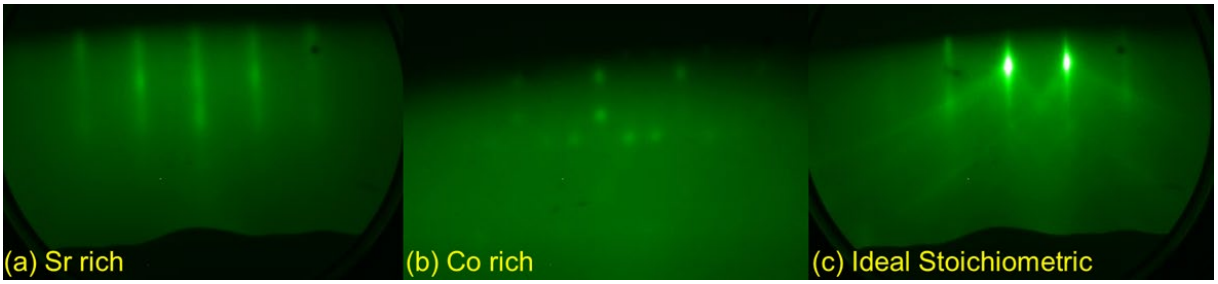

Figure 4.5: (a) Sr rich, (b) Co Rich, (c) Ideal Stoichiometric $SrCoO_3$ film.

The ex-situ X-ray Diffraction (XRD) data in Figure 4.4(b) reveals the predominant presence of the perovskite phase with minor contributions from the brownmillerite (BM) phase, as indicated by a characteristic peak at ~34° [30,135,136]. The BM phase stems likely from a fundamental limitation of MBE growth conditions. MBE is limited to operate in a maximum pressure on the order of 10^{-5} Torr, while achieving a fully oxidized SCO films with Co^{4+} would require two-three

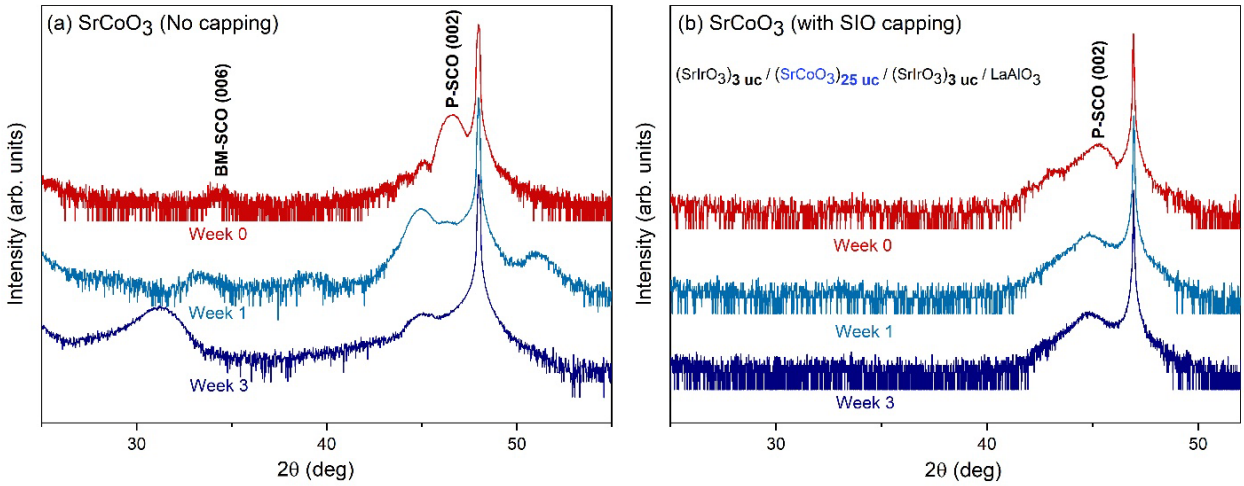

Figure 4.6: $SrCoO_3$ film crystalline quality (a) without (b) with $SrIrO_3$ capping.

orders of higher pressure [30,137]. Films with the perovskites (P-SCO) phase demonstrate extreme sensitivity to atmospheric exposure, readily converting to the BM-SCO phase through the formation of oxygen vacancy channels. However, the phase can be preserved by putting only a few unit cells of SIO layers on the top and bottom surfaces of the SCO film, as suggested by Figure 4.6.

Figure 4.7(a) shows the in vacuo XPS of Co 2p of pure $SrCoO_3$ (Co^{4+}) along with $LaCoO_3$ (Co^{3+}) and $CoMn_2O_4$ (Co^{2+}) [138] as reference spectra. Comparing the Co $2p_{3/2}$ satellite peaks of different oxidation states of Co in literature [139], it can be concluded that a higher oxidation state corresponds to a reduced area in the satellite peak. The weaker Co $2p_{3/2}$ satellite peak in the SCO film compared to references of Co^{3+} and Co^{2+} (marked by orange ellipse) indicates a Co oxidation state higher than Co^{3+}. Similarly, the shake-up satellite at ~72 eV observed in the Co 3p spectrum for LCO(Co^{3+}) in Figure 4.7(b) is nearly absent in SCO, further supporting the presence of Co^{4+} [139,140].

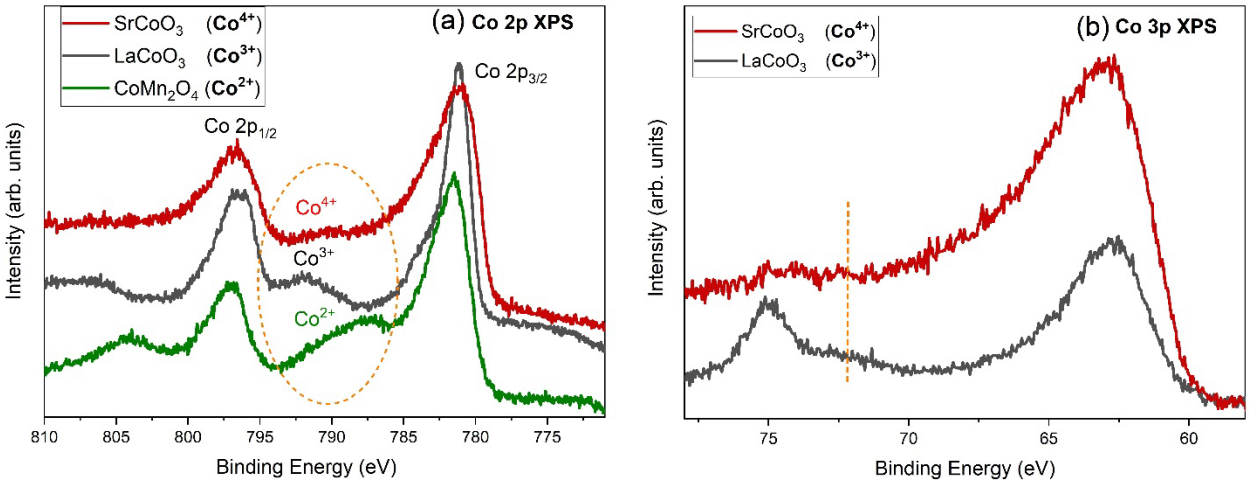

Figure 4.7: (a) Co 2p, (b) Co 3p XPS data of $SrCoO_3$ with references samples.

XAS measurements were conducted on two SCO samples. Both were studied at room temperature, with one sample additionally characterized at 170 K. Although the Co L edge data were analyzed qualitatively without energy calibration, it still provided useful information. While literature reports some discrepancies in the Co L_3-edge energy position [32,141,142], an agreement has been established that Co^{4+} is characterized by a minimized additional edge features in the L_3 edge. For example, the reference data in Figure 4.8(b) [139] shows L_3 edge

spectra for all Sr-Co based systems exhibit a subtle pre-peak at 776.2 eV except for the P-SCO phase. The room temperature measurements for both SCO films, in Figure 4.8(a), lack this feature supporting the presence of the P-SCO phase in our films. However, the L_3 edge data acquired at 170 K suggests a temperature-induced phase transition, although the exact nature of the resulting phase(s) remains undetermined. This P-SCO nature in the films is further supported by the O-K edge spectrum of $SrCoO_3$ in Figure 4.9. The O-K edge measures the density of unoccupied O 2p states and the pre-edge peak at ~530 eV corresponds to Co 3d- O 2p

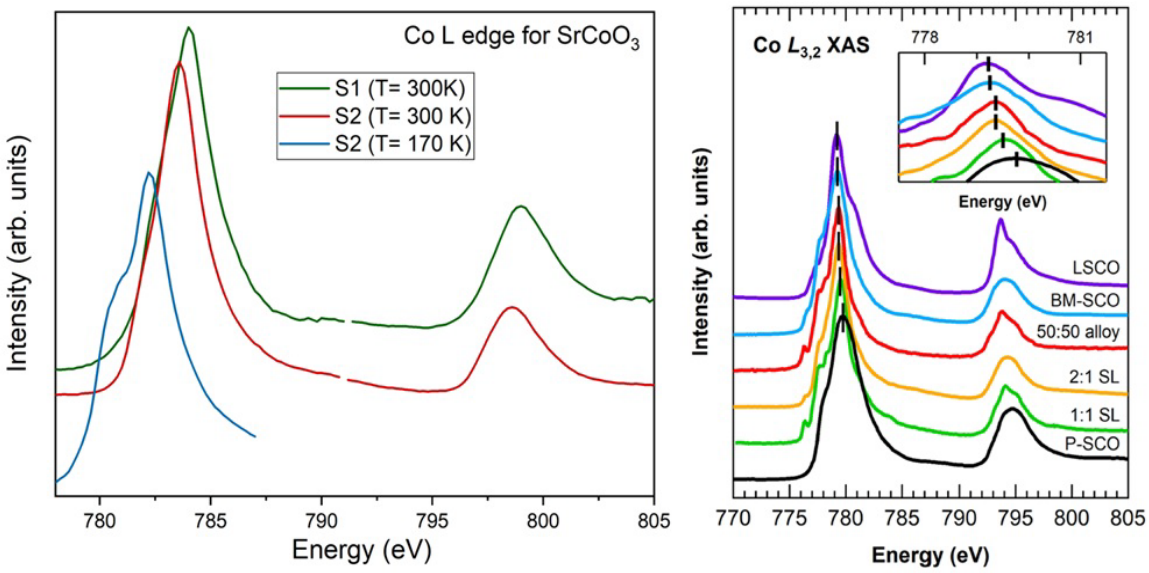

Figure 4.8: (a) Co L-edge XAS data of $SrCoO_3$ films (b) Reference data- adapted from [139].

hybridization occurring via ligand to metal charge transfer (LMCT) [143,144]. There is an increasing LMCT effect with the number of unoccupied states in Co 3d (increasing oxidation state) which results in a more pronounced pre-edge peak [144]. The larger O-K pre-edge intensity observed in our SCO films, compared to previous studies [32] suggests a higher oxidation state of Co in our samples. It was attempted to improve some of the films that underwent into undesirable phases due to degradation from air exposure. Post-growth annealing was performed at 300 °C for 1 hour in an ozone-rich environment using an ozone generator in Prof. Steve May's laboratory at Drexel University. Although some previous works demonstrated that ozone annealing could effectively oxidize Co to the nearly Co^{4+} state [32,135] , this treatment didn't work out in recovering the P-SCO phase in the grown films.

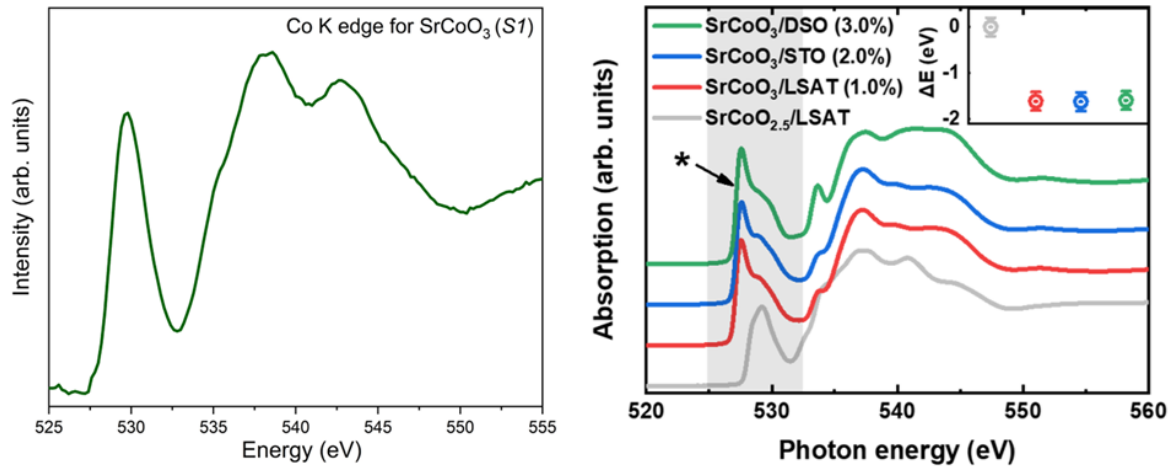

Figure 4.9: (a) O K-edge XAS data of 2 $SrCoO_3$ films (b) Reference data- adapted from [32].

4.4 $SrIrO_3$ (SIO) growth and characterizations

Before discussing the growth conditions for $SrIrO_3$/ $SrCoO_3$ (SIO/SCO) superlattices, a brief overview of the optimized growth parameters for pure $SrIrO_3$ (SIO) thin films is provided. The recipe was developed by Rimal et al. [76] in the FINO lab MBE system.

Strontium was thermally evaporated from the effusion cell, operating between 430 °C and 475 °C that generated a flux rate of approximately 0.01–0.015 Å/s. Iridium was supplied via a metal-organic precursor (Strem Chemicals, iridium (III) acetylacetonate, 98%) that enabled delivery of Ir flux only at 150–173 °C, significantly lower than temperatures required for elemental iridium evaporation (> 2000 °C) [145,146]. In this approach, SIO films were synthesized in the adsorption-controlled growth procedure [147,148], wherein excess Ir atoms desorbed from the surface due to their high vapor pressure. To note, SIO films were originally grown on a variety of single-crystal substrates, including $LaAlO_3$ (LAO) (100) and $(LaAlO_3)_{0.3}$ $(Sr_2AlTaO_6)_{0.7}$ (LSAT) (100), $SrTiO_3$ (STO) (100) and $GdScO_3$ (GSO) to study strain dependence of its electronic behavior.

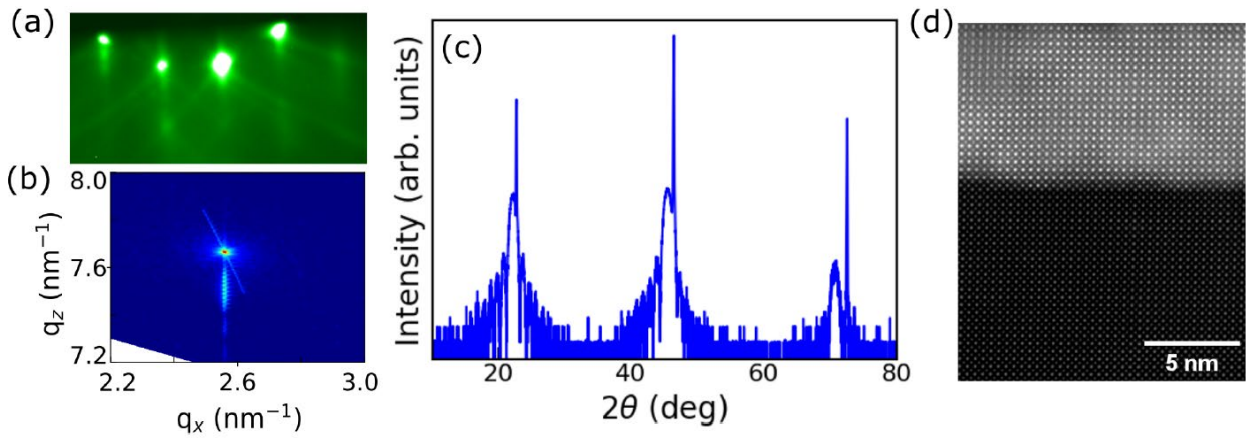

Figure 4.10: Crystal structure data of $SrIrO_3$. (Adapted from [76])

The optimal temperature for epitaxial SIO growth was determined to be 650 °C. An oxygen flow rate of 0.4 sccm was maintained during deposition, resulting in a chamber partial pressure of approximately 6 × 10^{-6} Torr. The oxygen plasma source was continuously operated throughout the growth process to help decompose the metal-organic precursor and facilitate the formation of the desired perovskite phase of $SrIrO_3$. To ensure a clean and smooth surface, only Ir flux was supplied leaving Sr shutter closed, for about 2 minutes both prior to and following the growth. The pre-growth treatment removed residual surface contaminants and improved initial surface flatness, while the post-growth treatment further enhanced surface morphology. Sr rich films led to produce haziness in RHEED pattern which could be improved by supplying only Ir for some extra time to compensate for the missing Ir atoms. Ir rich surfaces showed spotty RHEED patterns, as shown in Figure 4.11(bottom), however annealing the film in oxygen plasma environment would dissolve the extra Ir and remove those undesired features.

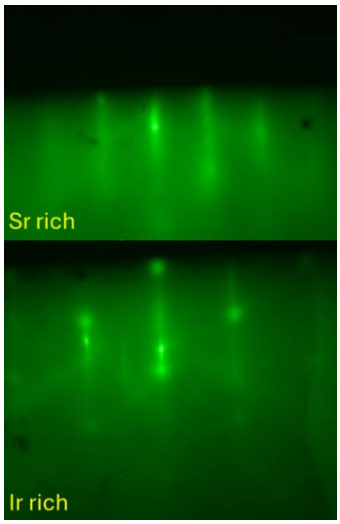

Figure 4.11: Sr rich (top) and Ir rich (bottom) $SrIrO_3$ films.

4.5 $SrIrO_3/SrCoO_3$ (SIO/SCO) superlattice growth and characterizations:

4.5.1 Backgrounds

Three sets of superlattice samples were grown over the course of time. The first was relatively preliminary to optimize growth conditions, the second set was comprehensively studied and specifically designed to investigate interfacial charge transfer phenomena. The third set is currently in the early stages of characterization. Therefore, this chapter will primarily focus on the growth and characterizations of the second set, given its relevance to the charge transfer study, discussed in the next chapter.

Three SIO/$[SCO/SIO]_n$ superlattice films were synthesized using MBE, on (100)-oriented LSAT substrates. The films are characterized by the number of unit cells in individual bilayers such as- 1) SIO, SCO= (4, 2) uc (n= 4 bilayers), 2) SIO, SCO= (5, 3) uc (n= 4 bilayers), 3) SIO, SCO= (6, 4) uc (n= 3 bilayers). They will be represented most often by SL_i and total bilayer thickness (b) in this chapter and following such as: SL1 (b= 6 uc), SL2 (b= 8 uc) and SL3 (b= 10 uc). Thus, charge transfer phenomena were studied tuned by a decreasing ratio of SIO: SCO (2:1, 5:3, 3:2 respectively), while total thicknesses remained roughly constant (11 nm, 14.5 nm , 14 nm respectively). The top-most SIO layer served as a capping layer to prevent degradation in the underlying SCO layer. The LSAT substrate (cubic lattice constant, (a_c= 3.868 ˚A) has a lattice mismatch of 1% with $SrCoO_3$ (a_c =3.829 ˚A) [149,150] and -2.4% with $SrIrO_3$ (bulk pseudo-cubic lattice parameter (3.96˚A) [76,149–151]. Before each growth, the substrate was annealed at 850 °C for 30 minutes and then cooled to the growth temperature (625 °C). A narrow range of growth window (615- 635 °C) was found for the superlattice films.

To grow individual SCO and SIO layers, the same optimized procedures were followed which were established for growing pure SCO and pure SIO films. The same flux rate of Sr for both SCO and SIO layers was maintaned, while Co and Ir flux rates were adjusted to achieve stoichiometric growths in both layers. Following growth, the samples were cooled at a rate of 20 °C/min. In-situ RHEED and in-vacuo XPS were used as like as the pure samples. For the superlattice samples, in addition to the lab-based XPS, an ex-situ hard X-ray photoelectron spectroscopy (HAXPES) study was conducted, using a monochoromated 5.4 KeV microfocus X-

ray source. HAXPES enabled probing the Co oxidation states of deeper SCO layers and investigation of the buried interfaces. All XPS and HAXPES data were calibrated by referencing the primary O 1s peak to 530 eV [76,112]. High-Angle Annular Dark-Field Scanning Transmission Electron Microscopy (HAADF- STEM) combined with energy-dispersive X-ray spectroscopy (EDX) mapping was performed in the Center for Electron Microscopy and Analysis at the Ohio State University to examine the crystal structure and elemental distribution. Polarization-dependent Hard X-ray Absorption Spectroscopy (XAS) was performed on Co K and Ir $L_{2/3}$ edges, the experimental details and results of XAS analysis are discussed in the next chapter.

4.5.2 Results and discussions

The crystal structure data for the *SIO, SCO= (6, 4) uc (b= 10 uc)* film is presented in Figure 4.12- Figure 4.14 as a representative for the superlattices. In-situ RHEED in Figure 4.12(a) clearly shows the Kikuchi lines and sharp diffraction spots confirming high crystalline quality and atomically flat surfaces. A reciprocal space mapping measurement of this film, performed along the LSAT (103) shows uniform Q_z (marked by the dotted vertical line) in Figure 4.13(right). This indicates that each layer is locked to the LSAT substrate, confirming the coherently strained and epitaxial nature of the superlattice structure. The structural quality of the superlattices is further confirmed by STEM measurements, as shown in Figure 4.13(left).

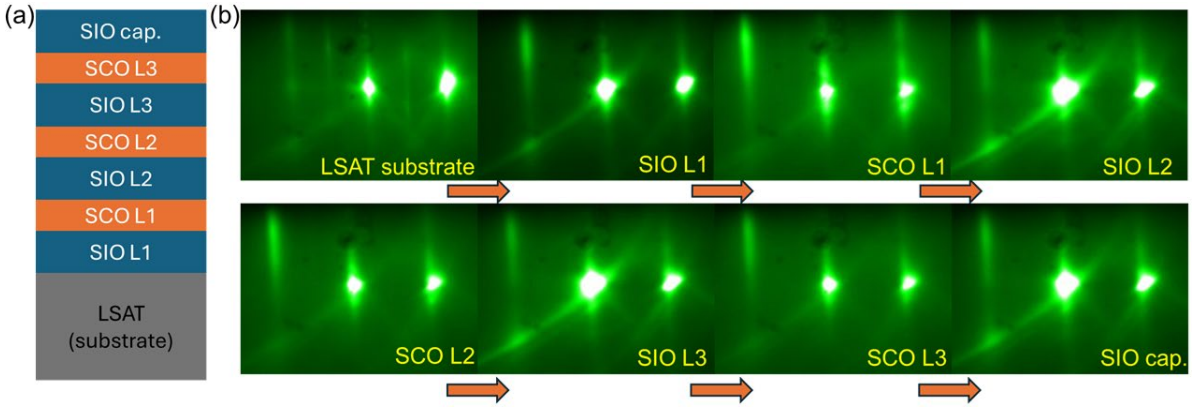

Figure 4.12: (a) Schematic diagram of the (b= 10 uc) superlattice film, (b) corresponding RHEED data.

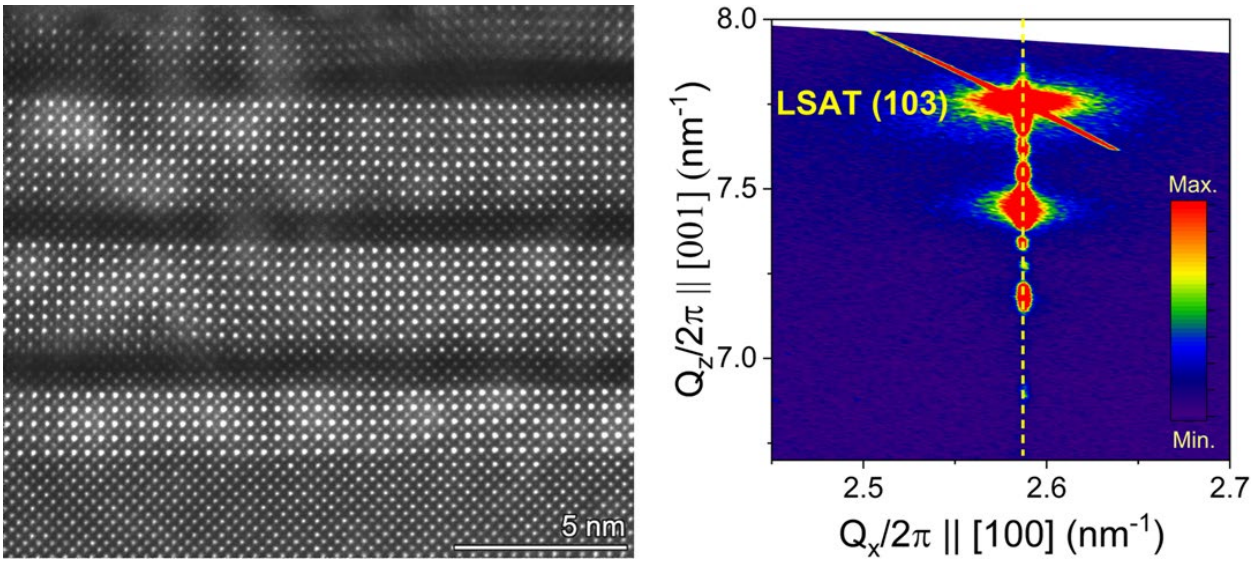

Figure 4.13: STEM and RSM data of the (b= 10 uc) superlattice film.

The XRD Bragg peaks (denoted by 1, 2) in Figure 4.14(a) also demonstrates high-order crystallinity of the films. Superlattice reflections, represented by the satellite peaks (1', 2'), further confirm long-range structural order of the superlattices. XRR simulation (inset) suggests an interfacial roughness between 0.1-0.2 nm and a surface roughness between 0.3-0.4 nm. It's worth highlighting that, although pure $SrCoO_3$ undergoes significant degradation to the brownmillerite phase when exposed to air for over 24 hours, XRD data in Figure 4.14(b) indicates that, when incorporated into a superlattice with $SrIrO_3$, it remains intact even after 6 months.

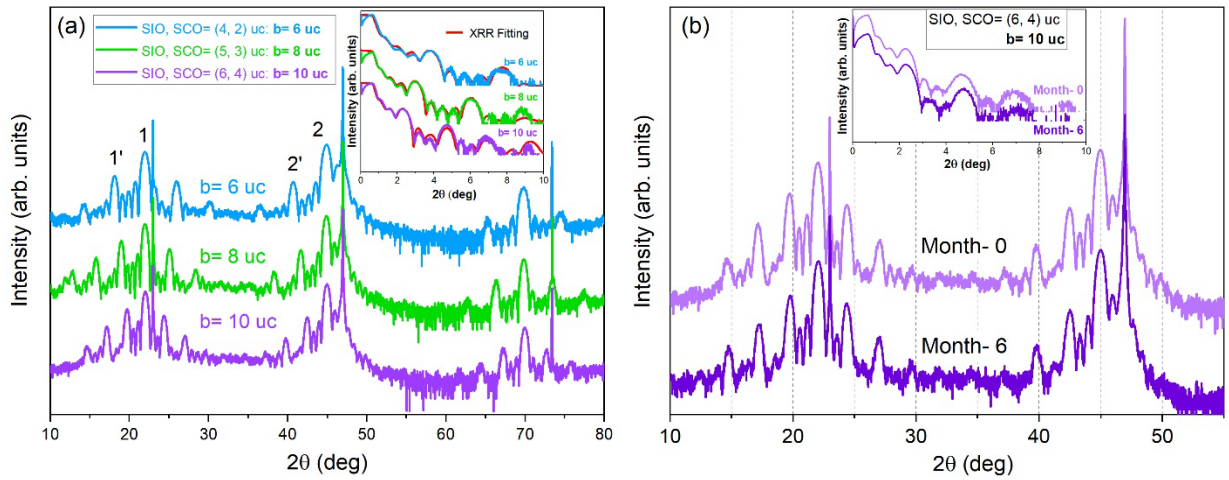

Figure 4.14: XRD data of the three superlattices (XRR fitting is in inset), (b) XRD of (b= 10 uc) SL film in 6 months.

4.6 Sr_2CoIrO_6 (SCIO) growth and characterizations

Sr_2CoIrO_6 (SCIO) films were grown on (100)-oriented $SrTiO_3$ (STO) substrate obtained from MTI corporation. A ratio of 2:1 between Sr and Co was ensured using Rutherford Backscattering Spectrometry (RBS). The STO substrates were annealed in oxygen plasma for 30 minutes at 800 °C. SCIO films were grown at 625 °C, where Sr, Co, and Ir sources were supplied simultaneously. A relatively wide window of growth temperature was observed for the double perovskites (625- 700 °C). An oxygen flow rate of 1.0 sccm (P= 6×10^{-5} Torr) was maintained during growth. To note, this relatively high oxygen pressure was essential for growing and stabilizing the SCIO films, however it contributed to the oxidation of the Ir source material and leading to it's rapid depletion. Because of this, a relatively small number of SCIO films were grown.

To promote cation ordering and investigate any change in electronic structure, one of the SCIO films was post-annealed at 750 °C for 3 hours in a flowing air tube furnace. Due a relatively small difference in cation radii (0.04 A) between Co^{3+} and Ir^{5+} [152], achieving a spontaneously ordered phase in SCIO was inherently challenging [153,154]. Although the ordering parameter is not determined quantitatively, XRD data in reveals presence of superlattice reflections at half-integer lattice constant- *SCIO (111)*. This indicates the formation of an ordered superstructure, providing evidence of spontaneous B-site ordering in our double perovskites [152,155]. Furthermore, in-situ RHEED exhibits two-fold superstructure streaks (highlighted by the dashed orange ellipse) along azimuthal (110) that corresponds to the double perovskite unit cell [155,156]

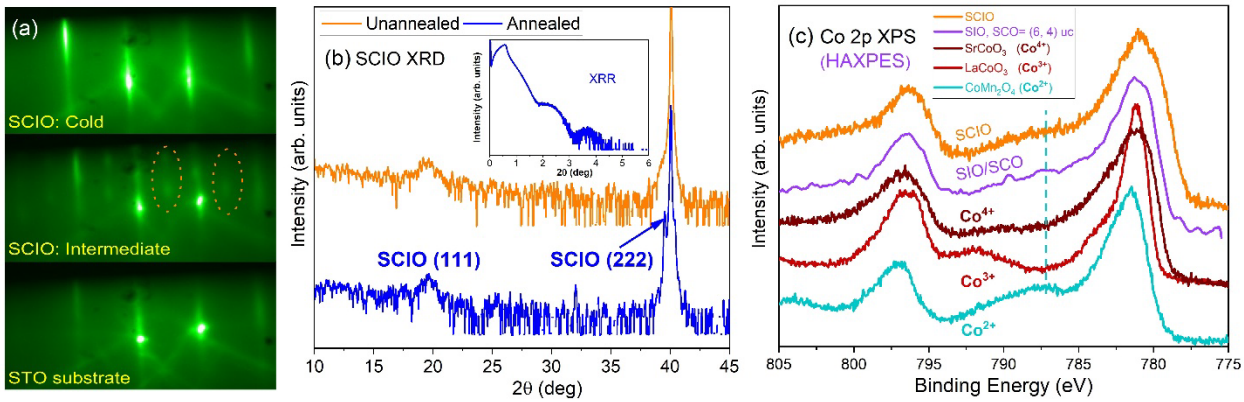

Figure 4.15: (a) RHEED, (b) XRD and (c) XPS of Sr_2CoIrO_6 with HAXPES of (b= 10 uc) superlattice film.

In Figure 4.15(c), the Co $2p_{3/2}$ satellite peaks in the HAXPES data of a representative superlattice and in the XPS of a SCIO sample, comparing with the reference samples, suggest a mixture of $Co^{2+/3+}$ in both these compounds. This deviation from the Co^{4+} state observed in pure $SrCoO_3$ suggests that interfacial charge transfer occurring within these films. A more detailed investigation of charge transfer phenomenon has been explored using X-ray absorption spectroscopy (XAS) in the following chapter.

4.7 $LaCoO_3$ (LCO) growth and characterizations

$LaCoO_3$ (LCO) thin films were epitaxially grown on $LaAlO_3$ (LAO) substrates, which served as reference samples. The Co K-edge X-ray absorption spectroscopy (XAS) of these reference films was utilized to determine the energy position of the Co^{3+} oxidation state. The La effusion cell was heated to 1560 °C, generating a flux rate of 0.046 Å/s, while the Co cell was heated to 1405 °C producing a flux rate of 0.0135 Å/s. Rutherford Backscattering Spectrometry (RBS) measurements of the LCO films were used to calibrate the quartz crystal microbalance (QCM) readings, correlating flux rates with actual deposition rates. Films were grown in an oxygen flow rate of 0.4 sccm (P= 6×10^{-6} Torr) at a substrate temperature of 700°C. A layer-by-layer growth mode was employed to grow LCO films resulting a 10-unit cells of thickness. LCO films were found to be relatively easier to synthesize, and they exhibited structural stability even when exposed to air.

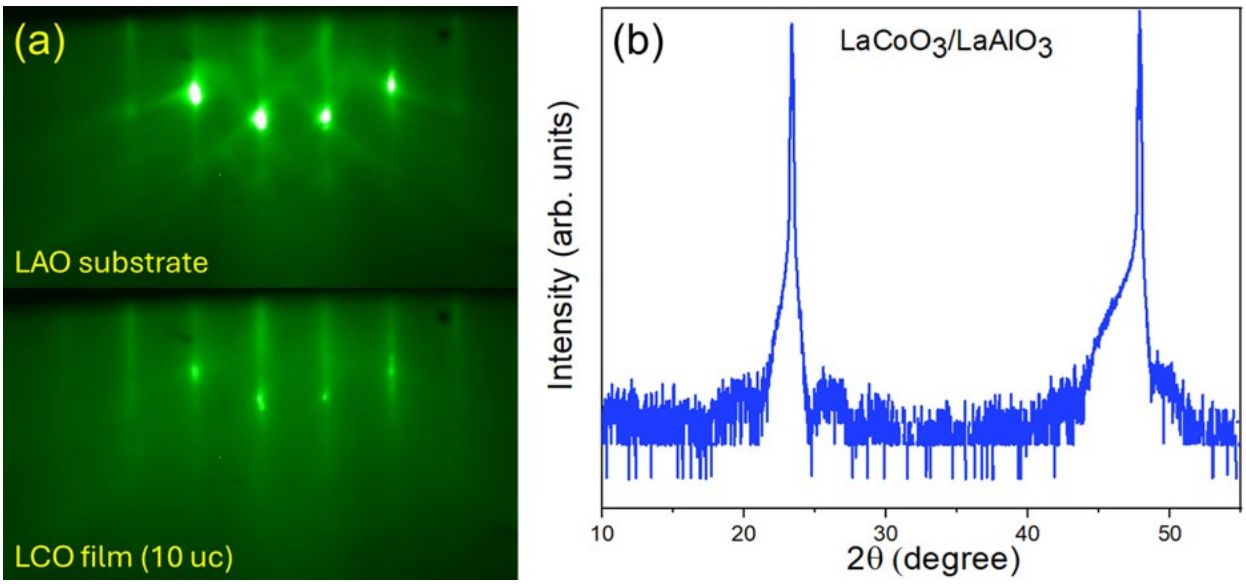

Figure 4.16: (a) RHEED, (b) XRD data of $LaCoO_3$ film of 10-unit cells of thickness.

4.8 Challenges and outlook

Molecular Beam epitaxy enables the growth of extremely clean and high-quality thin films, but this comes with several challenges including frequent maintenance and high operating costs, which are common for all MBE systems.

For me, one major challenge was flux instability, especially for growing superlattice samples that took 4-5 hours of deposition time. Because even a small amount of excess Co led to create extra undesirable and non-removable phases, I had to closely monitor the RHEED pattern for any sign of excess Co. Another major challenge for me was to preserve the pure SCO phase, though using a vacuum suitcase could be used to prevent its degradation for ex-situ measurements. An issue, experienced by each of our group, was the difficulty in removing metal-organic residues from the chamber. We however were able to accelerate chamber cleaning process using an Infra-red light that heated, and effectively desorbed light elements attached to the chamber walls. Still, for certain growths, it was not uncommon to find residual heavy atoms from the previous growths.

Figure 4.17: an image of residuals from a fire occurred during Ir source refilling.

Toxicity of certain elements posed safety concerns, and handling some materials required extra caution. For instance, we experienced a fire incident while refilling the iridium source, a snapshot is shown in Figure 4.17. A challenge for growing SCIO films was that it required a delicate balance between maintaining sufficient oxygen pressure for film growth and avoiding oxidation of the Ir source materials. On the other hand, some substrates were very expensive, but dicing an expensive 10 mm × 10 mm sample into 4 pieces of 5 mm × 5mm was helpful for optimizing growth conditions. Reproducing films is reported as a common issue in MBE growths, though I didn't have to tackle this as a major challenge when all the system components functioned properly.

4.9 Conclusions

Despite its challenges, Molecular Beam Epitaxy stands as a valuable technique because of its ability to produce very clean ultra-thin films. Such a high level of purity is essential for accurate scientific results. Moreover, the ability to control independent growth parameters during growth time gives extra flexibility to change film composition and achieve the desired phases. For example, it was possible to reverse any Sr or Ir rich films by changing corresponding source temperatures during growth. Achieving atomic-scale precision using MBE was a major advantage for my work. I was able to grow precisely 2-unit cells of thin films.Growth of such complex compounds in such precision has vast potential to discover novel physics phenomena and advance modern technologies.

Chapter 5 : Charge Transfer Study using X-ray Absorption Near-Edge Structure (XANES)

5.1 Introduction

As described in chapter 3, X-ray Absorption Near-Edge Structure (XANES), is an established technique to determine the valence state of Ir and Co. Both Ir and Co hold an oxidation state of 4+ in $SrIrO_3$ and $SrCoO_3$ respectively. Therefore, any electron transfer from Ir to Co in the superlattice/double perovskite structure consisting of $SrIrO_3$ and $SrCoO_3$ will result in a higher (lower) than 4+ state for Ir (Co), which was eventually confirmed using Polarization-dependent XAS on the Co K and Ir L_{23} edges. Polarization-dependent XAS further helped probe any asymmetry in charge transfer and anisotropy of electronic structure along in-plane and out-of-plane orbitals in our films. This chapter begins with a Density Functional Theory calculation, performed by Dr. Boris Kiefer from New Mexico State University. In the following, it provides a description of XAS experimental data collection, processing, analysis and offers several explanations on charge transfer, hybridization and orbital reconstruction.

5.2 Computational modeling

To determine the expected degree of charge transfer in these systems, Density Functional Theory (DFT) was employed using the Vienna ab-initio Simulation Package [157,158] accounting for electronic exchange and correlations within the R2SCAN meta-functional [159]. This meta-functional has been shown to improve thermochemistry [160] and electronic structure [161]. Electrons are treated within the projector augmented-wave framework (PAW) [162,163]. Material Project recommendations were followed, and a planewave energy cutoff of E_{cut} = 520 eV [164] and a Γ-centered k-point grid with a k-spacing of 0.25 $Å^{-1}$ were adopted. SCO and SIO perovskites were optimized in the experimentally known cubic (Pm-3m [27]) and orthorhombic (Pnma [34]) equilibrium crystal structures. In preparation for the heterostructure simulations, the cubic structure in the Pnma structure was transformed by a 45-degree rotation in the basal plane

and cell-doubling along the [010] direction and it was found that the energies between the two phases is ~1.0 eV/atom, suggesting that the computations are converged. SCO was found to be a ferromagnetic metal (Table 5.1). The effect of octahedral rotation was also tested, and SCO was placed in computed SIO equilibrium structure. It was found that that the cubic phase was significantly more stable, and octahedral rotation increased the Co magnetic moment by almost 25%. This rotation induced an increase in magnetism as expected: in cubic SCO Co-d and O-2p orbitals showed the highest overlap. With increasing octahedral rotation, the overlap diminished, leading to more localized Co-d orbitals, increasing the magnetic moment as computed (Table 5.1). demonstrating rehybridization of Co-O bonds in the rotated octahedral framework and supporting a Co^{4+} low-spin state. SIO is also metallic, and a sizable magnetic moment of ~ 1 μB/Ir was observed, consistent with a Ir^{4+} in low-spin configuration. However, with including SOC, it was found that this magnetic moment was significantly reduced to ~ 0.1 μB, in better agreement with the absence of permanent magnetism in [34] In contrast, SOC was found to have little effect on the magnetism in SCO (Table 5.1).

Table 5.1: R2SCAN crystallographic parameters of SCO and SIO

	SCO	**SCO**	**SIO**
Phase	Pm-3m	Pnma	Pnma
Lattice	3.807 (3.8289 [27]) (3.89 [164])	5.608 7.902 5.617	5.608 7.902 5.617
Bandgap	metallic	metallic	metallic
Rotation angle (deg)	180.0	154.7	154.7
Magnetic moment (μ_B)	2.856	3.781	0.990
SOC magnetic moment (μ_B)	2.910	0.150	0.116
Formation energy (eV/atom)	0.000	0.158	NA

The primary interest of this study is to better understand the charge transfer in SIO/SCO heterostructures. The heterostructures were generated by stacking Pnma unit cells along [010] direction. Co was added by replacing Ir-O_2 layers with Co-O_2 layers. In the computations, the in-plane lattice parameter was fixed at the value of LSAT, a = 3.868 Å [165], the substrate used in

experiment. In subsequent relaxations the in-plane lattice parameter was fixed, and the z-lattice parameter was allowed to relax. Two types of oxygen ions were distinguished: four equatorial (in-plane, IP) O ions in the TM-O_6 octahedra and two bridging oxygen ions to the Sr-O layers (out-of-plane, OOP).

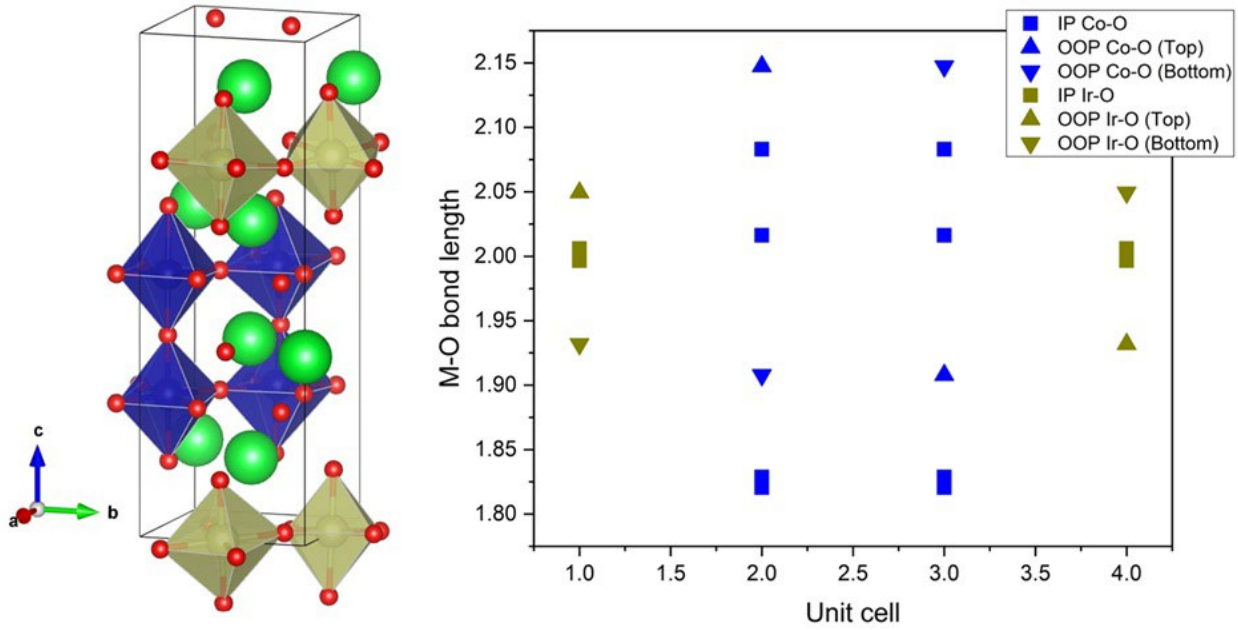

Figure 5.1: Crystal structure and the corresponding bond lengths of the superlattice structures (Blue= Co, Yellow= Ir)

All results were obtained from SOC corrected computations. As a measure to characterize charge transfer the site-projected electronic densities of state was used and the layer resolved number of occupied electrons states were computed by integrating from the lower edge of the d-band to the Fermi level; and for the characterization of oxygen holes, O-2p from the Fermi level to the upper edge of the O-2p band was integrated. Moreover, the layer-resolved O-2p shift in the 40 atom simulation cells with eight formula unit was computed, following Zhong and Hansmann [17]. To note, in SCO/SIO heterostructures O-2p orbitals cross the Fermi level, while in Ref. [17] the O-2p band is located well below the Fermi level. This integration provides a qualitative measure for individual phases, but comparing the heterostructures of this research with compositional endmembers, changes were identified due to heterostructure formation, changes in the TM-O bond network were identified, and insights into the charge transfer mechanism were derived, that could be verified and quantified through XAS experiments.

$Sr(Co_xIr_{1-x})O_3$ charge transfer: Ir in SIO heterostructure shows a small residual magnetic moment of 0.14 μB/Ir and for IP and OOP oxygen, 0.038 μB and 0.007 μB, respectively, and the ground state remains metallic (**Figure 1**). For the corresponding SCO endmember, it was found that it was a ferromagnetic metal, where Co carried a magnetic moment of 2.4 μB/Co, and both IP and OOP oxygen carried a small but non-zero almost degenerate magnetic moment of ~ 0.2 μB, consistent with Co d - O 2p hybridization. Therefore, the magnetism in both phases suggests significant hybridization, a finding that is corroborated by the site projected electronic density of states that shows O-2p states crossing the Fermi level, and O-2p holes in both (strained) endmembers were found. For the TMs and oxygen ions, layer resolved d-orbital occupancies were computed as well as oxygen hole occupancies (Table 5.2 and Table 5.3)

Table 5.2: Layer resolved orbital occupancy 20-atom heterostructures; 5x5x4; IS=-5.

	$Sr_4Ir_2O_{12}$ (5x5x4; IS=-5)	$Sr_4Co_2Ir_2O_{12}$ (5x5x4; IS=-5)	$Sr_4Co_4O_{12}$ (5x5x4; IS=-5)
x_{Co}	0.00	0.50	1.00
0.750, OOP	0.545	0.567	0.632
0.500, IP	6.562; 0.535	**6.785; 0.496**	**7.154; 0.619**
0.250, OOP	0.545	0.567	0.632
0.000, IP	6.562; 0.535	6.245; 0.496	**7.154; 0.619**

From the analysis of the occupied Ir-5d, a monotonous decrease in the heterostructures with increasing Co concentration was found, consistent with an Ir electron donor, this change correlates with the increasing number of IP O 2p holes, both suggesting change in Ir-O hybridization. Conversely, it was found that Co 3d increased, with decreasing Co concentration, supporting charge density accumulation, as does the decreasing hole abundance of IP-O 2p. These results suggest that charge transfer does not occur directly from Ir-O_2 layers into the Co-O_2 layer, but as supported by the correlated TM-IP-O the charge transfer pathway is Ir → IP-O (Ir-layer) → IP-O (Co-layer) → Co, assisted by hybridization. This finding strongly contrasts with the localized orbital picture where oxygen ions are passive spectators in the charge transfer process. In summary the DFT-SOC computations support an Ir-O-O-Co charge transfer mechanism, with predictions that can be verified through XAS measurements.

Table 5.3: Layer resolved orbital occupancy, 40-atom heterostructures; 5x5x4; IS=-5

	$SrIr_6O_{24}$	$Sr_2Co_2Ir_4O_{24}$	$Sr_2Co_2Ir_4O_{24}$	$Sr_3Co_3Ir_2O_{24}$	$Sr_4Co_4O_{24}$
*x*Co	0.00	0.25	0.50	0.75	1.00
0.875, OOP	0.557	0.575	0.570	0.604	0.595
0.750, IP	6.751; 0.591	6.669; 0.586	6.483; 0.647	**6.864; 0.585**	**6.838; 0.591**
0.625, OOP	0.557	0.575	0.534	0.542	0.595
0.500, IP	6.751; 0.591	6.589; 0.608	**6.892; 0.554**	**6.824; 0.525**	**6.838; 0.591**
0.375, OOP	0.557	0.529	0.534	0.520	0.595
0.250, IP	6.751; 0.591	**7.002; 0.446**	**6.892; 0.554**	**6.864; 0.585**	**6.838; 0.591**
0.125, OOP	0.557	0.635	0.403	0.488	0.595
0.000, IP	6.751; 0.591	6.589; 0.621	6.483; 0.647	6.294; 0.673	**6.838; 0.591**

5.3 Instrumental backgrounds and data acquisition:

X-ray absorption data were acquired in the Beamline for Materials Measurement (6-BM), located in the National Synchrotron Light Source-II, Brookhaven National Laboratory. All measurements were conducted at room temperature without any external magnetic field.

Data acquisition was performed in the fluorescence mode in a 4-element vortex silicon-drift detector using a Si (111) monochromator in a step size of 0.5 eV and energy resolution of 1.3×10^{-4} $\Delta E/E$. A glancing angle stage, consisting of 8 sample slots, was mounted in a rotation stage [166]. The rotation stage sits on a tilt stage, allowing fine control of the incident angle. The glancing angle

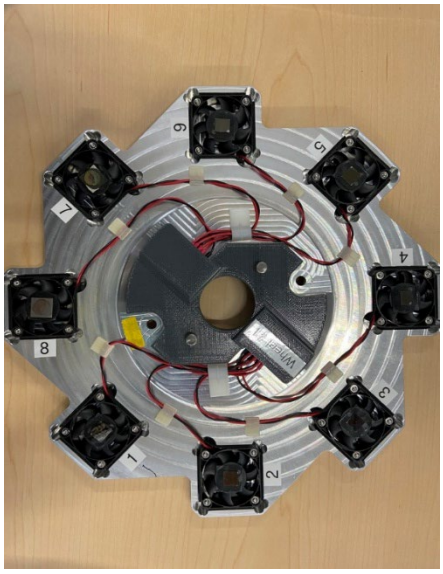

Figure 5.2: The glancing angle stage with 8 spinners (sample positions). (Adapted from [166])

measurement, in which the point of the shallow angle is to spread the beam out over the full length of the sample, significantly increases the number of atoms involved in the measurement. We had our samples spin continuously at a fixed rate during each measurement to suppress spurious diffraction from the substrate.

Measurements were performed on Ir L_2 edge for the superlattice films, Ir L_3 edge for the double perovskites and Co K edge for both sets of films. It was challenging to measure Ir L_3 edge of the superlattice films since a transition peak of Ta from the substrate located close the Ir L_3 energy. To note, Edge energy (Threshold energy) E_0 for Co K edge is defined as the maximum of the first derivative, and for Ir L edge, it's simply the white line position. The absorption intensities were automatically normalized to the incident photon flux in the beamline. Further XAS data reduction and analysis were performed using Athena software from Demeter (version: 0.9.26) library [167]. A list of all measured samples is provided in Table 5.4, where the following data were used as references: Co K edges of LaCoO3 (Co^{3+}) and CoO (Co^{2+}); Ir L_2 (and Ir L_3) edges of pure $SrIrO_3$ (Ir^{4+}) grown on LSAT ($SrTiO_3$). Energy calibration of Co K and Ir L edges was performed by setting a cobalt foil's first derivative maximum of Co K-edge to 7709 eV and a Gold foil's L_3 edge to 11919 eV.

For the Co K edge data processing, the standard steps suggested by [168] in the Athena program was followed. First, a linear pre-edge background was subtracted (-150 eV to -30 eV before the edge) to get rid of other edges. The normalization range differed in different samples; an ideal standard range was 100 eV- 600 eV). The *Rbkg* value was set to 1 Å (represents approximately half the near-neighbor distance). To get accurate dichroism results and integrated intensity differences in different polarizations (orbital polarization), a background subtraction of Ir $L_{2/3}$ edges was performed in the Athena program. First, Ir L_2 edge data (not Ir L_3) was smoothened to reduce noise level using a three-point averaging method (2 repetitions). The background of the $L_{2/3}$ edges was modeled as

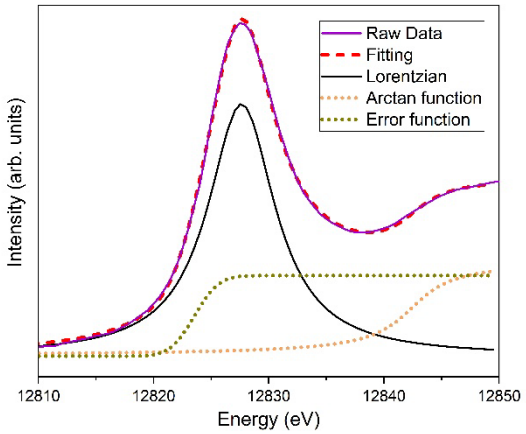

Figure 5.3: Background subtraction in IP Ir-L2 edge for the SL-3 sample.

a convolution of an arctangent and an error function, while a Lorentzian function was used to fit the main edge.

Table 5.4: List of all sampled studied with XAS

Edge	**Ref. samples**	Superlattices **(SL)**	Double perovskites **(DP)**
Co K	$LaCoO_3$/LaAlO3 (Co^{3+}) CoO (unpolarized) (Co^{2+})	SIO, SCO= (4, 2) uc (b = 6 uc) SIO, SCO= (5, 3) uc (b= 8 uc) SIO, SCO= (6, 4) uc (b= 10 uc)	$S_2CoIrO_6/SrTiO_3$ (Unannealed) $S_2CoIrO_6/SrTiO_3$ (Annealed)
Ir L_2	$SrIrO_3$/LSAT (Ir^{4+})	SIO, SCO= (4, 2) uc (b = 6 uc) SIO, SCO= (5, 3) uc (b= 8 uc) SIO, SCO= (6, 4) uc (b= 10 uc)	
Ir L_3	$SrIrO_3$/SrTiO3 (Ir^{4+})		$S_2CoIrO_6/SrTiO_3$ (Unannealed) $S_2CoIrO_6/SrTiO_3$ (Annealed)

5.4 Results and discussions

5.4.1 X-ray absorption near edge structure (XANES) and charge transfer

To characterize the degree of interfacial charge transfer between Co and Ir, synchrotron-based XANES measurements of the Co K and Ir L edges were employed. For Co K edge data, the maximum of the first derivative of the absorption data was used to determine the oxidation state of Co [169]. From the in-plane (IP) polarized XAS data in Figure 5.4(c) the maximum of the first derivative of all superlattices align exactly with $LaCoO_3$, indicating an average of Co^{3+} state. Since pure $SrCoO_3$ films grown in our system exhibit perovskite phase (Co^{4+}) (discussed in the previous chapter), it can be argued that Ir in $SrIrO_3$ donates electrons to Co in $SrCoO_3$ which eventually leads to formation of the stable structure for over 6 months. In the out-of-plane (OOP) polarized XAS data, the maximum value of the first derivative of all superlattices shifts further

towards lower energy, indicating an average Co oxidation state of less than 3+ along the out-of-plane direction. A similar conclusion can be drawn from the Co K edge data of both of the SCIO double perovskites from Figure 5.5. A relatively higher shift is observed towards lower energy for both IP and OOP data, which most likely originated due to a greater interaction between Co and Ir atoms in SCIO compared to minimal interactions only in the thin interfaces of the superlattices.

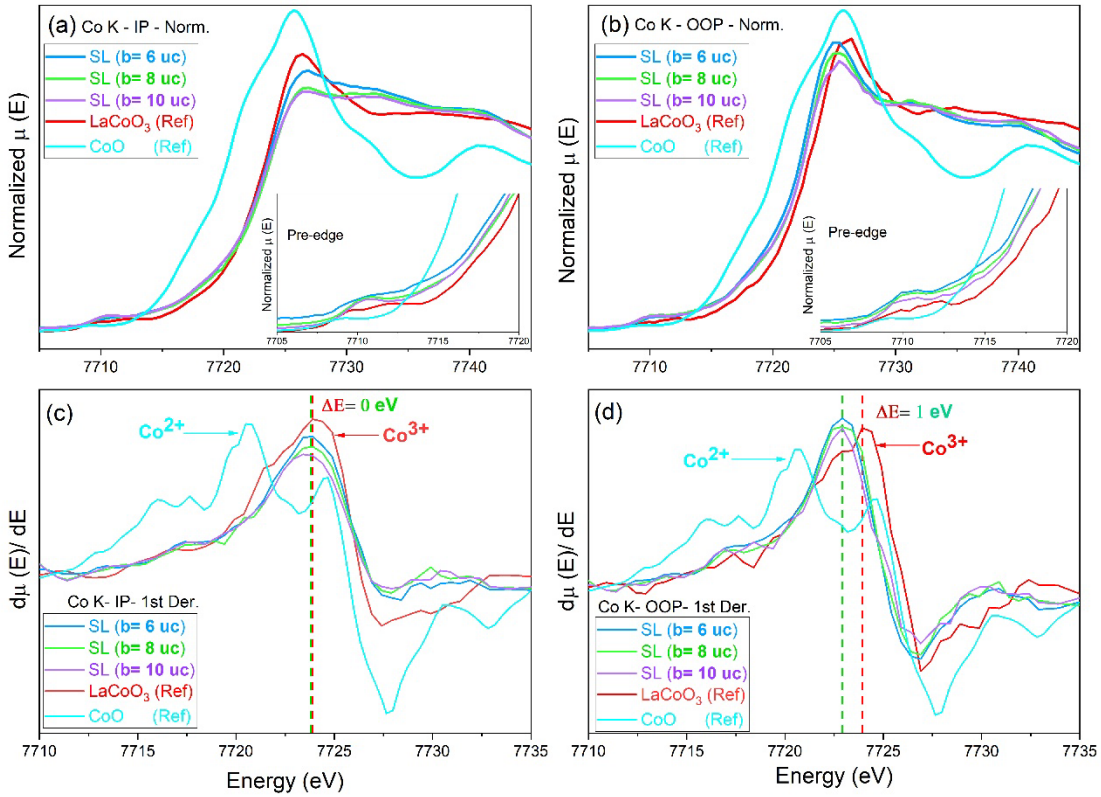

Figure 5.4: XAS Co K-Edge data for superlattice samples (a), (c) In-plane data (Normalized and First derivative of spectra), (b)(d) Out-of-plane data (Normalized and First derivative of spectra).

The white line energy position of both Ir L_2 and L_3 edges can be used to determine the oxidation state of Ir [170–173]. OOP Ir L_2 data of the superlattices samples, as shown in Figure 5.6(a) clearly exhibit double features in their shape which are found only in Ir^{5+} and Ir^{6+} states [170]. According to literature, Ir L_2 white-line shift associated with a full oxidation state change from Ir^{4+} from Ir^{5+} is 1.2- 1.3 eV [170,172,173] suggesting an average state of close to Ir^{5+} for in the superlattice films along OOP orbitals. A noticeable shift from Ir^{4+} along the IP direction is not observed. This doesn't necessarily mean that no charge transfer occurred at all, it may be due to

the bulk sensitivity of the XAS fluorescence mode. Since the interface layer is thinner compared to the SIO layers, the average shift likely remains smaller than the step size of 0.5 eV, making it undetectable in the measurements.

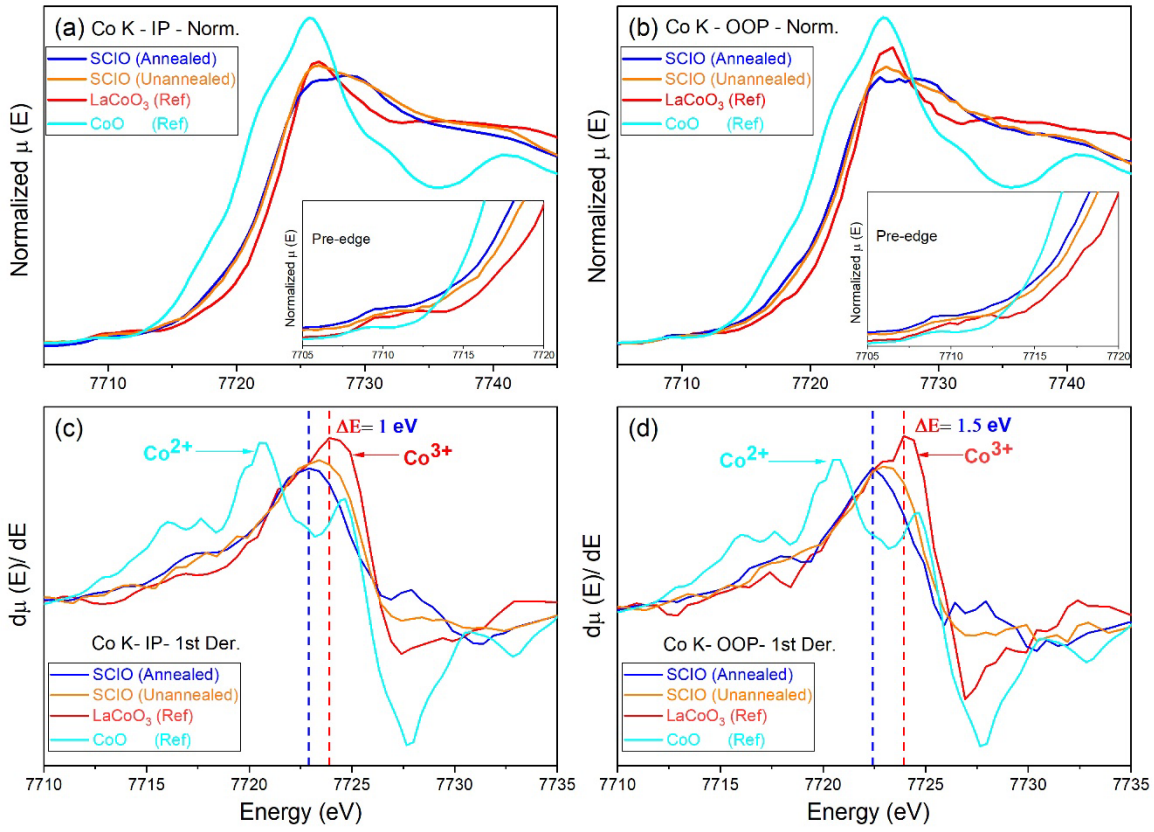

Figure 5.5**:** XAS Co K-Edge data for Double Perovskite samples (a), (c) In-plane data (Normalized and First derivative of spectra), (b)(d) Out-of-plane data (Normalized and First derivative of spectra).

It's unlikely that strain is the origin of the charge transfer phenomena since both pure $SrCoO_3$ and $SrIrO_3$ films undergo negligible change in their electronic structures due to strain [32,76]. Therefore, charge transfer from Ir to Co in our films occurred spontaneously due to the different electron affinity and electronegativity of the two ions, as reflected in the O 2p band center models presented previously [17,174] and further supported by the DFT modeling for the system, described in section 5.2.

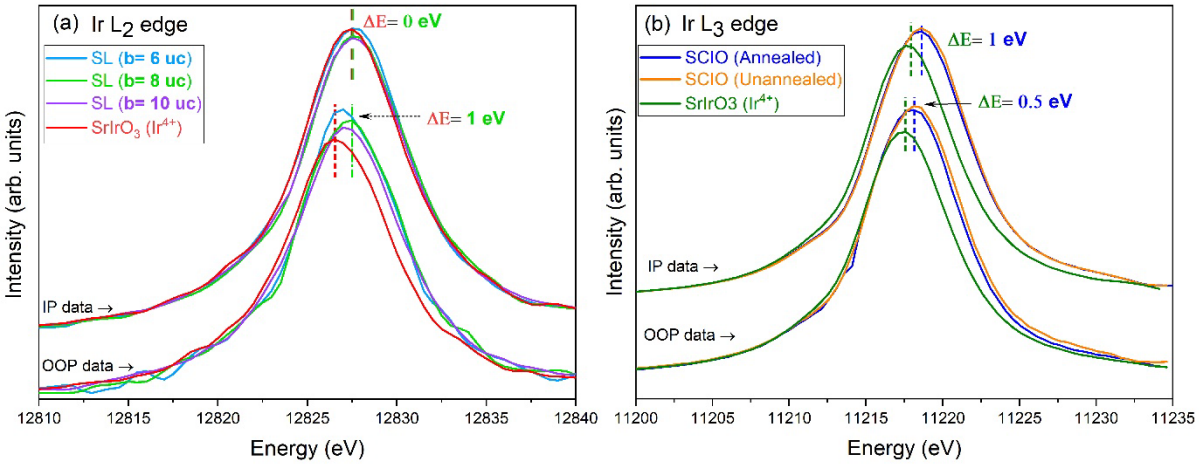

Figure 5.6: (a) Ir L_2 edge of the superlattices, (b) Ir L_3 edge of the double perovskites.

5.4.2 Ir $L_{2,3}$ X-ray linear dichroism (XLD) and anisotropy

X-ray linear dichroism (XLD) provides valuable insights into anisotropy of the electronic structure in superlattice films, where interfaces add an additional degree of symmetry-breaking beyond what may already be present from epitaxial strain [175,176]. Differences between in-plane and out-of-plane polarization may indicate orbital polarization [175] due to charge transfer or polar distortions due to interfacial effects [176]. XLD data for pure $SrIrO_3$ films in Figure 5.7(a) shows that IP Ir L_2 shifts towards higher energy by 1 eV relative to OOP Ir L_2. The transition intensity in the XAS L edge is directly proportional to the number of empty valence states in the direction of **E** [124], therefore IP Ir L2 edge probes only d_{x2-y2} orbitals of e_g band. On the other hand, the e_g band in $SrIrO_3$ undergoes a splitting due to a compressive strain [49]. It is likely that due to in-plane compression, d_{x2-y2} orbitals experienced a slightly higher Coulomb potential leading to raise its energy levels, causing IP Ir L_2 white line shifts towards higher energy. Figure 5.7(a) suggests that orbital splitting in SIO on both pure and superlattice structures is accompanied by a significant occupancy difference between in-plane (d_{x2-y2}) and

out-of-plane orbitals (d_{z2-3r2}), referred as orbital polarization [175,177]. This is most likely due to a relatively larger compressive lattice strain imposed on SIO by the LSAT substrate(-2.4%) [76].

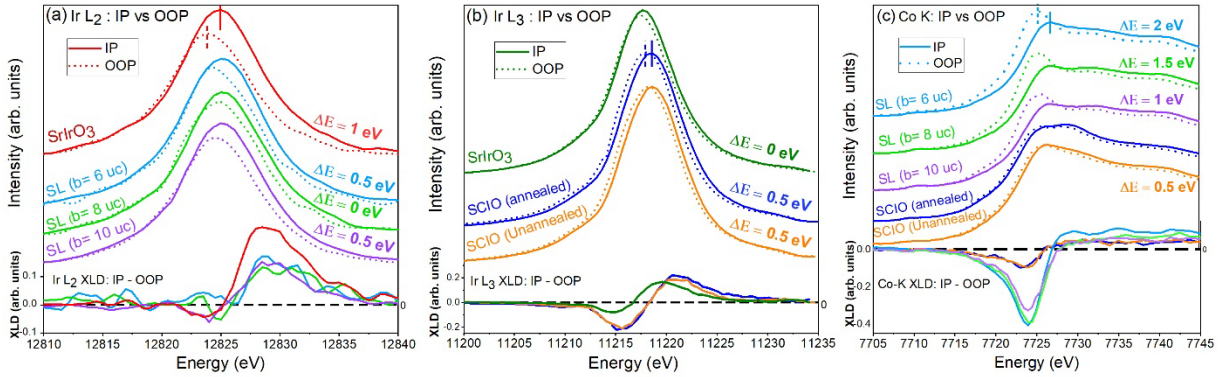

Figure 5.7: X-ray linear dichroism data for (a) Ir L_2 edge of superlattices, (b) Ir L_3 edge of double perovskites (c) Co K edge of the superlattices.

For the Sr_2CoIrO_6 films grown on $SrTiO_3$ (100) (0.05% mismatch) in Figure 5.7(c), a relatively smaller dichroism and negligible orbital polarization are observed - implying a very small deviation from uniform occupancy. To account for the IP shift of Ir L_3 XLD data, it's notes that Ir L_3 edge allows transitions to both t_{2g} and e_g orbitals, and a spin-orbit coupling splits the t_{2g} orbitals into $J_{eff}=\frac{1}{2}$ and $J_{eff}=\frac{3}{2}$ states [24,44]. Assuming the e_g orbitals nearly degenerate, it suggests Δt_{2g}= ~0.5 eV for SCIO films.

5.4.3 Angle-dependence of Co K pre-edge and hybridization

Polarization dependent pre-edge data was analyzed to investigate potential 4p-3d mixing in Co and octahedral distortions in SCO layers of the superlattices. In a perfect octahedral system, 4p-3d mixing is forbidden because of the inversion symmetry, and any pre-edge feature arises solely due to quadrupolar contribution [55,178]. Any pre-edge feature is indicative of dipolar contributions, which indicates 4p-3d orbital mixing. Therefore, the degree of 4p–3d mixing can be determined from the dipolar contribution, which is expected to follow a $\cos^2\theta$ angular dependence [118,179–181]. To analyze the polarization dependence of the pre-edge features, the peaks were fitted using Lorentzian functions and modeled the background with an error function as shown in Figure 5.8 and Figure 5.9 and Table 5.5.

For Co, the quadrupolar contribution accounts for only about 4% of the dipolar component in the pre-edge intensity [55], consequently even a moderate dipolar contribution should appear in a significantly enhanced manner.

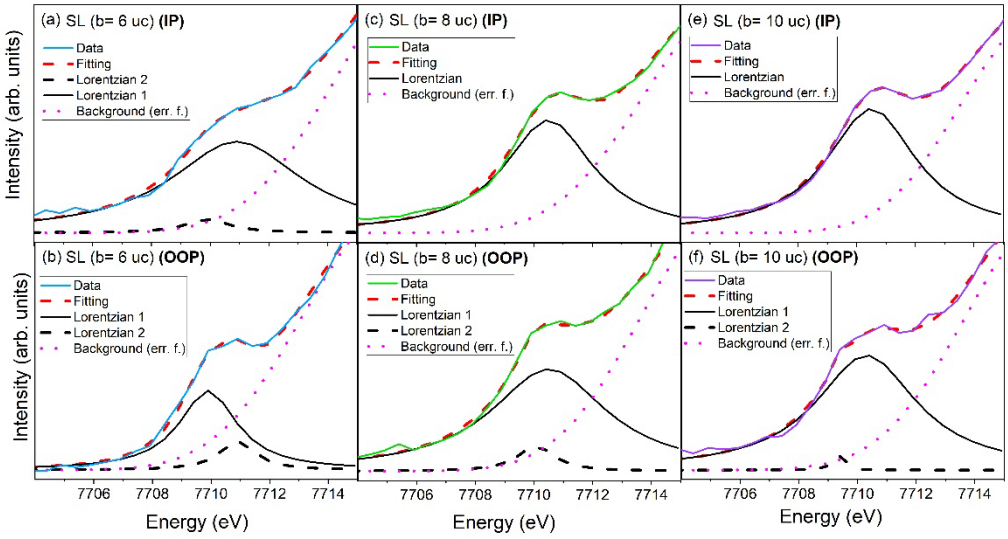

Figure 5.8: Co K Pre-edge fitting for the superlattices.

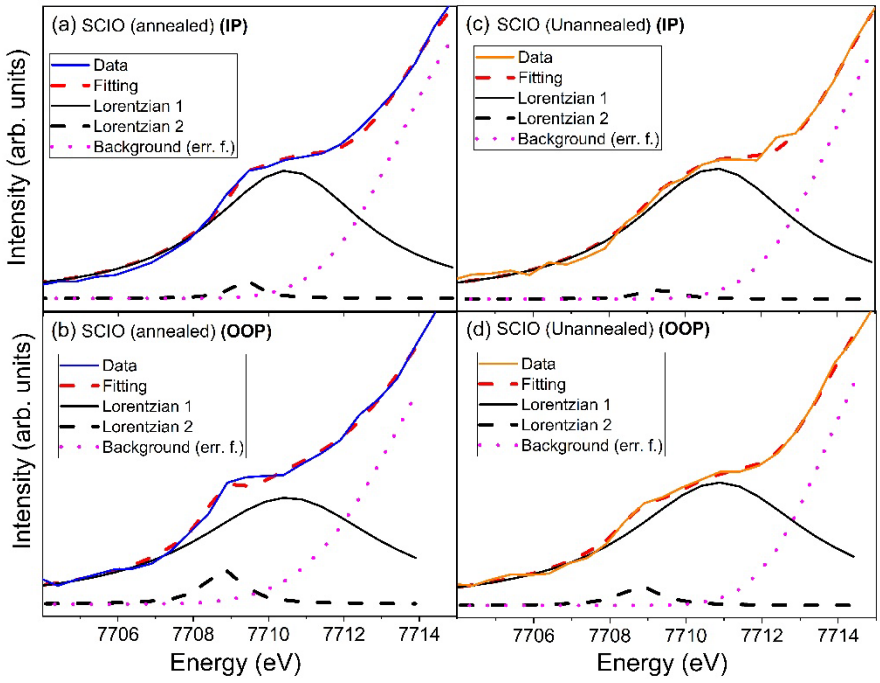

Figure 5.9: Co K Pre-edge fitting for the double perovskites.

Table 5.5: Pre-edge fitting results from Figure 5.8 and Figure 5.9

		Primary Peak			Sec. Peak	
	Center (eV)	**Intensity**	**Sigma**	**Center (eV)**	**Intensity**	**Sigma**
SL (b= 6 uc) **(IP)**	7710.90	0.41	5.44	7709.90	0.02	1.78
SL (b= 6 uc) **(OOP)**	7709.90	0.156	2.37	7710.90	0.035	1.44
SL (b= 8 uc) **(IP)**	7710.50	0.343	3.67			
SL (b= 8 uc) **(OOP)**	7710.50	0.403	4.77	7710.05	0.031	1.43
SL (b= 10 uc) **(IP)**	7710.50	0.38	3.69			
SL (b= 10 uc) **(OOP)**	7710.30	0.396	4.17	7709.30	0.005	0.329
SCIO (Annealed) **(IP)**	7710.50	0.41	4.97	7709.40	0.1	0.849
SCIO (Annealed) **(OOP)**	7710.50	0.411	5.97	7708.80	0.026	1.18
SCIO (Unannealed) **(IP)**	7710.90	0.435	5.18	7709.25	0.007	1.10
SCIO (Unannealed) **(OOP)**	7710.90	0.451	5.72	7708.80	0.015	1.22

The pre-edge spectra of films exhibit varying degrees of polarization dependence, indicating differences in local symmetry or electronic structure. For the SL-3 film (b= 10 uc), a single Lorentzian peak is sufficient to fit both the IP and OOP pre-edge spectra, with nearly identical energy positions and intensities, clearly indicating absence of a dipolar contribution (no observable $\cos^2\theta$ variation). For the SL-2 film (b= 8 uc) film, a difference of ~16% is observed between IP and OOP Lorentzian peaks at 7710.50 eV indicating a very small dipolar contribution. Additionally, a tiny peak appears at 7710.06 eV only along OOP data. This could arise due to a non-uniform spin distribution between IP/OOP directions, since a greater spectral contribution at lower energies of Co K pre-edge is associated with a higher spin state [182,183]. Following the same reasoning, the SL 1 film (b= 6 uc) exhibits a relatively higher dipolar contribution and a larger asymmetry in IP/OOP spin distributions. Given that a dipolar contribution leads to a pronounced spike in the pre-edge data in a tetragonal system, as illustrated with an example in Figure 5.10 [179,180], $SrCoO_3$ layers in the superlattice likely retained just as distorted Octahedral coordination. In both SCIO films, no notable p-d mixing is observed, while a weak spectral contribution at lower energy likely reflects a greater statistical distribution of high spin states along the OOP orbitals.

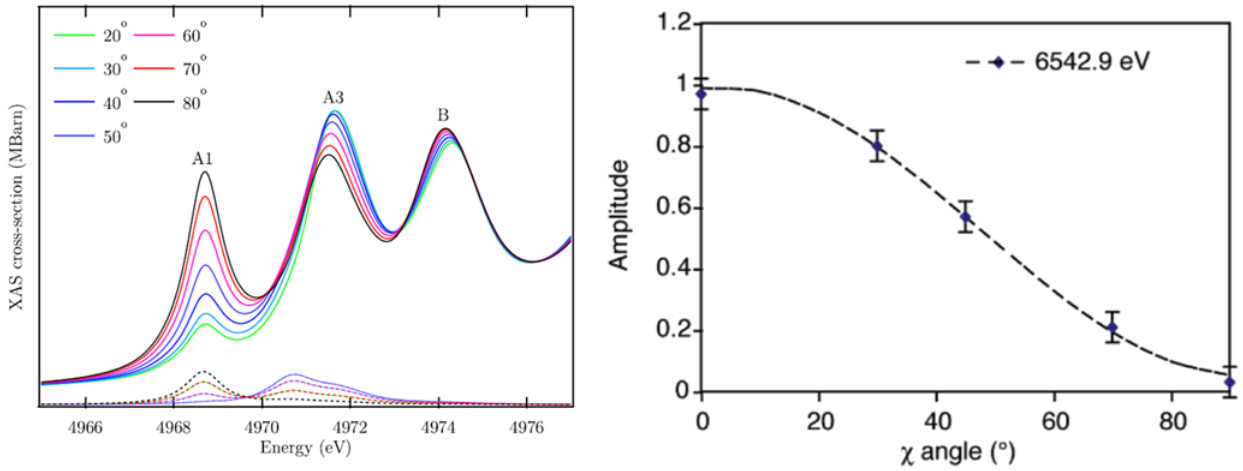

Figure 5.10: References with significant dichroic contributions to the pre-edge (a) Calculated Ti K edge spectra at the of a-TiO2 for different angles of incidence θ with the sum of dipolar and quadrupolar components (thick lines) and with quadrupolar components only. (Adapted from [180]), (b) Mn K pre-edge amplitude variation of the $[Rh(en)_3][Mn(N)(CN)_5].H2O$(Mn(V)-nitrido) compound that follows a $\cos^2\theta$ trend. (Adapted from [179])

5.4.4 Co K shoulder peaks and hybridization

The shoulder peaks, shown in Figure 5.11, further revealed a subtle degree of hybridization, with their energy positions determined using the second derivative of the spectra following [184]. In the Table 5.6, the peaks labeled S1, observed in the range 7714–7715 eV, likely indicates hybridization, although its origin remains a subject to debate. Ref. [185] suggests them as a signature of Ligand to Metal charge transfer (LMCT). Ref. [186] explains them as non-local hybridization with nearby atoms mediated by O 2p orbitals. The polarization dependence of this peak in our superlattice films aligns with [187] supporting a Co (4p)- O- Co'(3d) intersite hybridization. In contrast, this peak appears as independent of polarization directions in the double perovskites, most likely because the adjacent atoms to Co are Ir in SCIO. A relatively enhanced peak in the out-of-plane direction is observed for the SL 2 and SL 3 samples, but an opposite trend for the SL 1 sample. This suggests a directional shift and a stronger hybridization towards out-of-plane with the decreasing SIO: SCO ratio. The origin of the other shoulder peak between 7718-7719 eV observed in all films remains undetermined, however, they may imply a form of hybrid transition [184,188].

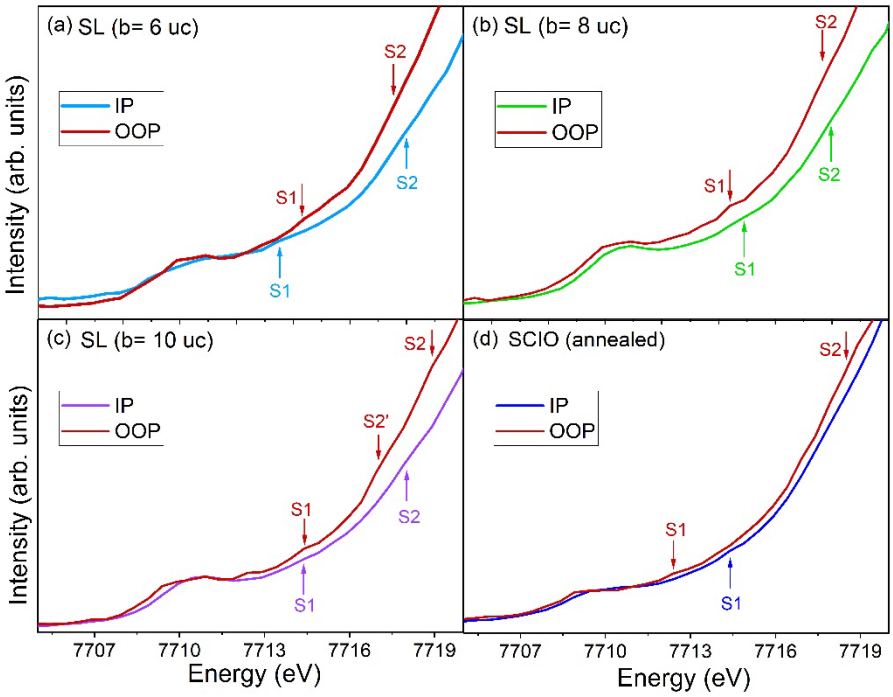

Figure 5.11: Shoulder peaks in the Co K edge data.

Table 5.6: Shoulder peak positions in Figure 5.11 (SCIO- unannealed data was not in the figure, but included in the table)

Sample	**S1 (eV)**	**S2 (eV)**
SL (b= 6 uc) **(IP)**	7714	7718
SL (b= 6 uc) **(OOP)**	7714.40	7717.50
SL (b= 8 uc) **(IP)**	7114.90	7718.90
SL (b= 8 uc) **(OOP)**	7714.40	7717.50
SL (b= 10 uc) **(IP)**	7714	7717.90
SL (b= 10 uc) **(OOP)**	7714.40	7718.90
SCIO (Annealed)- **IP**	7714.40	7717.9
SCIO (Annealed)- **OOP**	7712.40	7718.50
SCIO (Unannealed)- **IP**	7714.90	7718
SCIO (Unannealed)- **OOP**	7714	7718

5.4.5 In-plane vs out-of-plane pre-edge and octahedral distortion

The pre-edge data is examined from another point of view. Any tetragonal distortion in Co induces a splitting in the 3d e_g orbitals which should lead to a difference between IP and OOP pre-edge peak positions [58]. The tensile strain on SCO, imposed by the LSAT substrate, is expected to contract the apical bonds and elevate energy of the $d_{z2\text{-}3r2}$ orbitals. However, pre-edge fitting data in Table 5.5 doesn't support this idea. Instead, using the second derivative to identify maxima of the pre-edges (Figure 5.12), it's observed that OOP pre-edge primary peak lags by ~0.5 eV for the (SIO, SCO= (5, 3) uc) and (SIO, SCO= (6, 4) uc) samples. A similar shift in the SCIO (annealed) film, which has only 0.05% lattice mismatch with the substrate [152], suggests that a mechanism other than strain is responsible for these contradictory results. This may be attributed to the distortion of the oxygen octahedra surrounding Co. Ref. [189] proposed a similar suggestion for Ni, which exhibited an opposite response to tensile strain than expected in iridate-nickelate films. A similar trend is observed in the dichroism of Co K XANES data in Figure 5.7(c), where OOP Co K edge leads by 1-2 eV for the superlattice films, though the shift is minimal for the SCIO films.

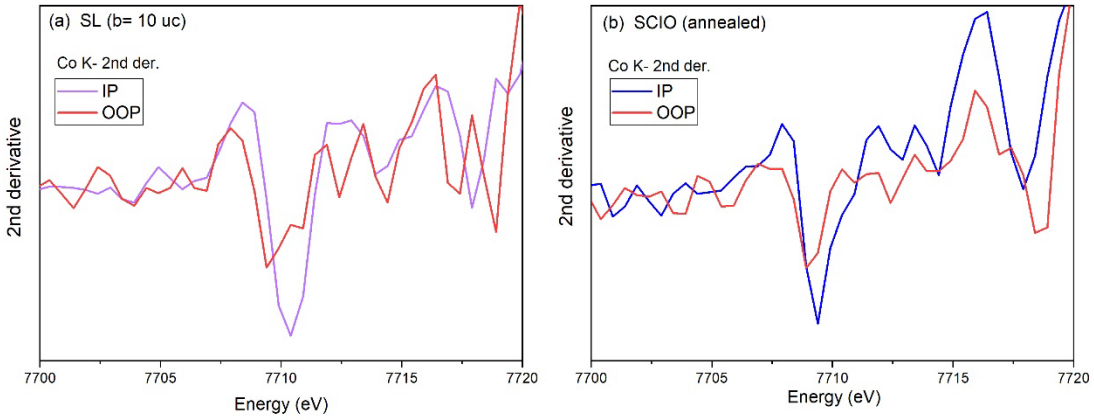

Figure 5.12: Second derivative of IP vs OOP data for selected films.

5.5 Conclusions

In conclusion, it has been confirmed that Ir donates electron to Co in the $SrIrO_3/SrCoO_3$ superlattice and Sr_2CoIrO_6 double perovskites, thus experimentally verified the prediction made by [17] and our DFT model. Using Polarization-dependent XAS on the pre-edge data of Co K edge, A sharp reduction in hybridization effect is also observed as individual layer thicknesses increase. We believe our research provides a new perspective towards understanding and improving existing theories on charge transfer in transition-metal oxides.

Chapter 6 : Spin State Transition and Electrical Transport Properties

In the chapter, as an example of the modification of electronic structure in $SrIrO_3$ due to charge transfer, electrical transport properties of the superlattices have been discussed. In the following, the spin states of Co in both pure $SrCoO_3$ film and superlattices are explored.

6.1 Electrical transport properties

The electrical transport property measurements of the films were performed in a Quantum Design Physical Property Measurement System (PPMS)- DynaCool, installed in the Department of Electrical and Computer Engineering at Auburn University. The DC four-probe method was employed in a van der Pauw geometry with indium contacts placed at the four corners of the films to serve as ohmic contacts. In the van der Pauw geometry, specific resistivity of a flat sample with four small contacts is given by [190,191]:

$$\rho = \frac{\pi d}{\ln 2}\left(\frac{R_1 + R_2}{2}\right) f\left(\frac{R_2}{R_1}\right)$$

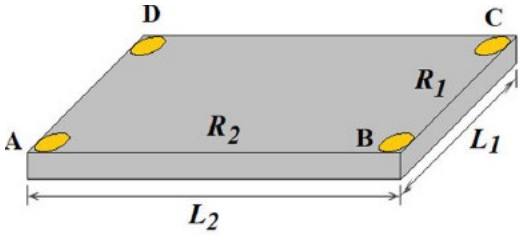

Figure 6.1: A parallelepiped sample with thickness d. (Adapted from [190])

where d is the thickness of the sample, R_1 and R_2 are the measured resistances. The term $f(R_2/R_1)$ is a geometric correction factor, determined numerically or graphically. For the samples under study, the value is assumed as 1 [192]. Another term- sheet resistance ($R_s = \rho/d$) is often used in describing transport properties [193]. The Hall co-efficient (R_H) is related to the Hall voltage (V_H) by: $R_H = (V_H d / IH)$, where I is the current parallel and H is the applied magnetic field perpendicular to the sample. $R_H > 0$ for holes and $R_H < 0$ for electrons as majority carriers [194].

For resistivity measurements, zero-field cooling and field warming (at 7 T) cycles were performed. For temperature-dependent studies, the system was allowed to stabilize for one hour after reaching each target temperature to avoid any temperature lag.

6.1.1 Transport properties of $SrCoO_3$

Since $SrCoO_3$ undergoes degradation in air, transport property measurements on $SrCoO_3$ were started within 1 hour after removing samples from the high vacuum system. An air exposure of 24 hours resulted in insulating behavior in the resistivity study, indicating that the film degrades significantly from the perovskite (P) Phase. The longitudinal resistivity data for $SrCoO_3$ film is shown along with the superlattices in Figure 6.4(a).

The transverse (Hall) resistivity can arise due to both Ordinary Hall effect (OHE) and Anomalous Hall effect (AHE). The OHE arises from the Lorentz force acting on conduction electrons, and is linear in an external applied magnetic field (H) with a positive or negative slope depending on whether majority carrier is hole or electron [195,196]. AHE, more commonly observed in ferromagnetic materials, depends on the perpendicular magnetization and the total Hall resistivity usually gets saturated at high magnetic fields [196].

In the Hall resistivity data of $SrCoO_3$, although the OHE component is not eliminated, Anomalous Hall effect (AHE) can still be clearly qualitative observed in from the shape of Figure 6.2, consistent with previous studies with perovskite $SrCoO_3$ [29,137]. The film was studied in the temperatures: 5 K, 50 K, 70 K, 150 K, 250 K, 300 K, and a clear AHE was observed only between 50 K – 150 K. At 250 K and above, it tended to become straight line with a positive slope, and at 5 K, only a noise in the data was found. No sign reversal of the AHE is observed in Figure 6.2, which is in contrast with results from [29], suggesting the mechanism of skew scattering as an origin of the AHE over the intrinsic Berry Phase. It suggests that skew scattering got suppressed at 5 K, and the intrinsic AHE was almost absent resulting in no AHE effect even at lower temperatures [29]. The contributions to the skew scattering mechanism remain undetermined.

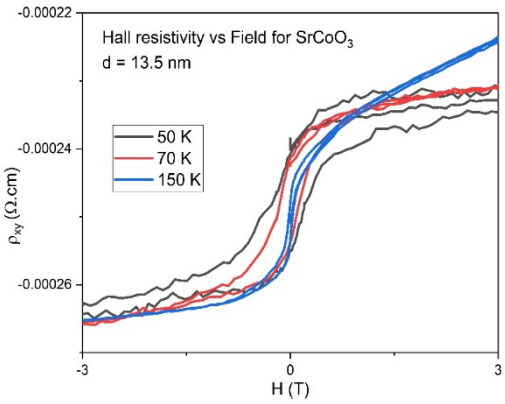

Figure 6.2: Hall resistivity data of the $SrCoO_3$ film.

6.1.2 Kondo effect and electronic reconstruction in superlattice

All the superlattice films showed metallic behavior, with an upturn below 50 K, as shown in Figure 6.4(a). This is likely due to weak localization effects, as no appreciable variation in carrier concentration ~ 9×10^{21} cm^{-3} was found. In this literature [76], the authors investigated different scattering mechanisms in $SrIrO_3$ films by fitting the temperature dependence resistivity data to the equation:

$$\rho(T) = \rho_0 + \rho_1 T^{1.4} + \rho_K \left(\frac{T_K^2}{T^2 + T_K^2} \right)^s - \rho_3 \log(T)$$

Here, ρ_0, ρ_1 and ρ_3 represent scattering from impurity, quasiparticle and weak antilocalization respectively, and ρ_K, T_K represent Kondo scattering and Kondo Temperature.

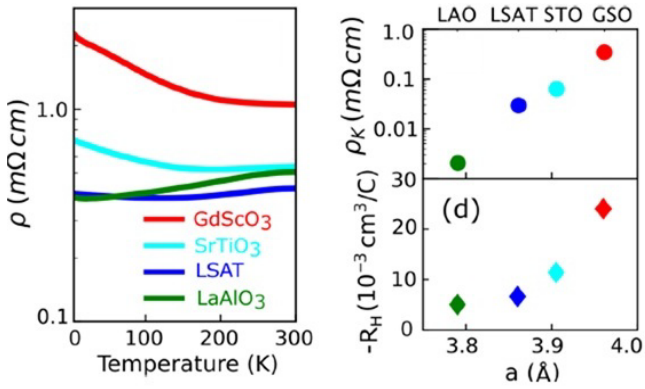

Figure 6.3: Temperature dependent resistivity (left) and Kondo scattering term (right-top) for SIO films on different substrates. (Adapted from [76])

While Kondo scattering is observed in $SrIrO_3$ films as shown in Figure 6.3 [76], the effect disappeared in the SCO/SIO superlattice films. It's likely because conduction is dominated by electrons in $SrIrO_3$, while in the superlattice SIO layers donate electrons to SCO leading to the disappearance of the Kondo effect. It underscores the role of charge transfer in suppressing this scattering effect, hence confirms a modification of the electronic structure due to charge transfer. Moreover, in the superlattice samples, a change in the majority carriers with temperature is observed. Figure 6.4(c) shows that the Hall-coefficient exhibits a negative slope at 300 K suggesting a n-type carrier, while at 45 K (and below) it exhibits a positive slope, indicating p-type majority carriers. It remained unexplored in which temperature the transition in carrier type took plane. A more detailed investigation into transport properties is expected to be carried out on the latest set of superlattices (set 3).

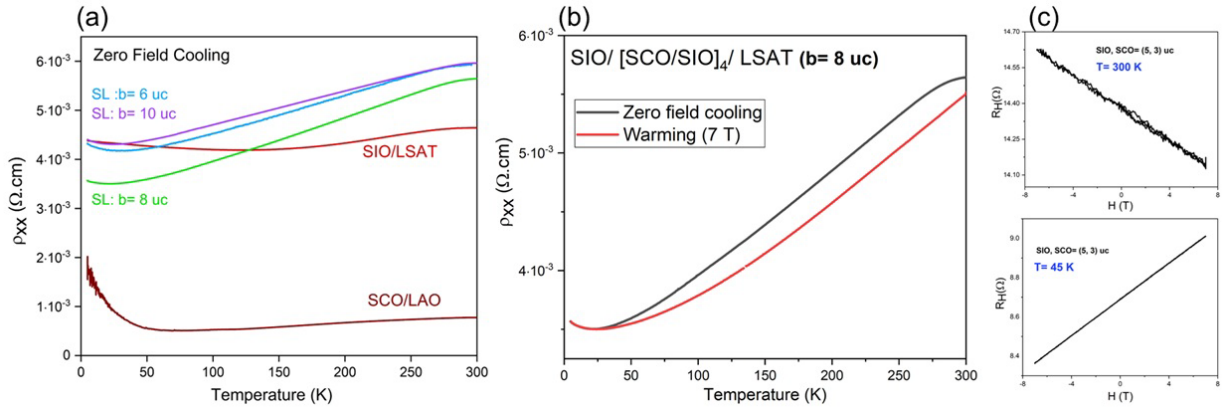

Figure 6.4: Longitudinal resistivity vs Temperature (a) Zero Field cooling (ZFC), (b) comparison of ZFC and FC for the (b= 8 uc) superlattice sample, (c) Hall co-efficient versus Field.

6.2 Branching ratio and spin state

In transition metal cobaltites, a strong competition exists between Hund's rule- which favors a high-spin (HS) state, and crystal field splitting- which stabilizes a low-spin (LS) state [197]. Consequently, the spin state of Co ions in the pristine perovskite $SrCoO_3$ (P-SCO) has been under debate, importantly, oxygen vacancies play the role of another degree of freedom [198,199]. Experimental studies have reported both low-spin [200] and intermediate spin [200] state in $SrCoO_3$. On the other hand, theoretical calculations have predicted that the most probable spin configuration should be an intermediate spin state [201,202]. However, the dynamical mean-field theory (DMFT) study with density functional theory calculations showed that the local moment in P-SCO arises predominantly from the high-spin state rather than the intermediate-spin state [203]. Furthermore, it has been further suggested that, the spin state of Co ions in P-SCO lies between the HS and IS states, depending on the amount of oxygen vacancy [199].

The spin state of a material can be determined from branching ratio of the L edge data obtained via X-ray absorption spectroscopy (XAS) or electron energy loss spectroscopy (EELS) [121,204]. The Branching ratio (BR) is defined as $I(L_3)/ [I(L_3) + I(L_2)]$, where $I(L_i)$ represents integrated intensity of the corresponding peak. As described previously, two $SrCoO_3$ films were studied with XAS Co L edge. Figure 6.5(a) shows the Co L edge spectra after background subtraction using the Shirley method and the corresponding BR value (The Tougaard

background subtraction yields a very close result). According to the literature [204], a Branching ratio value of 0.804 in SCO S2 sample indicates a high spin state for the Co^{4+} state. The sample is unique in the sense that the film was grown overnight and transported the following morning to Brookhaven National Laboratory in a vacuum-sealed bag, with measurements conducted the next day. This rapid handling likely caused least oxygen vacancy in the film and preserved the intrinsic spin state, making the result more reliable. In contrast, the SCO S1 sample was grown three days prior to SCO S2 and stored in the ultra-high vacuum (UHV) transfer line of the MBE system. This exhibited a lower BR value of 0.74 (with Shirley background subtraction) indicative of an intermediate spin state.

The superlattice samples were further studied using layer-resolved EELS in the STEM system. The Branching ratio values, summarized in Figure 6.5 with a representative sample, indicate high spin in each layer for a Co^{3+} state. This indicates that no spin state transition occurred in the superlattice films as a result of the charge transfer.

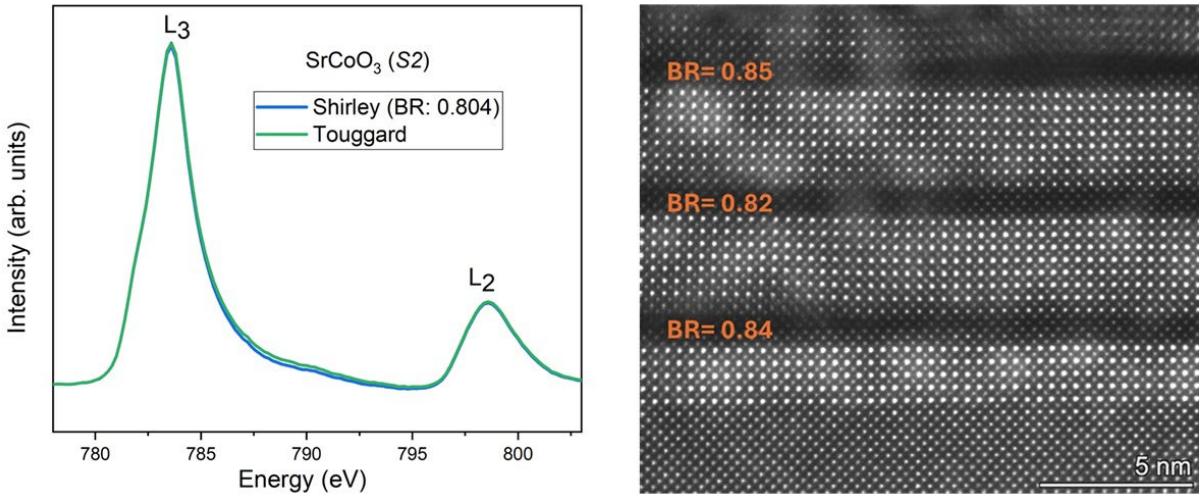

Figure 6.5: Branching ratio values of pure SCO (left) and SCO/SIO superlattice (b=10 uc) (right).

Chapter 7 : Outlook and Conclusions

Three sets of good superlattice samples were grown over the course of this research. The first set was preliminary and used to refine growth conditions of the following sets. This chapter provides data from the first and third set, along with supplementary information on the second set. In addition to cobalt and iridium-based systems, attempts were made to grow two tantalum-based perovskites- $SrTaO_3$ and $AgTaO_3$. However, these efforts did not yield satisfactory results. A brief overview of the insights gained from these films is also provided.

7.1 Superlattice- set 1

Three SIO/SCO superlattices samples were grown in the first set, one of them was on $SrTiO_3$ substrate, the other two were on LSAT. Another superlattice was grown, replacing SCO by $LaCoO_3$ (LCO) to confirm if the system was behaving properly. $LaCoO_3$ is an insulator, therefore SIO/LCO superlattice exhibited insulating behavior, as expected.

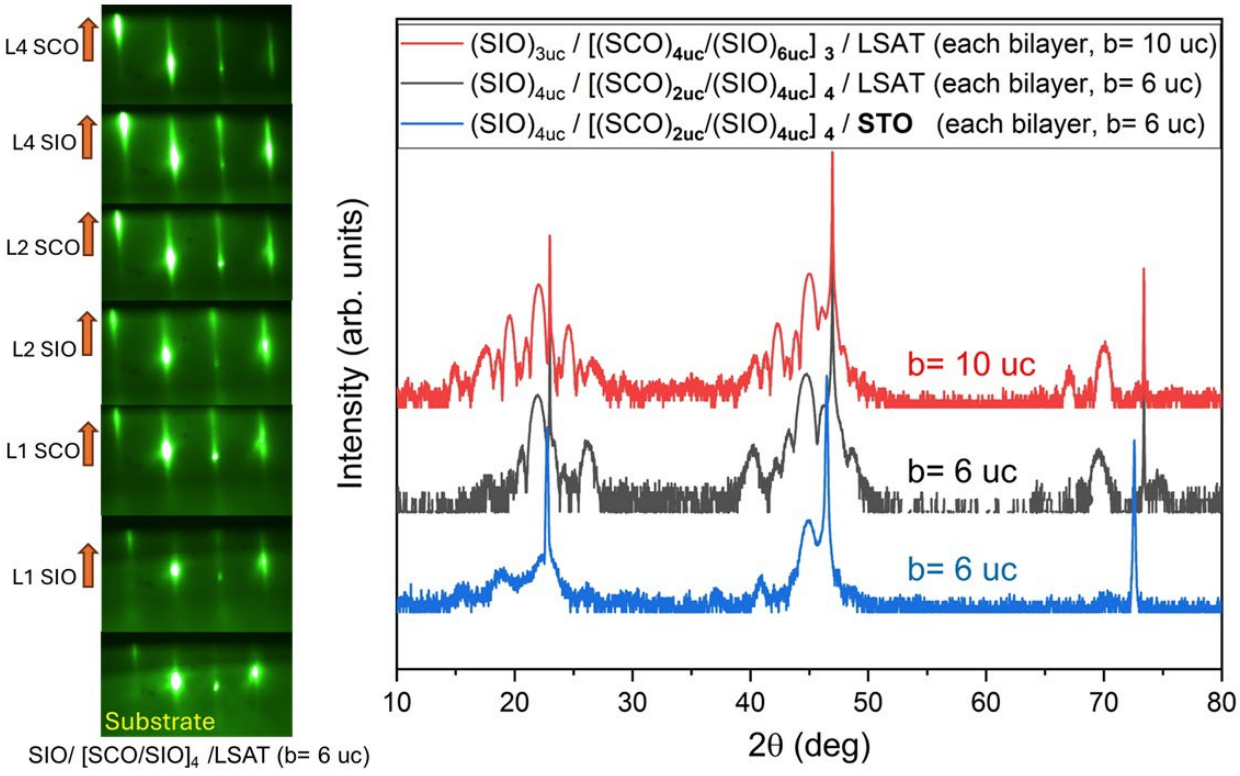

Figure 7.1: RHEED of a representative superlattice and XRD of 3 superlattices in Set 1.

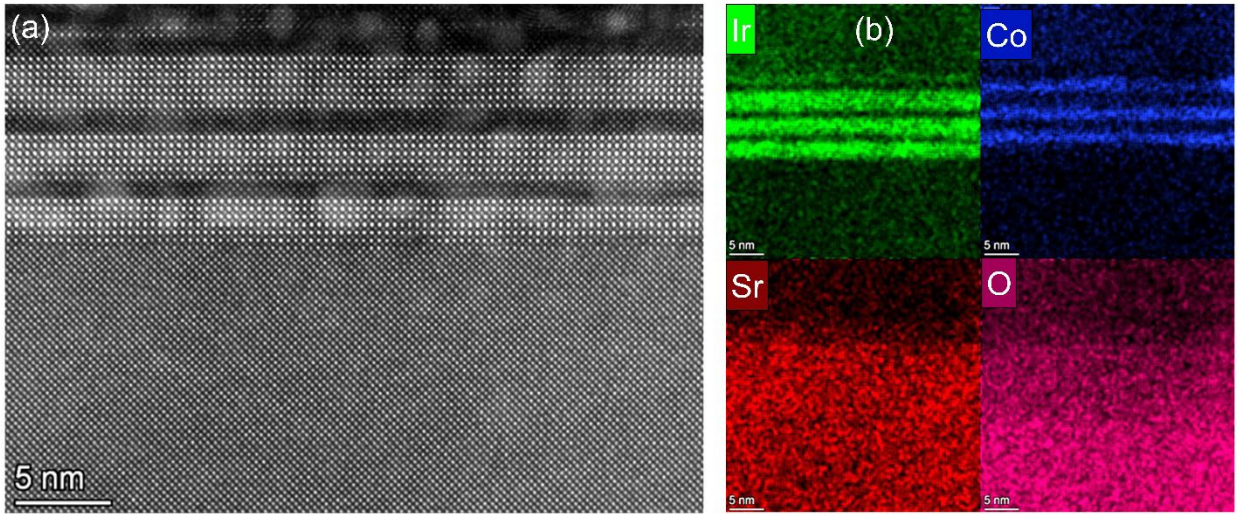

Figure 7.2: STEM and EDX from of the sample SIO/ $[SCO/SIO]_3$/ LSAT (b= 10 uc) from Superlattice set 1.

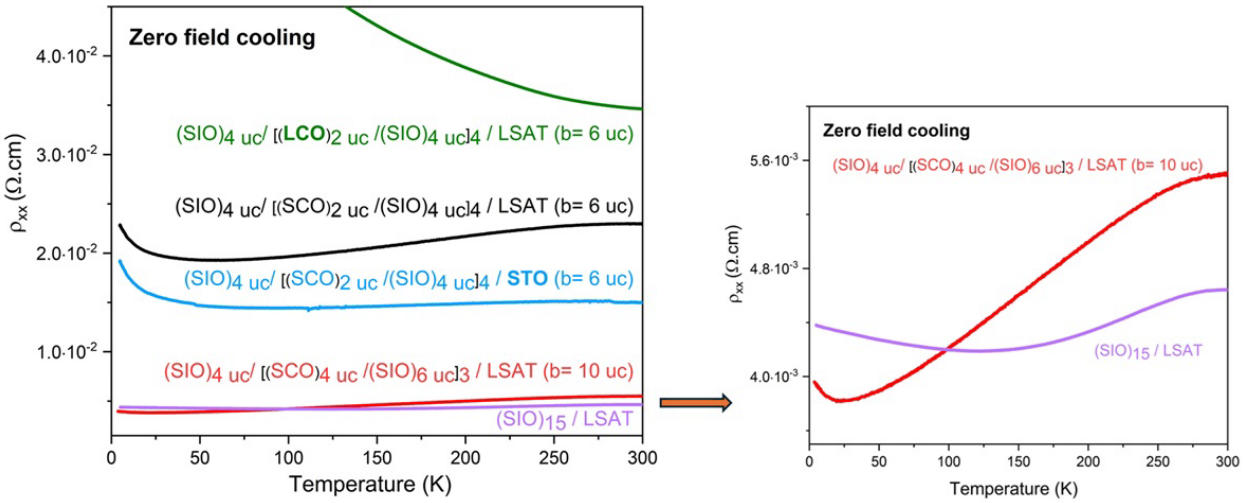

Figure 7.3: Transport data of Set 1 along with a superlattice of $LaCoO_3$-$SrIrO_3$ and pure $SrIrO_3$.

7.2 Superlattice- set 2

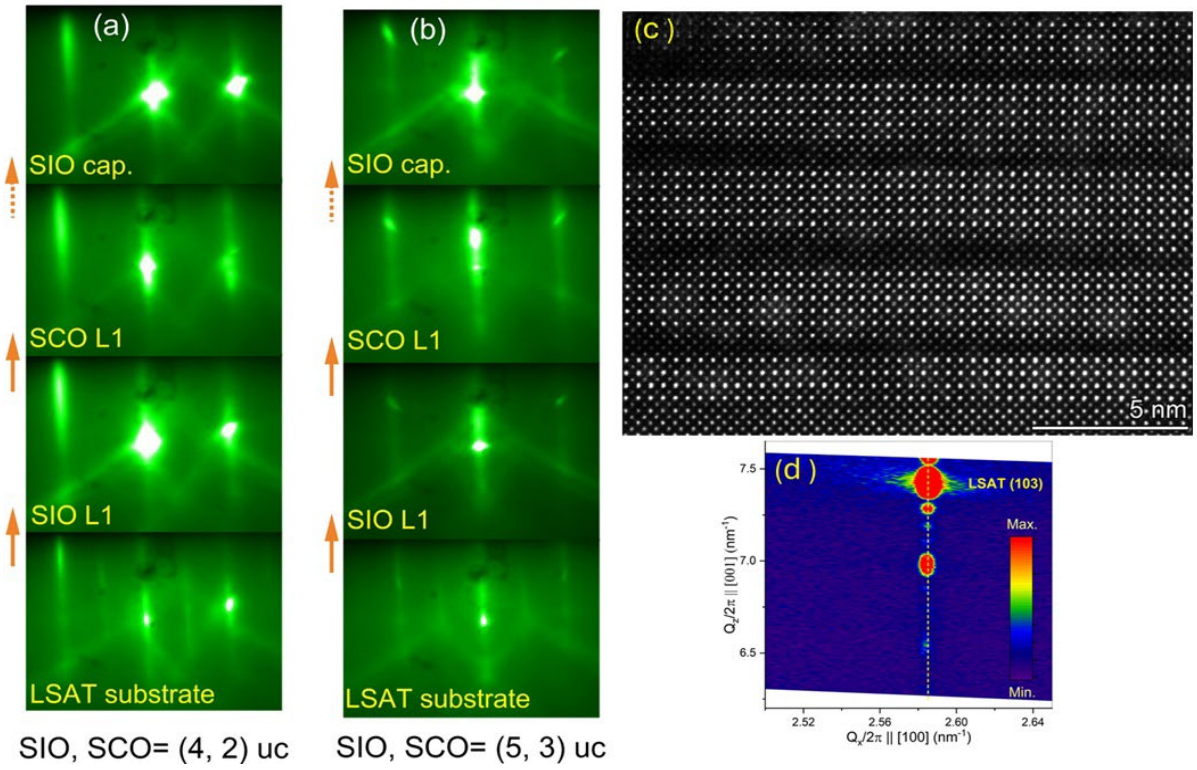

Figure 7.4: RHEED figures of (a) SL 1, (b) SL 2, (c) STEM image of SL 2, (d) RSM data of (b= 8 uc) SL of Set 2.

7.3 Superlattice- set 3

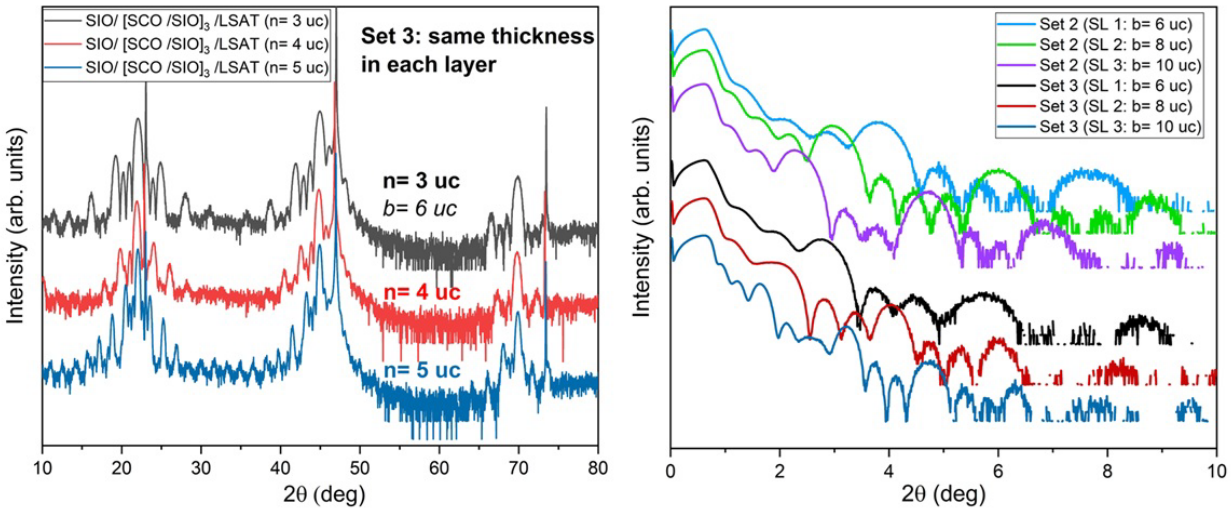

Figure 7.5: XRD (left) and XRR (right) data of 3 superlattices of Set 3.

The third set of superlattices was grown with the goal of investigating their magnetic properties. Therefore, the ferromagnetic $SrCoO_3$ layers were made relatively thicker than the previous two sets. While in the first two sets, SIO was thicker, in the third set both SIO and SCO layers were grown uniformly with the same thickness.

7.4 $SrCoO_x$

A Co K edge measurement was performed on $SrCoO_x$ in the beamline 9-BM-B,C in Advanced Photon Source, Argonne National Laboratory. The original $SrCoO_3$ films had been exposed to air for approximately 2 days, thus the Co K edge data with respect to the reference film, $LaCoO_3$ (Co^{3+}), indicates that they underwent to phases with an average oxidation state of Co^{3+}, suggesting a predominant presence of the brownmillerite (BM) phase.

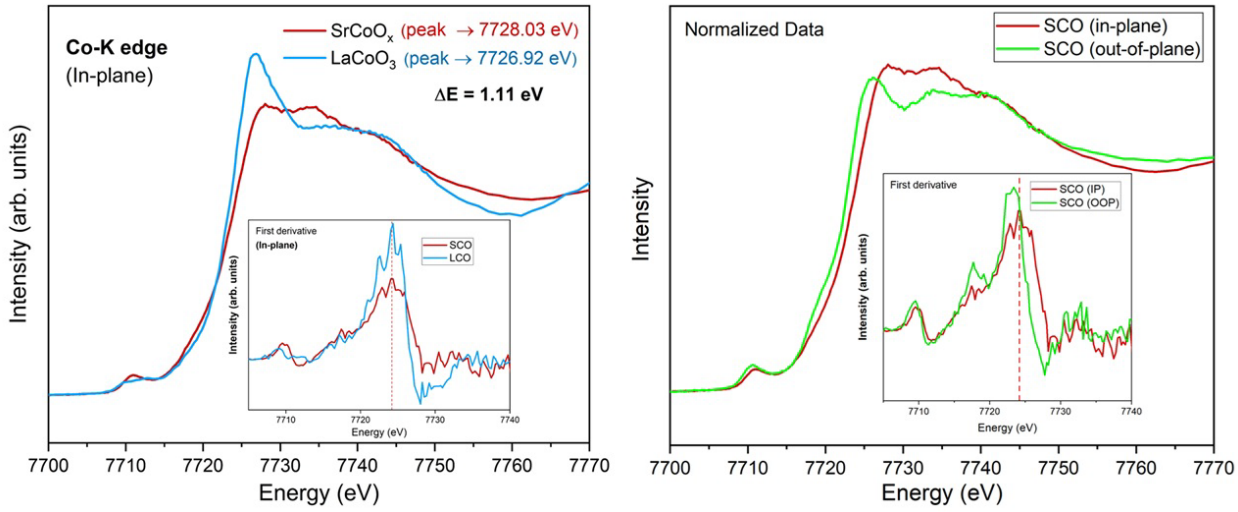

Figure 7.6: Co K edge of $SrCoO_x$ in (most likely in the BM Phase).

7.5 Outlooks on tantalum-based systems

Attempts were made to grow $SrTaO_3$ thin films, though the growth quality was not up to the expectation level. Two primary issues contributed to this. First in $SrTaO_3$, Ta holds an oxidation state of Ta^{4+}, which is very unstable and tend to oxidize to Ta^{5+}. Therefore, achieving a stable Ta^{4+} would require a growth environment of low Oxygen (Oxidizing conditions). However, our MBE system had a minimum oxygen flow rate of 0.2 sccm, which was sufficient to oxidize a large portion of Ta^{4+} state to Ta^{5+}.

The other issue was rooted in the Ta source. Elemental Ta is refractory by nature, therefore requires very high temperature (> 2400 °C) to generate sufficient vapor pressure for MBE using in conventional effusion cells [205]. To bypass this, a metal-organic source was used (like the growth of $SrIrO_3$), which required oxygen plasma to decompose the organic ligands and release tantalum. Without oxygen plasma, a very tiny amount of Ta would have deposited on the substrate. However, oxygen plasma, because of its highly oxidizing nature, would have converted Ta^{4+} to Ta^{5+} readily. For most of the $SrTaO_3$ growths, oxygen plasma was turned off during growth which resulted in very low Ta deposition. Moreover, such a tiny amount, when exposed to 0.2 sccm of Oxygen, converted to Ta^{5+} had there any Ta^{4+}. To protect the $SrTaO_3$ layer and potentially stabilize the structure, attempts were made to synthesize $AgTaO_3$ as a capping layer. But, Ag was found to be difficult to oxidize within the operating pressure of MBE. Thus, growing good quality Ta-based perovskites remained challenging.

While MBE has inherent limitations, it offers flexibility for continuous innovation and system upgrades. For example, hybrid MBE (hMBE) successfully addressed the challenges associated with the refractory nature of iridium. Similarly, a modified setup can accommodate issues with Ta based perovskites growth in future.

7.6 Conclusions and prospects

In conclusion, it has been experimentally and theoretically confirmed that Ir donates electrons to Co in the $SrIrO_3/SrCoO_3$ superlattices and Sr_2CoIrO_6 double perovskites, thereby confirming the direction of charge transfer predicted for similar perovskite superlattices. An extension of the theoretical model is that charge transfer does not occur directly from Ir to Co but is mediated through the intermittent oxygen sublattice.

This research holds significant potential for various technological applications. One key example is its relevance to overcoming current challenges on transistors and chips. Microchips and transistors are the brain of all modern technological tools: modern electronics (computers/smartphones/modern cars), household appliances (microwaves, washing machines, and refrigerators), medical devices (MRI, CT scanner), industrial robotics (and automation), artificial intelligence, quantum computing and many others.

Usually, millions of transistors are packed into a single microchip. The smaller the transistors can be produced, the more of them can be packed in a chip, and the more powerful device systems become. After continuously reducing the size of those transistors (Murphy's law), currently we are on the 2 nanometers scale, and it's the limit below which silicon leaks current, and unable to function effectively anymore. At this point, to continue the current technological advancements, we require another breakthrough and must find alternative material to replace silicon. The most potential pathway that scientists are attempting to achieve towards this goal is research on two-dimensional materials (especially transition metals) [206,207]. Fashioning these compounds into only three-atom-thickness can help, in principle, make smaller and more energy efficient transistors, while avoiding the performance problems of silicon. This dissertation provides evidence of successful growths of excellent quality ultra-thin films which are of even less than 1 nanometer. Particularly, layers of as low as only 2 uc (0.8 nanometers) have been synthesized, where individual layers can still exhibit their inherent properties.

From an economic point of view, the US government enacted the CHIPS and Science Act in August 2022 with roughly $280 billion in funding and expected to manufacture nearly 30 percent of the world's leading-edge chips by 2032 [208,209]. In addition, an investment of $500 billion in Artificial Intelligence infrastructure was announced in January 2025 [210]. The foundation of artificial intelligence is driven by having specially advanced chips (called GPU) to operate it.

Even with so much investments, it seems there is only one way to circumvent the current barrier-going beyond Silicon. An invention of something which can work efficiently at even smaller size than silicon will eventually make silicon Chips outdated. That will be a breakthrough. Ultrathin films of complex oxides present a promising alternative to silicon in next-generation transistors, and this dissertation demonstrates their effectiveness in sub-nanometer scale. Further in-depth research on this is worthy and can provide more valuable insights.

From a different point of view, in investigating charge transfer, it has been demonstrated that charge transfer can act as a viable mechanism for stabilizing metastable phases like perovskite $SrCoO_3$ (P-SCO). This provides a remarkable opportunity to address a major problem among ultra-thin film researchers- preserving the quality of a certain thin film over longer periods.

Often thin films are grown at pressures hundreds of thousands of times less than atmospheric pressure, but once the films are brought to atmosphere, their quality can't sustain longer. But for

real-life applications, we must find a way to have their inherent properties persisted in earth's atmosphere. This problem is even severe for certain materials that perform under harsh conditions. For example, satellites run on solar cells for their energy, and these cells must withstand significantly higher levels of potentially damaging particle radiation and greater fluctuations in temperature in the higher atmospheric spheres and outer space.

To note, to act as a protective layer, an appropriate coating not only protects from damage, at the same time, it doesn't change inherent properties of the material it's protecting. Determining the appropriate coating is a challenging task. With current established theories, it's possible to predict potential appropriate materials of only a narrow class of semiconducting materials. Incorporating a broad spectrum of materials requires verification of existing theories. The experimental verification process is additionally important because they can provide important feedback missing in existing works. This work can certainly provide a ground in this feedback mechanism and help bridge the current gaps in predicting appropriate protective layers in a broader manner.

References:

[1] G. Granozzi and S. Agnoli, *Ultrathin Oxide Films*, in *Surface and Interface Science* (John Wiley & Sons, Ltd, 2013), pp. 585–640.

[2] H. Brune, *Epitaxial Growth of Thin Films*, in *Surface and Interface Science* (John Wiley & Sons, Ltd, 2013), pp. 421–492.

[3] J. Heber, Enter the oxides, Nat. Publ. Group **459**, (2009).

[4] D. G. Schlom, L. Chen, X. Pan, A. Schmehl, and M. A. Zurbuchen, A Thin Film Approach to Engineering Functionality into Oxides, J. Am. Ceram. Soc. **91**, 2429 (2008).

[5] C. Kittel, *Introduction to Solid State Physics*, 8th ed (Wiley, Hoboken, NJ, 2005).

[6] P. Zubko, S. Gariglio, M. Gabay, P. Ghosez, and J.-M. Triscone, Interface Physics in Complex Oxide Heterostructures, Annu. Rev. Condens. Matter Phys. **2**, 141 (2011).

[7] H.-U. Habermeier, Thin films of perovskite-type complex oxides, Mater. Today **10**, 34 (2007).

[8] T. Ishihara, *Perovskite Oxide for Solid Oxide Fuel Cells* (Springer-Verlag US, Boston, MA, 2009).

[9] Z. Zeng, F. Calle-Vallejo, M. B. Mogensen, and J. Rossmeisl, Generalized trends in the formation energies of perovskite oxides, Phys. Chem. Chem. Phys. **15**, 7526 (2013).

[10] A. Kumar, A. Kumar, and V. Krishnan, Perovskite Oxide Based Materials for Energy and Environment-Oriented Photocatalysis, ACS Catal. **10**, 10253 (2020).

[11] A. Ohtomo and H. Y. Hwang, A high-mobility electron gas at the LaAlO3/SrTiO3 heterointerface, Nature **427**, 423 (2004).

[12] K. S. Takahashi, M. Kawasaki, and Y. Tokura, Interface ferromagnetism in oxide superlattices of CaMnO3/CaRuO3, Appl. Phys. Lett. **79**, 1324 (2001).

[13] A. Bhattacharya, S. J. May, S. G. E. Te Velthuis, M. Warusawithana, X. Zhai, B. Jiang, J.-M. Zuo, M. R. Fitzsimmons, S. D. Bader, and J. N. Eckstein, Metal-Insulator Transition and Its Relation to Magnetic Structure in (LaMnO 3) 2 n / (SrMnO 3) n Superlattices, Phys. Rev. Lett. **100**, 257203 (2008).

[14] J. Nichols et al., Emerging magnetism and anomalous Hall effect in iridate–manganite heterostructures, Nat. Commun. **7**, 12721 (2016).

[15] A. Gozar, G. Logvenov, L. F. Kourkoutis, A. T. Bollinger, L. A. Giannuzzi, D. A. Muller, and I. Bozovic, High-temperature interface superconductivity between metallic and insulating copper oxides, Nature **455**, 782 (2008).

[16] H. Chen and A. Millis, Charge transfer driven emergent phenomena in oxide heterostructures, J. Phys. Condens. Matter **29**, 243001 (2017).

[17] Z. Zhong and P. Hansmann, Band Alignment and Charge Transfer in Complex Oxide Interfaces, Phys. Rev. X **7**, 011023 (2017).

[18] W. Mönch, *From the Schottky–Mott Rule to Interface-Induced Gap States*, in *Electronic Structure of Semiconductor Interfaces* (Springer Nature Switzerland, Cham, 2024), pp. 37–60.

[19] Z. Zhong and P. Hansmann, Tuning the work function in transition metal oxides and their heterostructures, Phys. Rev. B **93**, 235116 (2016).

[20] J. Geessinck, Charge Transfer at the Interface between Complex Oxide Thin Films, PhD, University of Twente, 2020.

[21] J. Wu, M. Zöllner, S. Esser, V. Begum, G. Prinz, A. Lorke, P. Gegenwart, and R. Pentcheva, Electronic reconstruction and charge transfer in strained Sr 2 CoIrO 6 double perovskite, Phys. Rev. B **104**, 205126 (2021).
[22] T. Takami, *Functional Cobalt Oxides: Fundamentals, Properties, and Applications* (Pan Stanford Publishing, Singapore, 2014).
[23] Y. F. Nie et al., Interplay of Spin-Orbit Interactions, Dimensionality, and Octahedral Rotations in Semimetallic SrIrO 3, Phys. Rev. Lett. **114**, 016401 (2015).
[24] M. A. Zeb and H.-Y. Kee, Interplay between spin-orbit coupling and Hubbard interaction in SrIrO 3 and related Pbnm perovskite oxides, Phys. Rev. B **86**, 085149 (2012).
[25] P. Bezdicka, A. Wattiaux, J. C. Grenier, M. Pouchard, and P. Hagenmuller, Preparation and characterization of Fully stoichiometric $SrCoO_3$ by electrochemical oxidation, Z. Für Anorg. Allg. Chem. **619**, 7 (1993).
[26] S. Balamurugan, K. Yamaura, M. Arai, and E. Takayama-Muromachi, Charge transport and ferromagnetic critical behavior of the correlated 3 d perovskite Sr 1 − x Ce x CoO 3, Phys. Rev. B **76**, 014414 (2007).
[27] Y. Long, Y. Kaneko, S. Ishiwata, Y. Taguchi, and Y. Tokura, Synthesis of cubic $SrCoO_3$ single crystal and its anisotropic magnetic and transport properties, J. Phys. Condens. Matter **23**, 245601 (2011).
[28] P. Schöffmann, Stoichiometric Control and Magnetoelectric Coupling in Artificial Multiferroic Heterostructures, RWTH Aachen University, 2021.
[29] D. Zhang, Y. Wang, N. Lu, X. Sui, Y. Xu, P. Yu, and Q.-K. Xue, Origin of the anomalous Hall effect in SrCoO 3 thin films, Phys. Rev. B **100**, 060403 (2019).
[30] N. Lu et al., Electric-field control of tri-state phase transformation with a selective dual-ion switch, Nature **546**, 124 (2017).
[31] J. H. Lee and K. M. Rabe, Coupled Magnetic-Ferroelectric Metal-Insulator Transition in Epitaxially StrainedSrCoO3from First Principles, Phys. Rev. Lett. **107**, (2011).
[32] Y. Wang et al., Robust Ferromagnetism in Highly Strained SrCoO 3 Thin Films, Phys. Rev. X **10**, 021030 (2020).
[33] S. J. Callori, S. Hu, J. Bertinshaw, Z. J. Yue, S. Danilkin, X. L. Wang, V. Nagarajan, F. Klose, J. Seidel, and C. Ulrich, Strain-induced magnetic phase transition in SrCoO 3 − δ thin films, Phys. Rev. B **91**, 140405 (2015).
[34] G. Cao and P. Schlottmann, The challenge of spin–orbit-tuned ground states in iridates: a key issues review, Rep. Prog. Phys. **81**, 042502 (2018).
[35] J.-W. Kim, Y. Choi, S. H. Chun, D. Haskel, D. Yi, R. Ramesh, J. Liu, and P. J. Ryan, Controlling entangled spin-orbit coupling of 5 d states with interfacial heterostructure engineering, Phys. Rev. B **97**, 094426 (2018).
[36] G. Rimal, T. Tasnim, G. Calderon Ortiz, G. E. Sterbinsky, J. Hwang, and R. B. Comes, Strain-dependent insulating state and Kondo effect in epitaxial SrIrO 3 films, Phys. Rev. Mater. **8**, L071201 (2024).
[37] S. Okamoto, J. Nichols, C. Sohn, S. Y. Kim, T. W. Noh, and H. N. Lee, Charge Transfer in Iridate-Manganite Superlattices, Nano Lett. **17**, 2126 (2017).
[38] F. Wang and T. Senthil, Twisted Hubbard Model forSr2IrO4: Magnetism and Possible High Temperature Superconductivity, Phys. Rev. Lett. **106**, (2011).
[39] B. J. Kim et al., Novel J eff = 1 / 2 Mott State Induced by Relativistic Spin-Orbit Coupling in Sr 2 IrO 4, Phys. Rev. Lett. **101**, 076402 (2008).

[40] W. Zhang, Spin Orbital Coupling in 5d Transition Metal Oxides and Topological Flat Bands, The Ohio State University, 2021.
[41] R. Gu et al., Superorders and terahertz acoustic modes in multiferroic BiFeO3/LaFeO3 superlattices, Appl. Phys. Rev. **11**, (2024).
[42] R. Tsu, Applying the insight into superlattices and quantum wells for nanostructures: Low-dimensional structures and devices, Microelectron. J. **38**, 959 (2007).
[43] H. Böttner, G. Chen, and R. Venkatasubramanian, Aspects of Thin-Film Superlattice Thermoelectric Materials, Devices, and Applications, MRS Bull. **31**, 211 (2006).
[44] B. J. Kim et al., Novel J eff = 1 / 2 Mott State Induced by Relativistic Spin-Orbit Coupling in Sr 2 IrO 4, Phys. Rev. Lett. **101**, 076402 (2008).
[45] S. J. Moon et al., Dimensionality-Controlled Insulator-Metal Transition and Correlated Metallic State in 5 d Transition Metal Oxides Sr n + 1 Ir n O 3 n + 1 (n = 1 , 2, and ∞), Phys. Rev. Lett. **101**, 226402 (2008).
[46] J. W. Kim, Y. Choi, J. Kim, J. F. Mitchell, G. Jackeli, M. Daghofer, J. Van Den Brink, G. Khaliullin, and B. J. Kim, Dimensionality Driven Spin-Flop Transition in Layered Iridates, Phys. Rev. Lett. **109**, 037204 (2012).
[47] A. De La Torre et al., Collapse of the Mott Gap and Emergence of a Nodal Liquid in Lightly Doped Sr 2 IrO 4, Phys. Rev. Lett. **115**, 176402 (2015).
[48] F. Wang and T. Senthil, Twisted Hubbard Model for Sr 2 IrO 4 : Magnetism and Possible High Temperature Superconductivity, Phys. Rev. Lett. **106**, 136402 (2011).
[49] J. Liu et al., *Tuning the Electronic Properties of J_eff=1/2 Correlated Semimetal in Epitaxial Perovskite SrIrO3*, arXiv:1305.1732.
[50] D. Yi et al., Atomic-scale control of magnetic anisotropy via novel spin–orbit coupling effect in La 2/3 Sr 1/3 MnO 3 /SrIrO 3 superlattices, Proc. Natl. Acad. Sci. **113**, 6397 (2016).
[51] D. Yi et al., Tuning Perpendicular Magnetic Anisotropy by Oxygen Octahedral Rotations in (La 1 − x Sr x MnO 3) / (SrIrO 3) Superlattices, Phys. Rev. Lett. **119**, 077201 (2017).
[52] J. D. Hoffman et al., Oscillatory Noncollinear Magnetism Induced by Interfacial Charge Transfer in Superlattices Composed of Metallic Oxides, Phys. Rev. X **6**, 041038 (2016).
[53] S. Esser et al., Strain-induced changes of the electronic properties of B -site ordered double-perovskite Sr 2 CoIrO 6 thin films, Phys. Rev. B **97**, 205121 (2018).
[54] S. Agrestini et al., Nature of the magnetism of iridium in the double perovskite Sr 2 CoIrO 6, Phys. Rev. B **100**, 014443 (2019).
[55] G. N. George and I. J. Pickering, *X-Ray Absorption Spectroscopy* (De Gruyter, Berlin Boston, 2025).
[56] M. S. Dresselhaus, G. Dresselhaus, and A. Jorio, *Group Theory: Application to the Physics of Condensed Matter* (Springer-Verlag, Berlin, 2008).
[57] *Crystal Field Theory*, https://en.wikipedia.org/wiki/Crystal_field_theory.
[58] X. Cheng, Multiplet computation methods for core level X-ray spectroscopy of transition metal and rare earth elements, (2023).
[59] *Introduction to Inorganic Chemistry/ - Wikibooks, Open Books for an Open World*, https://en.wikibooks.org/wiki/Introduction_to_Inorganic_Chemistry/.
[60] R. Carter, *Transition Metal Complexes - Crystal Field Theory*, https://alpha.chem.umb.edu/chemistry/ch370/.
[61] K. V. Shanavas, Z. S. Popović, and S. Satpathy, Theoretical model for Rashba spin-orbit interaction indelectrons, Phys. Rev. B **90**, (2014).

[62] N. Zettili, *Quantum Mechanics: Concepts and Applications*, 2nd ed (Wiley, Chichester, U.K, 2009).
[63] F. Herman, S. Skillman, and J. Arents, Atomic Structure Calculations, J. Electrochem. Soc. **111**, 87C (1964).
[64] J. Kondo, Resistance Minimum in Dilute Magnetic Alloys, Prog. Theor. Phys. **32**, 37 (1964).
[65] L. Kouwenhoven and L. Glazman, Revival of the Kondo effect, Phys. World **14**, 33 (2001).
[66] T. Child, M. Cross, A. Tully, and M. Werner, An Introduction to the Kondo Effect, (2018).
[67] *Handbook of Sputtering Technology* (Elsevier, 2012).
[68] M. A. Herman and H. Sitter, *Molecular Beam Epitaxy: Fundamentals and Current Status*, 2., nd ed. 1996 (Springer Berlin, Berlin, 2013).
[69] *Epitaxial Growth of Thin Films*, in *Surface and Interface Science* (Wiley-VCH Verlag GmbH & Co. KGaA, Weinheim, Germany, 2014), pp. 421–492.
[70] S. Askraba, A New Vibrational Technique for Measurement of Stress Variations in Thin Films, PhD thesis, Victoria University, 1999.
[71] J. Palisaitis and R. Vasiliauskas, *Epitaxial Growth of Thin Films*, (unpublished).
[72] D. G. Schlom, L. Chen, X. Pan, A. Schmehl, and M. A. Zurbuchen, A Thin Film Approach to Engineering Functionality into Oxides, J. Am. Ceram. Soc. **91**, 2429 (2008).
[73] D. Schlom, *MBE+ARPES: Customizing Quantum Materials with Atomic Layer Precision and Measuring Their Electronic Structure*, https://www.paradim.org/2022_CU_SS.
[74] R. Paudel, Band Engineering of Perovskite Ferrite Epitaxial Thin Films for OER Catalysis, PhD thesis, Auburn University, 2022.
[75] S. Thapa, S. R. Provence, P. T. Gemperline, B. E. Matthews, S. R. Spurgeon, S. L. Battles, S. M. Heald, M. A. Kuroda, and R. B. Comes, Surface stability of SrNbO3+δ grown by hybrid molecular beam epitaxy, APL Mater. **10**, 091112 (2022).
[76] G. Rimal, T. Tasnim, G. Calderon Ortiz, G. E. Sterbinsky, J. Hwang, and R. B. Comes, Strain-dependent insulating state and Kondo effect in epitaxial SrIrO 3 films, Phys. Rev. Mater. **8**, L071201 (2024).
[77] B. Jalan, R. Engel-Herbert, N. J. Wright, and S. Stemmer, Growth of high-quality SrTiO3 films using a hybrid molecular beam epitaxy approach, J. Vac. Sci. Technol. Vac. Surf. Films **27**, 461 (2009).
[78] V. M. Mecea, From Quartz Crystal Microbalance to Fundamental Principles of Mass Measurements, Anal. Lett. **38**, 753 (2005).
[79] Quartz Crystal Microbalance (QCM), n.d.
[80] SYLTHERM^{TM} XLT Heat Transfer Fluid, n.d.
[81] M. A. Herman and H. Sitter, *Molecular Beam Epitaxy: Fundamentals and Current Status*, 2nd, rev.updated ed ed. (Springer, Berlin ; New York, 1996).
[82] D. G. Schlom, L. Chen, X. Pan, A. Schmehl, and M. A. Zurbuchen, A Thin Film Approach to Engineering Functionality into Oxides, J. Am. Ceram. Soc. **91**, 2429 (2008).
[83] M. H. Yang and C. P. Flynn, Growth of alkali halides from molecular beams: Global growth characteristics, Phys. Rev. Lett. **62**, 2476 (1989).
[84] S.-L. Shang, S. Lin, M. C. Gao, D. G. Schlom, and Z.-K. Liu, Ellingham diagrams of binary oxides, APL Mater. **12**, (2024).
[85] The Interactive Ellingham Diagram Tool, (n.d.).

[86] M. A. Herman, Physical problems concerning effusion processes of semiconductors in molecular beam epitaxy, Vacuum **32**, 555 (1982).
[87] *The Technology and Physics of Molecular Beam Epitaxy* (n.d.).
[88] B. Lewis and J. C. Anderson, *Nucleation and Growth of Thin Films*, U.S. ed (Academic Press, New York, 1978).
[89] S. M. Baumann, *RBS*, in *Encyclopedia of Materials Characterization* (Elsevier, 1992), pp. 476–487.
[90] H. R. Verma, editor , *Rutherford Backscattering Spectroscopy*, in *Atomic and Nuclear Analytical Methods: XRF, Mössbauer, XPS, NAA and B63Ion-Beam Spectroscopic Techniques* (Springer, Berlin, Heidelberg, 2007), pp. 91–141.
[91] M. Mayer, *Rutherford Backscattering Spectrometry (RBS)*, in *Workshop on Nuclear Data for Science and Technology: Materials Analysis*, Vol. 34 (2003).
[92] Sylvan. Rubin, T. O. Passell, and L. E. Bailey, Chemical Analysis of Surfaces by Nuclear Methods, Anal. Chem. **29**, 736 (1957).
[93] M. Mayer, SIMNRA, a simulation program for the analysis of NRA, RBS and ERDA, AIP Conf. Proc. **475**, 541 (1999).
[94] A. Ichimiya and P. I. Cohen, *Reflection High-Energy Electron Diffraction* (Cambridge University Press, Cambridge, 2004).
[95] S. Hasegawa, *Reflection High-Energy Electron Diffraction*, in *Characterization of Materials*, edited by E. N. Kaufmann, 1st ed. (Wiley, 2012), pp. 1–14.
[96] J. H. Haeni, C. D. Theis, and D. G. Schlom, RHEED Intensity Oscillations for the Stoichiometric Growth of SrTiO3 Thin Films by Reactive Molecular Beam Epitaxy, J. Electroceramics **4**, 385 (2000).
[97] N. Derriche, S. Godin, R. Greenwood, A. Mercado, and A. N. Warner, Reflection High-Energy Electron Diffraction, (2019).
[98] C. Hammond, *The Basics of Crystallography and Diffraction*, 3. ed., reprinted with corr (Oxford Univ. Press [u.a.], Oxford, 2012).
[99] G.-C. Wang and T.-M. Lu, *RHEED Transmission Mode and Pole Figures: Thin Film and Nanostructure Texture Analysis* (Springer, New York, NY, 2014).
[100] X. Xu, *Reflection High Energy Electron Diffraction (RHEED) Basics*, in (2017).
[101] *Applied RHEED*, Vol. 154 (Springer Berlin Heidelberg, Berlin, Heidelberg, 1999).
[102] G. F. Harrington and J. Santiso, Back-to-Basics tutorial: X-ray diffraction of thin films, J. Electroceramics **47**, 141 (2021).
[103] S. Speakman, *Introduction to High Resolution X-Ray Diffraction of Epitaxial Thin Films*, (unpublished).
[104] G. S. Girolami, *X-Ray Crystallography* (University science books, Mill Valley (Calif.), 2016).
[105] H. JINYUN, Structural Characterization of Perovskite Thin Films by X-Ray Reflectivity, THESIS, University of California, Davis, 2020.
[106] M. Yasaka, X-ray thin-film measurement techniques V. X-ray reflectivity measurement, **26**, 01 (2010).
[107] T. Konya, X-ray thin-film measurement techniques II. III. High resolution X-ray diffractometry, **25**, 01 (2009).
[108] G. Bauer, J. H. Li, and V. Holy, High Resolution X-ray Reciprocal Space Mapping, Acta Phys. Pol. A **89**, 115 (1996).

[109] B. D. Cullity and S. R. Stock, *Elements of X-Ray Diffraction*, 3. ed (Prentice Hall, Upper Saddle River, NJ, 2001).
[110] J. A. ón Santana, *Quantitative Core Level Photoelectron Spectroscopy* (Morgan & Claypool Publishers, San Rafael, 2016).
[111] D. W. Bruce, D. O'Hare, and R. I. Walton, editors , *Local Structural Characterisation: Inorganic Materials Series*, 1st ed. (Wiley, 2013).
[112] S. Thapa, R. Paudel, M. D. Blanchet, P. T. Gemperline, and R. B. Comes, Probing surfaces and interfaces in complex oxide films via in situ X-ray photoelectron spectroscopy, J. Mater. Res. **36**, 26 (2021).
[113] Angle Resolved XPS, (2008).
[114] P. C. J. and J. A., NIST Electron Effective-Attenuation-Length Database, (2011).
[115] K. Smith, D. Saenz, D. Zemlyanov, and A. Voevodin, XPS Thickness Solver, (2014).
[116] D. Y. Zemlyanov et al., Versatile technique for assessing thickness of 2D layered materials by XPS, Nanotechnology **29**, 115705 (2018).
[117] G. S. Henderson, F. M. F. De Groot, and B. J. A. Moulton, X-ray Absorption Near-Edge Structure (XANES) Spectroscopy, Rev. Mineral. Geochem. **78**, 75 (2014).
[118] C. Brouder, Angular dependence of X-ray absorption spectra, J. Phys. Condens. Matter **2**, 701 (1990).
[119] T. Yamamoto, Assignment of pre-edge peaks in K-edge x-ray absorption spectra of 3d transition metal compounds: electric dipole or quadrupole?, X-Ray Spectrom. **37**, 572 (2008).
[120] J. Wong, F. W. Lytle, R. P. Messmer, and D. H. Maylotte, K -edge absorption spectra of selected vanadium compounds, Phys. Rev. B **30**, 5596 (1984).
[121] B. T. Thole and G. Van Der Laan, Branching ratio in x-ray absorption spectroscopy, Phys. Rev. B **38**, 3158 (1988).
[122] *End Stations and Experiment*, https://synchrotron.uj.edu.pl/en_GB/linie-badawcze/astra/eksperyment.
[123] J. Stöhr, *X-Ray Natural Linear Dichroism*, (unpublished).
[124] J. Stöhr and H. C. Siegmann, *Magnetism: From Fundamentals to Nanoscale Dynamics* (Springer, Berlin, 2006).
[125] S. J. Pennycook, Scanning transmission electron microscopy: Seeing the atoms more clearly, MRS Bull. **37**, 943 (2012).
[126] X. Yan et al., Single-defect phonons imaged by electron microscopy, Nature **589**, 65 (2021).
[127] C. Ophus, Quantitative Scanning Transmission Electron Microscopy for Materials Science: Imaging, Diffraction, Spectroscopy, and Tomography, Annu. Rev. Mater. Res. **53**, 105 (2023).
[128] S. J. Pennycook, *Scanning Transmission Electron Microscopy: Imaging and Analysis* (Springer New York, New York, NY, 2011).
[129] T. T. Tran, Synthesis of Germanium-Tin Alloys by Ion Implantation and Pulsed Laser Melting: Towards a Group IV Direct Band Gap Semiconductor, (2017).
[130] Scanning Transmission Electron Microscopy, Nanoscience Instruments, n.d.
[131] E. Yasuda, editor , *Carbon Alloys: Novel Concepts to Develop Carbon Science and Technology* (Elsevier, Amsterdam : London, 2003).
[132] *Energy-Dispersive X-Ray Spectroscopy (EDS)*, in *Characterization of Nanoparticles* (Elsevier, 2020), pp. 397–417.

[133] A. Glavic and M. Björck, GenX 3: the latest generation of an established tool, J. Appl. Crystallogr. **55**, 1063 (2022).
[134] M. D. Blanchet, J. J. Heath, T. C. Kaspar, B. E. Matthews, S. R. Spurgeon, M. E. Bowden, S. M. Heald, T. Issacs-Smith, M. A. Kuroda, and R. B. Comes, Electronic and structural properties of single-crystal Jahn–Teller active Co1+xMn2−xO4 thin films, J. Phys. Condens. Matter **33**, 124002 (2021).
[135] H. Jeen, W. S. Choi, J. W. Freeland, H. Ohta, C. U. Jung, and H. N. Lee, Topotactic Phase Transformation of the Brownmillerite $SrCoO_{2.5}$ to the Perovskite $SrCoO_{3-\delta}$, Adv. Mater. **25**, 3651 (2013).
[136] N. Ichikawa, M. Iwanowska, M. Kawai, C. Calers, W. Paulus, and Y. Shimakawa, Reduction and oxidation of SrCoO2.5 thin films at low temperatures, Dalton Trans. **41**, 10507 (2012).
[137] D. Zhang, H. Ishizuka, N. Lu, Y. Wang, N. Nagaosa, P. Yu, and Q.-K. Xue, Anomalous Hall effect and spin fluctuations in ionic liquid gated SrCoO 3 thin films, Phys. Rev. B **97**, 184433 (2018).
[138] M. D. Blanchet, J. J. Heath, T. C. Kaspar, B. E. Matthews, S. R. Spurgeon, M. E. Bowden, S. M. Heald, T. Issacs-Smith, M. A. Kuroda, and R. B. Comes, Electronic and structural properties of single-crystal Jahn–Teller active Co1+xMn2−xO4 thin films, J. Phys. Condens. Matter **33**, 124002 (2021).
[139] L. Dahéron, R. Dedryvère, H. Martinez, M. Ménétrier, C. Denage, C. Delmas, and D. Gonbeau, Electron Transfer Mechanisms upon Lithium Deintercalation from LiCoO2 to CoO2 Investigated by XPS, Chem. Mater. **20**, 583 (2008).
[140] W. Samarakoon et al., Direct Imaging of the Structural and Morphological Evolution of Epitaxial LiCoO2 Films during Charge and Overcharge, J. Phys. Chem. C **126**, 15882 (2022).
[141] S. Cook, T. K. Andersen, H. Hong, R. A. Rosenberg, L. D. Marks, and D. D. Fong, Engineering the oxygen coordination in digital superlattices, APL Mater. **5**, 126101 (2017).
[142] V. Cuartero, S. Lafuerza, M. Rovezzi, J. García, J. Blasco, G. Subías, and E. Jiménez, X-ray absorption and emission spectroscopy study of Mn and Co valence and spin states in TbM n 1 − x C o x O 3, Phys. Rev. B **94**, 155117 (2016).
[143] F. M. F. De Groot, M. Grioni, J. C. Fuggle, J. Ghijsen, G. A. Sawatzky, and H. Petersen, Oxygen 1 *s* x-ray-absorption edges of transition-metal oxides, Phys. Rev. B **40**, 5715 (1989).
[144] J. Suntivich, W. T. Hong, Y.-L. Lee, J. M. Rondinelli, W. Yang, J. B. Goodenough, B. Dabrowski, J. W. Freeland, and Y. Shao-Horn, Estimating Hybridization of Transition Metal and Oxygen States in Perovskites from O K-edge X-ray Absorption Spectroscopy, J. Phys. Chem. C **118**, 1856 (2014).
[145] M. B. Panish and L. Reif, Vaporization of Iridium and Rhodium, J. Chem. Phys. **34**, 1915 (1961).
[146] *Kurt J. Lesker Company*, https://www.lesker.com/newweb/deposition_materials/deposition-materials-notes.cfm?pgid=ir1.
[147] J. E. Davey and T. Pankey, Epitaxial GaAs Films Deposited by Vacuum Evaporation, J. Appl. Phys. **39**, 1941 (1968).

[148] H. Freller and K. G. Günther, Three-temperature method as an origin of molecular beam epitaxy, Thin Solid Films **88**, 291 (1982).
[149] J. M. Longo, J. A. Kafalas, and R. J. Arnott, Structure and properties of the high and low pressure forms of SrIrO3, J. Solid State Chem. **3**, 174 (1971).
[150] A. Biswas and Y. H. Jeong, Growth and engineering of perovskite SrIrO 3 thin films, Curr. Appl. Phys. **17**, 605 (2017).
[151] S. Suresh, S. P. P. Sadhu, V. Mishra, W. Paulus, and M. S. Ramachandra Rao, Tunable charge transport properties in non-stoichiometric SrIrO3 thin films, J. Phys. Condens. Matter **36**, 425601 (2024).
[152] S. Esser et al., Strain-induced changes of the electronic properties of B -site ordered double-perovskite Sr 2 CoIrO 6 thin films, Phys. Rev. B **97**, 205121 (2018).
[153] A. Ohtomo, S. Chakraverty, H. Mashiko, T. Oshima, and M. Kawasaki, Spontaneous atomic ordering and magnetism in epitaxially stabilized double perovskites, J. Mater. Res. **28**, 689 (2013).
[154] M. Anderson, K. Greenwood, G. Taylor, and K. Poeppelmeier, B-cation arrangements in double perovskites, Prog. Solid State Chem. **22**, 197 (1993).
[155] T. Manako, M. Izumi, Y. Konishi, K.-I. Kobayashi, M. Kawasaki, and Y. Tokura, Epitaxial thin films of ordered double perovskite Sr2FeMoO6, Appl. Phys. Lett. **74**, 2215 (1999).
[156] M. Hashisaka, D. Kan, A. Masuno, M. Takano, Y. Shimakawa, T. Terashima, and K. Mibu, Epitaxial growth of ferromagnetic La2NiMnO6 with ordered double-perovskite structure, Appl. Phys. Lett. **89**, 032504 (2006).
[157] G. Kresse and J. Furthmüller, Efficiency of ab-initio total energy calculations for metals and semiconductors using a plane-wave basis set, Comput. Mater. Sci. **6**, 15 (1996).
[158] G. Kresse and J. Furthmüller, Efficient iterative schemes for *ab initio* total-energy calculations using a plane-wave basis set, Phys. Rev. B **54**, 11169 (1996).
[159] J. W. Furness, A. D. Kaplan, J. Ning, J. P. Perdew, and J. Sun, Accurate and Numerically Efficient r^2 SCAN Meta-Generalized Gradient Approximation, J. Phys. Chem. Lett. **11**, 8208 (2020).
[160] M. Kothakonda, A. D. Kaplan, E. B. Isaacs, C. J. Bartel, J. W. Furness, J. Ning, C. Wolverton, J. P. Perdew, and J. Sun, Testing the r^2 SCAN Density Functional for the Thermodynamic Stability of Solids with and without a van der Waals Correction, ACS Mater. Au **3**, 102 (2023).
[161] S. Swathilakshmi, R. Devi, and G. Sai Gautam, Performance of the r^2 SCAN Functional in Transition Metal Oxides, J. Chem. Theory Comput. **19**, 4202 (2023).
[162] P. E. Blöchl, Projector augmented-wave method, Phys. Rev. B **50**, 17953 (1994).
[163] G. Kresse and D. Joubert, From ultrasoft pseudopotentials to the projector augmented-wave method, Phys. Rev. B **59**, 1758 (1999).
[164] A. Jain et al., Commentary: The Materials Project: A materials genome approach to accelerating materials innovation, APL Mater. **1**, 011002 (2013).
[165] B. C. Chakoumakos, D. G. Schlom, M. Urbanik, and J. Luine, Thermal expansion of LaAlO3 and (La,Sr)(Al,Ta)O3, substrate materials for superconducting thin-film device applications, J. Appl. Phys. **83**, 1979 (1998).
[166] BMM Users Manual, (n.d.).
[167] B. Ravel and M. Newville, ATHENA, ARTEMIS, HEPHAESTUS: data analysis for X-ray absorption spectroscopy using IFEFFIT, J. Synchrotron Radiat. **12**, 537 (2005).
[168] M. Newville, Fundamentals of XAFS, Rev. Mineral. Geochem. **78**, 33 (2014).

[169] G. S. Henderson, F. M. F. de Groot, and B. J. A. Moulton, X-ray Absorption Near-Edge Structure (XANES) Spectroscopy, Rev. Mineral. Geochem. **78**, 75 (2014).
[170] M. A. Laguna-Marco, P. Kayser, J. A. Alonso, M. J. Martínez-Lope, M. Van Veenendaal, Y. Choi, and D. Haskel, Electronic structure, local magnetism, and spin-orbit effects of Ir(IV)-, Ir(V)-, and Ir(VI)-based compounds, Phys. Rev. B **91**, 214433 (2015).
[171] M. E. Sweers, Q. Ma, C. M. Donahue, D. Nordlund, S. M. Haile, and L. C. Seitz, Epitaxial strain-tuned oxygen vacancy formation, reduction behavior, and electronic structure of perovskite SrIr O 3, Phys. Rev. Mater. **8**, 055801 (2024).
[172] B. A. Duell, J. Li, D. Haskel, J. Kim, H. Park, P. G. LaBarre, A. P. Ramirez, and M. A. Subramanian, Iridium valence variation and carrier sign tuning in (Ca , Ba) x La 2 − x CuIrO 6 double perovskites, Phys. Rev. Mater. **5**, 054604 (2021).
[173] S. Agrestini et al., Probing the J eff = 0 ground state and the Van Vleck paramagnetism of the Ir 5 + ions in layered Sr 2 Co 0.5 Ir 0.5 O 4, Phys. Rev. B **97**, 214436 (2018).
[174] H. Chen and A. Millis, Charge transfer driven emergent phenomena in oxide heterostructures, J. Phys. Condens. Matter **29**, 243001 (2017).
[175] A. S. Disa, D. P. Kumah, A. Malashevich, H. Chen, D. A. Arena, E. D. Specht, S. Ismail-Beigi, F. J. Walker, and C. H. Ahn, Orbital Engineering in Symmetry-Breaking Polar Heterostructures, Phys. Rev. Lett. **114**, 026801 (2015).
[176] R. B. Comes, S. R. Spurgeon, S. M. Heald, D. M. Kepaptsoglou, L. Jones, P. V. Ong, M. E. Bowden, Q. M. Ramasse, P. V. Sushko, and S. A. Chambers, Interface-Induced Polarization in SrTiO3-LaCrO3 Superlattices, Adv. Mater. Interfaces **3**, 1500779 (2016).
[177] E. Benckiser et al., Orbital reflectometry of oxide heterostructures, Nat. Mater. **10**, 189 (2011).
[178] F. De Groot, G. Vankó, and P. Glatzel, The 1s x-ray absorption pre-edge structures in transition metal oxides, J. Phys. Condens. Matter **21**, 104207 (2009).
[179] J. Yano, J. Robblee, Y. Pushkar, M. A. Marcus, J. Bendix, J. M. Workman, T. J. Collins, E. I. Solomon, S. DeBeer George, and V. K. Yachandra, Polarized X-ray Absorption Spectroscopy of Single-Crystal Mn(V) Complexes Relevant to the Oxygen-Evolving Complex of Photosystem II, J. Am. Chem. Soc. **129**, 12989 (2007).
[180] T. C. Rossi et al., X-ray absorption linear dichroism at the Ti K edge of anatase TiO 2 single crystals, Phys. Rev. B **100**, 245207 (2019).
[181] B. Joseph, A. Iadecola, L. Simonelli, Y. Mizuguchi, Y. Takano, T. Mizokawa, and N. L. Saini, A study of the electronic structure of $FeSe_{1-x}$ Te_x chalcogenides by Fe and Se K-edge x-ray absorption near edge structure measurements, J. Phys. Condens. Matter **22**, 485702 (2010).
[182] J. M. Chen et al., Evolution of spin and valence states of (Pr 0.7 Sm 0.3) 0.7 Ca 0.3 CoO 3 at high temperature and high pressure, Phys. Rev. B **90**, 035107 (2014).
[183] G. Vankó, J.-P. Rueff, A. Mattila, Z. Németh, and A. Shukla, Temperature- and pressure-induced spin-state transitions in LaCoO 3, Phys. Rev. B **73**, 024424 (2006).
[184] O. Haas, R. P. W. J. Struis, and J. M. McBreen, Synchrotron X-ray absorption of LaCoO3 perovskite, J. Solid State Chem. **177**, 1000 (2004).
[185] M. G. Kim, Y. S. Im, E. J. Oh, K. H. Kim, and C. H. Yo, The substitution effect of Ca2+ ion on the physical properties in nonstoichiometric Dy1−xCaxCoO3−y system, Phys. B Condens. Matter **229**, 338 (1997).

[186] M.-C. Lee, S. Lee, C. J. Won, K. D. Lee, N. Hur, J.-L. Chen, D.-Y. Cho, and T. W. Noh, Hybridized orbital states in spin-orbit coupled 3 d − 5 d double perovskites studied by x-ray absorption spectroscopy, Phys. Rev. B **97**, 125123 (2018).
[187] G. Vankó, F. M. F. de Groot, S. Huotari, R. J. Cava, T. Lorenz, and M. Reuther, *Intersite 4p-3d Hybridization in Cobalt Oxides: A Resonant x-Ray Emission Spectroscopy Study*, arXiv:0802.2744.
[188] M. Sikora, Cz. Kapusta, K. Knížek, Z. Jirák, C. Autret, M. Borowiec, C. J. Oates, V. Procházka, D. Rybicki, and D. Zajac, X-ray absorption near-edge spectroscopy study of Mn and Co valence states in LaMn 1 − x Co x O 3 (x = 0 – 1), Phys. Rev. B **73**, 094426 (2006).
[189] X. Liu et al., Interfacial charge-transfer Mott state in iridate–nickelate superlattices, Proc. Natl. Acad. Sci. **116**, 19863 (2019).
[190] L. J. van der PAUW, A method of measuring specific resistivity and hall effect of discs of arbitrary shape, Philips Res. Rep. **13**, 1 (1958).
[191] F. S. Oliveira, R. B. Cipriano, F. T. Da Silva, E. C. Romão, and C. A. M. Dos Santos, Simple analytical method for determining electrical resistivity and sheet resistance using the van der Pauw procedure, Sci. Rep. **10**, (2020).
[192] A. A. Ramadan, R. D. Gould, and A. Ashour, On the Van der Pauw method of resistivity measurements, Thin Solid Films **239**, 272 (1994).
[193] van der Pauw - Hall Option, (2021).
[194] F. Werner, Hall measurements on low-mobility thin films, J. Appl. Phys. **122**, (2017).
[195] S.-K. Wong, B. H. Chia, K. Srinivasan, R. Law, E.-L. Tan, H. K. Tan, R. Sbiaa, and S. N. Piramanayagam, Anomalous Hall effect measurement of novel magnetic multilayers, J. Appl. Phys. **106**, (2009).
[196] N. Nagaosa, J. Sinova, S. Onoda, A. H. MacDonald, and N. P. Ong, Anomalous Hall effect, Rev. Mod. Phys. **82**, 1539 (2010).
[197] D. I. Khomskii, *Transition Metal Compounds*, 1st ed. (Cambridge University Press, 2014).
[198] M. Hoffmann, V. S. Borisov, S. Ostanin, I. Mertig, W. Hergert, and A. Ernst, Magnetic properties of defect-free and oxygen-deficient cubicSrCoO3−δ, Phys. Rev. B **92**, (2015).
[199] J. Lim and J. Yu, Role of oxygen vacancy in the spin-state change and magnetic ordering in SrCoO 3 − δ, Phys. Rev. B **98**, 085106 (2018).
[200] H. Taguchi, M. Shimada, and M. Koizumi, The electrical properties of ferromagnetic SrCoO3−δ (0 <δ <0.5), Mater. Res. Bull. **15**, 165 (1980).
[201] R. H. Potze, G. A. Sawatzky, and M. Abbate, Possibility for an intermediate-spin ground state in the charge-transfer materialSrCoO3, Phys. Rev. B **51**, 11501 (1995).
[202] M. Zhuang, W. Zhang, A. Hu, and N. Ming, Possible magnetic ground state in the perovskiteSrCoO3, Phys. Rev. B **57**, 13655 (1998).
[203] J. Kuneš, V. Křápek, N. Parragh, G. Sangiovanni, A. Toschi, and A. V. Kozhevnikov, Spin State of Negative Charge-Transfer MaterialSrCoO3, Phys. Rev. Lett. **109**, (2012).
[204] G. Van Der Laan and B. T. Thole, Local Probe for Spin-Orbit Interaction, Phys. Rev. Lett. **60**, 1977 (1988).
[205] Vapor Pressure of Tantalum (Ta), Dr. Eberl MBE-Komponenten GmbH, n.d.
[206] L. Liu et al., Uniform nucleation and epitaxy of bilayer molybdenum disulfide on sapphire, Nature **605**, 69 (2022).
[207] W. Li et al., Approaching the quantum limit in two-dimensional semiconductor contacts, Nature **613**, 274 (2023).

[208] H.R.4346 - CHIPS and Science Act, 2022.
[209] *CHIPS and Science Act*, in *Wikipedia* (https://en.wikipedia.org/wiki/CHIPS_and_Science_Act).
[210] S. Holland, Trump announces private-sector $500 billion investment in AI infrastructure, (2025).